Analysis of selected observations of magnetic turbulence in the solar wind

SR MCKEE

orcid.org 0000-0002-2725-265X

Dissertation accepted in partial fulfilment of the requirements for the degree *Master of Science in Astrophysical Sciences* at the North-West University

Supervisor: Prof RA Burger

Graduation May 2020

28831586

Abstract

Models for the modulation of galactic cosmic rays, such as those used to study space weather (see discussion by Moloto et al., 2018), require as input a diffusion tensor, which in turn depends on the magnetic turbulence spectrum (see, e.g., Bieber et al., 1994; Engelbrecht and Burger, 2013a,b). It is convention to assume that the inertial range of the magnetic turbulence spectrum is a power law with the Kolmogorov spectral index. The current project introduces a numerical technique, which will analyse the power spectra derived from Voyager 1 magnetic field data, in order to characterise the form of the turbulence power spectrum. The most common form taken on by the power spectrum is that with a Kolmogorov spectral index associated with the inertial range of the turbulence spectrum. Driving by pickup ions (see, e.g., Zank, 1999; Isenberg, 2005; Cannon et al., 2014; Aggarwal et al., 2016; Cannon et al., 2017), at scales around the proton gyro frequency are suggested to influence the form of the turbulence power spectrum. If this driving is significant, it should show up in Voyager 1 spacecraft measurements beyond about 20 AU. The current project shows however no significant changes to the underlying power spectrum in the presence of pickup ion peaks. The presence of pickup ions is indicated by small enhancements above the background spectrum at the gyrofrequency of the pickup ion species. The current project finds evidence for helium and proton pickup ion species. The results of the current project show that peaks associated with helium pickup ions are more frequent at smaller radial distances and those associated with proton pickup ions are more frequent at larger radial distances. The current project also includes a theoretical discussion of the total turbulence power spectrum and compares the result to that presented in Bieber (1996). The current results are more general and agrees with that presented in Bieber (1996) for inertial range spectral index $q = 2$.

Keywords: Turbulence spectrum, turbulence structure, turbulent magnetic field, Voyager 1, pickup ions

Contents

Chapter 1

Introduction

The thought of analysing and being able to make any deductions from Voyager magnetic field data is at first challenging. These data sets are notorious for possessing large gaps in the data. However, the analysis of these data sets is important when gaining insight into the behaviour of the solar wind as it moves out through the heliosphere from smaller to larger radial distances.

Power spectra derived from the solar wind magnetic field data, observed by the Voyager 1 spacecraft, form the main analysis tool in this discussion. The slope of the power spectrum should indicate the presence of turbulence in the solar wind magnetic field data. The power spectral density, as a function of frequency, is expected in theory to resemble the power spectra as described in Kolomogorov theory (Kolmogorov, 1941a). This text presents a numerical technique that ascertains the value of the spectral indices which define the Voyager data power spectra. This technique also estimates the bend-over scale which is a parameter input for cosmic ray modulation models, it is referred to as the "break-point frequency" in this text.

Bieber et al. (1993) suggest that applying the techniques of "Pre-Whitening" and "Post-Darkening" to the data yield an improved power spectrum. These techniques are suggested to be advantageous especially when working with data sets that contain missing data records. The power spectrum described in Bieber et al. (1993) for use in pre-whitening and post-darkening methods is derived in the text. Voyager 1 data is then analysed using this derived expression for different percentages of missing data. It is then posited whether or not there is sufficient gain in applying the methods suggested in Bieber et al. (1993) to the data.

As for the filtering of the data sets and the processing of data with missing records, an appropriate filtering technique is developed and applied. The aim was to remove spurious data peaks and fill in the missing records. The numerical technique is then applied to a synthetically generated data set with pickup ion signatures in the input power spectrum. The numerical technique is then tested to see if it can identify these signatures apart from the background spectrum.

Another topic of investigation in the current project is the radial dependence of the magnetic field variance data, which is of particular interest to cosmic-ray modulation studies. The current study compares the radial dependence for radial distances below 40 au with previous results.

A theoretical analysis of the structure of turbulence is presented in accordance with the

procedure of Bieber (1996). An expression for the total energy (total power spectrum) of the turbulent fluctuations in the solar wind is derived and compared to the result posited in Bieber (1996). On comparison, the expression in this discussion is a generalisation of the specific case in Bieber (1996) where both approaches agree at a value of $q = 2$ for the inertial range spectral index. Turbulence power spectra are mathematically built using composite models of slab and 2D components. The process whereby this is achieved is the topic of the theoretical chapter in this project.

Chapter 2 gives a brief background to the study. The numerical procedure to be used for the analysis of the Voyager 1 magnetic field data is introduced and benchmarked in Chapter 3. Chapter 4 describes the analysis of the magnetic field data and the quest for pickup ion signatures in the power spectra. Theoretical results pertaining to the 2D/slab structure of turbulence are presented in Chapter 5. A summary and conclusions are given in Chapter 6.

Chapter 2

Background

2.1 Introduction

The focus of this dissertation is on the results that are of use for models of cosmic-ray modulation. Cosmic-ray intensity varies on a time scale of years (see, e.g., Parker, 1965; Kota and Jokipii, 1983; Moloto, 2015) and consequently turbulence studies relevant to cosmic-ray scattering should address changes that occur on the time scale of weeks or months at the most. Improved understanding of the nature of turbulence in the heliosphere has led to an improved understanding of cosmic-ray transport (see, e.g., Bieber et al., 1994; Engelbrecht et al., 2017; Engelbrecht and Burger, 2013a; Engelbrecht, 2017). This introductory chapter serves to introduce some of the concepts used in this dissertation. Turbulence covers a vast range of topics and those selected are only meant to give some idea of the width of this field.

2.2 A magnetohydrodynamic description of turbulence

Discussions surrounding turbulence theory are centered on the structure and the properties of the magnetic field. This is because as with MHD (Magnetohydrodynamic) turbulence, turbulence in the electric field is assumed to be negligible ($\delta E \approx 0$) (Dosch and Zank, 2015). MHD turbulence is observed in a fluid which is incompressible (Goldreich and Sridhar, 1997). MHD turbulence involves fluctuations which are random in nature and are of magnetic origin. The term "fluctuations", in this context, refers to Alfvén waves as well as compressible magnetosonic type fluctuations. This combination of waves comprises the MHD turbulence observed in trailing edges of the high-speed streams. However, the magnetosonic waves are significantly weaker when compared to the Alfvén waves (Dobrowolny et al., 1980). The energy transferred by such turbulent wave fluctuations through a fluid flow can be described by adopting a Kolmogorov theory description. Additional to the fluctuating wave type description of turbulent energy transfer, the MHD equations can be used to formulate a mathematical description of the energy transfer in terms of the properties of a turbulent flow (Zank, 2014). In the case of turbulent flow, the Reynolds number is an important parameter specifically in the study of fully developed turbulence. The Reynolds number R is defined as

$$R = \frac{LV}{\nu}; \tag{2.1}$$

where L is the length scale, V is the solar speed, and velocity, and ν is the viscosity of the fluid. R is a control parameter for the incompressible flow which charaterises the turbulence (Frisch and Kolmogorov, 1995). Fully developed turbulence occurs when the Reynolds number is very large. However, this occurs on the condition that the flow is not being constrained in any sense (Frisch and Kolmogorov, 1995).

Another important feature of Kolmogorov theory is the inertial range spectral index (Goldreich and Sridhar, 1997). The inertial range extends down to turbulence dissipation scale (Frisch and Kolmogorov, 1995) and includes scales which grow as $\sim R^{3/4}$, where R is the Reynolds number. Scales lower than this constitute the dissipation range (Frisch and Kolmogorov, 1995).

2.3 Turbulence and the solar wind

The solar wind is a collisionless plasma (Zank, 2014) which has a radially directed flow travelling at a supersonic velocity, becoming subsonic at the heliospheric termination shock. The heliospheric magnetic field originates where the field lines are anchored to the sun. The field lines move with the solar wind plasma as it propagates away from the sun; the magnetic field is thus considered to be *frozen in* due to the high conductivity of the solar wind plasma. The field lines are then twisted into a spiral configuration as a result and dragged along with the plasma as it flows away from the sun. This configuration is known as an Archimedean spiral first posed by Parker (1965). The field lines begin flowing radially outwards with the solar wind at radial distances close to the solar surface. As the solar wind moves to larger radial distances further from the solar surface, the radial component of the field is no longer dominant and the azimuthal component becomes significant. The decrease in the radial component of the magnetic field with distance is expected by the conservation of magnetic flux for the constant flow solar wind. It is important to note that it is the azimuthal component of the magnetic field which drives the spiral geometry (Owens and Forsyth, 2013).

2.4 Turbulent energy cascade

Figure 2.1 shows how the energy transfers from eddies at one scale to those at the next scale; which is smaller but comparable to the first. The energy transfer in the cascade has thus a local nature to it (Frisch and Kolmogorov, 1995). Energy cascades through the eddy scales at a uniform rate since the rate of energy absorbed is the same as the rate at which it is dissipated. This then means that if energy is injected into eddies on large scales at a rate ε, the energy is dissipated by eddies at the samllest scales at the same rate ε (Frisch and Kolmogorov, 1995).

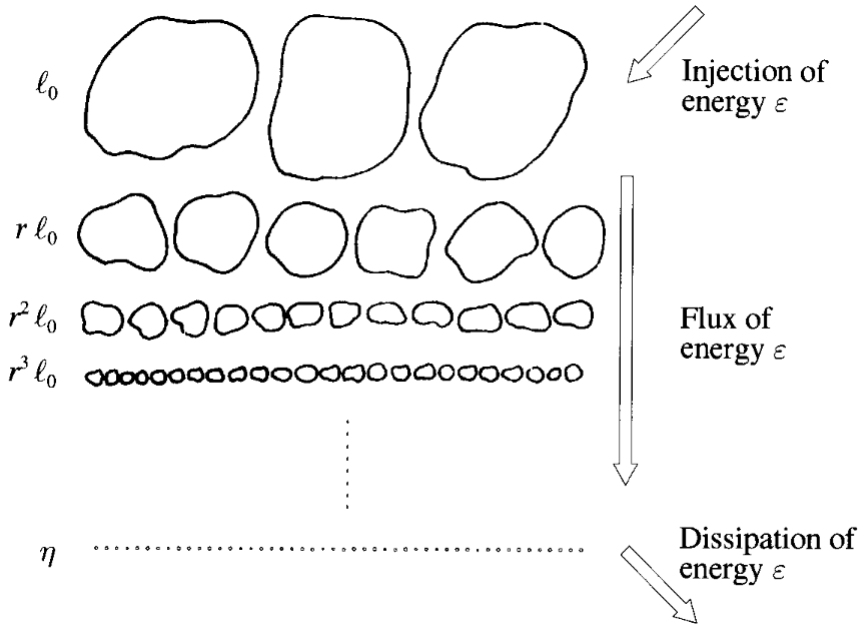

Figure 2.1: Schematic representation of the energy cascade through the various eddy scales. The movement of the energy throughout the eddies scales is indicated on the far right of the figure (Frisch and Kolmogorov, 1995).

Notice in Figure 2.1 that the small eddies fill up just as much space as the large eddies do. The point is that at large scales there are fewer eddies required to fill the same length (space) which is filled at smaller scales by making use of many more eddies. This feature of the energy cascade that all eddies are space-filling ensures that the inertial range is scale-invariant. Eddies are assumed to be space filling in Kolmogorov theory; that is there are no boundaries restricting the distribution of the eddies in space (Frisch and Kolmogorov, 1995).

Kolmogorov turbulence

Incompressible turbulence is consistent with Kolmogorov theory (Kolmogorov, 1941b) if the flow in question has a Mach number which is small in value. This requirement is summarized by the condition of $M \ll 1$, where M is the Mach number (Frisch and Kolmogorov, 1995). This defining theory assumes isotropic turbulence and an energy cascade brought on by the interaction of structures known as "eddies" over many scale sizes. The spectral index of the inertial range is shown to have a value of $-5/3$.

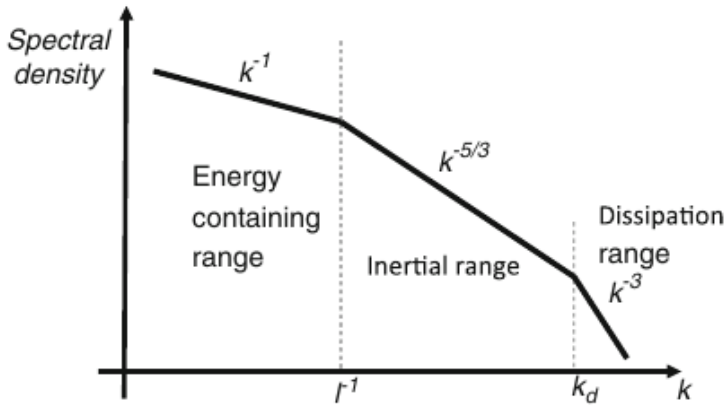

Figure 2.2: Schematic representation of the Kolmogorov turbulence phenomonology (Zank, 2014).

2.5 The structure of turbulence

The presence of turbulence in the solar wind is certainly not a new observation, and there is a huge body of knowledge in the literature. However, there is a great deal still to be learnt about turbulence in the solar wind. From an observational perspective, turbulence in the solar wind has been observed through fluctuations in the magnetic field, magnetic field velocity as well as the flow velocity of the solar wind. The solar wind was classified as being a "turbulent magnetofluid" after displaying a random and non-reproducable nature. The observations of the parameters of the solar wind (such as density and speed) as a function of time were thus also of a random nature. Most importantly, the magnetic field variances about the mean field are observed to be large and this is thought to imply the presence of turbulent "eddies" on various scales. The study of turbulence in the solar wind contributes to the knowledge of the nature of the solar wind plasma. Turbulence is after all a cascade of energy over various scales and when dissipating energy, imposes heating effects within the plasma (Marsch, 1991).

2.5.1 Slab model

The wavevectors of turbulent fluctuations in the magnetic field are directed only along one direction in the slab model. The model thus only depends on the mean field aligned coordinate as shown in Figure 2.3. Slab turbulence is referred to as Alfvénic fluctuations in some literature (Zank, 2014). Note that the structure of slab turbulence is such that the fluctuations will be well-correlated in the direction perpendicular to the mean magnetic field with large correlation scales.

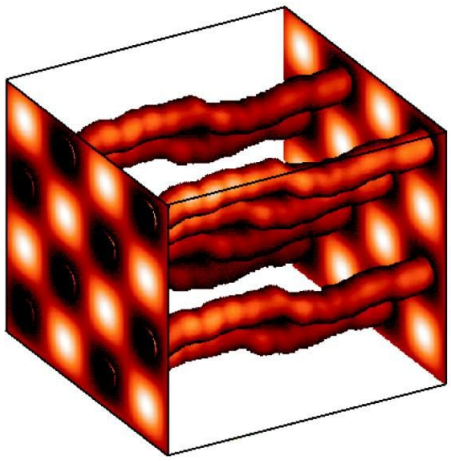

Figure 2.3: Visualisation of the slab turbulence model. Note that the magnetic field direction is in the direction of the flux tubes, and that all the flux tubes are "in step" in the direction perpendicular to the field. (Matthaeus et al., 2003)

2.5.2 2D model

For this model, the wavevectors of the fluctuations are restricted to a plane perpendicular to the mean magnetic field. The model depends on two spatial variables in the plane perpendicular to the mean field. In contrast to slab turbulence, these fluctuations will be well-correlated in the direction of the mean magnetic field. The visualisation of this model is in Figure 2.4.

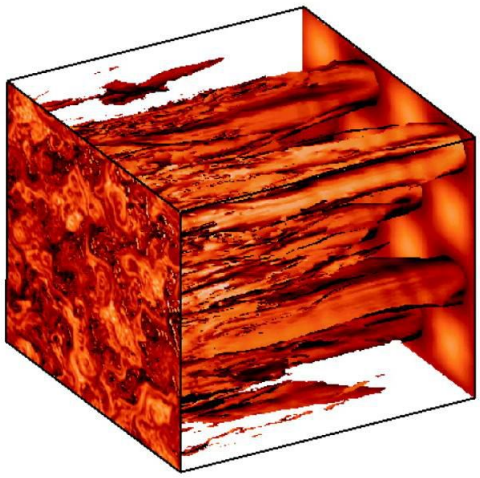

Figure 2.4: Visualisation of the composite slab/two-dimensional turbulence model (Matthaeus et al., 2003).

2.5.3 Composite model

In this model, the slab and 2D models are used together to form a description of turbulence. Observational evidence for such a model was first presented by Matthaeus et al. (1990). These authors found that the correlation lengths obtained from ISEE-3 data at 1 au were clustered in the form of a Maltese cross, with longer length scales in the direction of the field and perpendicular to it than in directions in between. The model relies on the specification of both a slab turbulence spectrum as well as a 2D turbulence spectrum (Hussein et al., 2015). Bieber (1996) and Saur and Bieber (1999) calculated the actual ratio of slab and 2D turbulence from data and found that the 2D component dominates. The calculations of Bieber and co-workers will be revisited in Chapter 5 where it will be shown that results from this highly-cited paper are in fact only valid for a specific value of the spectral index of the inertial range.

2.5.4 Goldreich-Sridhar turbulence

A specific relationship between the parallel and perpendicular wavenumbers underpins the theory of this model (Goldreich and Sridhar, 1995). The relation $|k_{\parallel}| \sim k_{\perp}^{2/3}$ was derived after accounting for Kolmogorov cascading and the critical balance condition (Hussein et al., 2015). The term *critical balance* refers to the balance between the linear propagation scales and the time scales of nonlinear interactions on a scale-to-scale basis. This implies that the time scales for linear and non-linear propagation are the same. Critical balance is an assumption on scaling associated with strong turbulence. The notion of critical balance is important to this model because it is what makes a prediction on the energy content of the model. The energy for this model is at a maximum when the model is in a state of critical balance. This model treats wavenumbers in a specialised way as wavelets (Hussein et al., 2015). Additionally, this model is anisotrophic and three dimensional. Further information on the implementation of this model can be found in the work by Kowal and Lazarian (2010) and Lazarian and Vishniac (1999).

2.5.5 Iroshnikov-Kraichnan turbulence

In this section, the discussion surrounds a turbulence theory which builds on from the already known Kolmogorov theory of turbulence. The extension comes in when adding the presence of a magnetic field (Falgarone and Passot, 2008). As in previously discussed theories, the idea of fluctuations being visualised as wave packets is used here again. In this particular theory, the wave packets are Alfvén wave packets propagating along the magnetic field lines (Falgarone and Passot, 2008). Just like in Kolomogorov theory, Iroshnikov-Kraichnan theory should have an energy transfer mechanism. The energy transfer mechanism, in this case, is the collision of the wave packets which are moving in opposing directions (Goldreich and Sridhar, 1997). The inclusion of the presence of a magnetic field in the model means that the spectral index $(-3/2)$ differs from the index $(-5/3)$ in Kolmogorov turbulence theory. These are but a few defining features of this particular theory (Ng and Bhattacharjee, 2007). Further subject matter is available in the work by Ng and Bhattacharjee (2007) and Kraichnan (1965).

2.6 Background on pickup ions

The existence of pickup ions (Axford et al., 1963) was first confirmed when pickup helium was observed *in situ* (Möbius et al., 1985). Neutral particles are ionised by one of three main mechanisms (Wu et al., 2016):

- Charge exchange with ions.
- Sunlight induced photoionization.
- Ionization through impact with electrons in the solar wind.

The term pickup ion stems from the behaviour of the ion when interacting with the solar wind. As the solar wind passes by the ion, the ion encounters the heliospheric magnetic field and begins to gyrate around the magnetic field. The ion is then essentially "picked up" and carried along with the solar wind, and thus carries the name "pickup ion" (Wu et al., 2016). Since the solar wind is a turbulent plasma which interacts with the pickup ions, the study of turbulence is important in understanding pickup ion transport and propagation inside the heliosphere. In fact, turbulence in the solar wind is thus far suggested to be a source of pickup ion scattering in the heliosphere (Wu et al., 2016). The neutral atoms which become pickup ions come from four localised populations (Wu et al., 2016):

- Neutral atoms from interstellar space.
- Neutral atoms from a source in the inner heliosphere.
- Neutral atoms from a source in the outer heliosphere.
- The populations of neutrals in the supersonic solar wind.

Each pick-up ion species has a characteristic gyrofrequency given by

$$\omega_i = \frac{q_i B}{m_i}. \tag{2.2}$$

Note that this is an angular frequency and has to be divided by 2π to get frequency in Hz. The comprehensive studies of Hollick et al. (2018a,b,c) done to identify pickup ion signatures in Voyager 1 data will be discussed and some of their results compared with results from this project, in Chapter 4.

2.7 Theoretical pickup ion spectra

Williams and Zank (1994) calculate the so-called asymptotic wave spectra expected to be induced by pickup ions up to about 50 au from the Sun. The authors caution that their calculations assume homogeneous conditions associated with quiet-time conditions in the heliosphere, and are done for a small volume element and not an extended space like the heliosphere. Although a direct comparison with such theoretical predictions as those of Williams and Zank (1994) is beyond the scope of this dissertation, they do provide a useful test for the numerical technique that is used to calculate spectra along the trajectory of the Voyager 1 spacecraft.

Only two examples provided by Williams and Zank (1994) will be considered. These are valid in the spacecraft frame; first for an azimuthal field and then for a radial field. In both cases, the solar wind speed is assumed to be larger than the Alfvén speed. These two examples will be used to test the numerical technique discussed in Chapter 3.

Azimuthal field

At sufficiently large radial distances in the ecliptic plane, the magnetic field becomes almost purely azimuthal. The power spectrum is then given by Equation (36) of Williams and Zank (1994),

$$\begin{aligned} P(\omega) &= \frac{nmv_A^2\Omega_i}{\omega^2}\Big(1+\frac{v_A}{V_w}\Big)\Big(1-\frac{\Omega_i}{\omega}\frac{v_A}{V_w}\Big); \\ \Omega_i\frac{v_A}{V_w} &\leq \omega \leq \Omega_i; \end{aligned} \tag{2.3}$$

where ω is the wave frequency, Ω_i is the pickup ion frequency, v_A is the Alfvén speed, n is the pickup ion number density, and m is the mass of a pickup ion. Note that the spectrum is zero at the lower limit of the allowed frequencies, and cuts off when the frequency reaches the ion gyrofrequency. The maximum of the spectrum is at one or two tenths of the gyrofrequency.

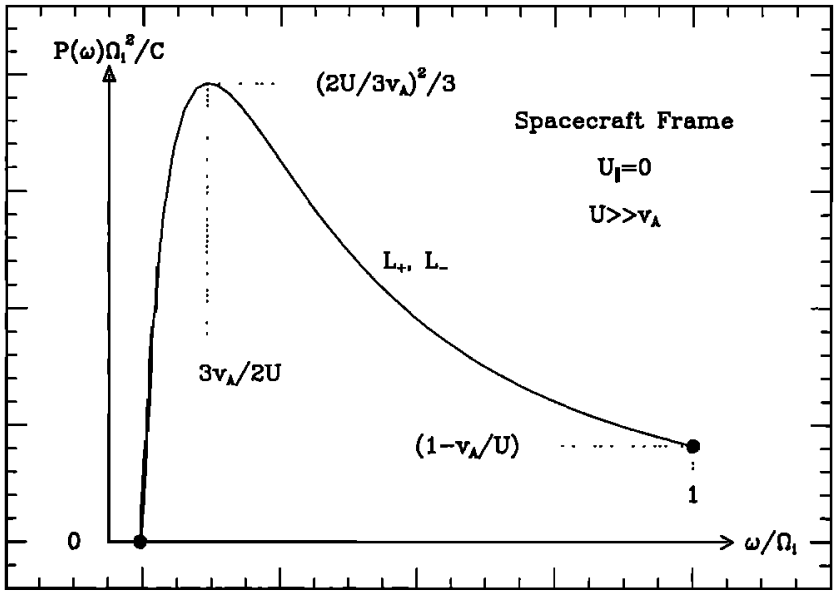

Figure 2.5: Wave excitation spectrum expected in theory for azimuthal field geometry. L_+, L_- indicate the polarisation states of the waves as discussed in Williams and Zank (1994). Note that these authors use U for the solar wind speed V_w.

Radial field

The fact that the heliospheric magnetic field is an Archimedean spiral in the ecliptic plane, means that radial field will only be seen very close to the Sun. In this case, the power spectrum is given by

$$\begin{aligned} &P(\omega) = nmv_A(V_w - v_A)\frac{\Omega_i}{\omega^2}; \\ &\Omega_i \leq \omega \leq \infty \end{aligned} \tag{2.4}$$

where the symbols used are the same as for the case of an azimuthal field. In this case, the maximum of the spectrum is at the frequency $nmv_A(V_w - v_A)$, and the spectrum has no cutoff but drops as ω^{-2} (or equivalently f^{-2} beyond the gyrofrequency).

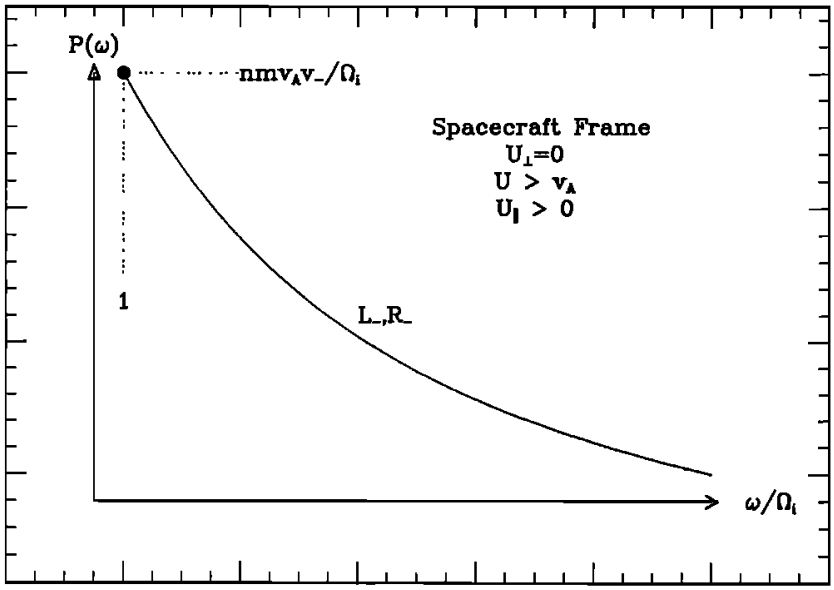

Figure 2.6: Wave excitation spectrum expected in theory for radial field geometry. L_+, R_- indicate the polarisation states of the waves as discussed in Williams and Zank (1994). Note that these authors use U for the solar wind speed V_w.

2.8 An appropriate choice of coordinates

Before doing a data study of a certain problem, it is always important to consider a coordinate system which is appropriate to the physical system in question. The problem at hand is to describe the properties of the turbulence phenomena observed in the solar wind. The solar wind is a radial outflow from the solar surface. It would be far more appropriate to describe the turbulence in the solar wind using a coordinate system with a radial description. The RTN coordinate system has a radial dimension and is often used to describe spacecraft position in space. The RTN coordinate system stands for the radial-tangential-normal coordinate system (Davis, 2010) and how this coordinate system relates

to the (x,y,z) Cartesian coordinate system is that when mapped in to the Sun-observer plane, the Cartesian coordinate system is returned (Howard, 2011). The directions in the RTN coordinate system are defined as follows:

- R: This is the radial coordinate in the radial direction with unit vector $\widehat{\boldsymbol{R}}$ (Losa et al., 2005).
- T: This is the tangential coordinate which is perpendicular to the radial direction but in the orbital plane of a spacecraft. This direction has the unit vector $\widehat{\boldsymbol{T}}$ which points towards the spacecraft (Losa et al., 2005).
- N: This is the normal coordinate. The unit vector $\widehat{\boldsymbol{N}}$ is in the direction of the angular momentum of a spacecraft and is normal to both R and T (Losa et al., 2005).

In terms of the measurements of the turbulent magnetic field within the solar wind, measurements along the z-direction of the Cartesian coordinate system are most important. Since spacecraft measurements are made in the RTN system, the N-component is most important to turbulence studies because the N-component maps back to the z-component in the Cartesian system (Russell et al., 2016). Consider Figure 2.7 below which schematically illustrates how the RTN coordinate system relates to the Cartesian and other coordinate systems.

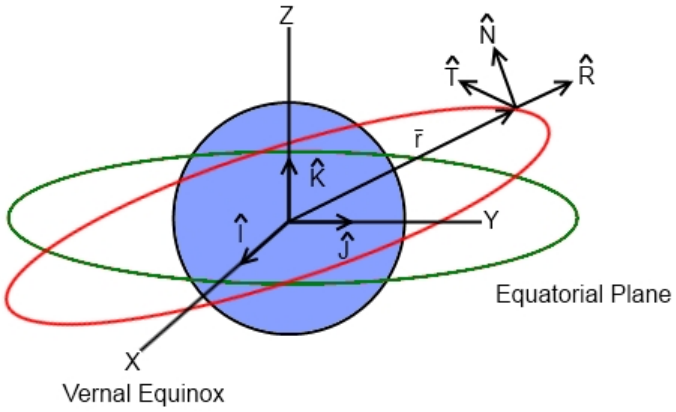

Figure 2.7: Coordinate systems used to describe how a spacecraft orbits around the earth in space. The position of the spacecraft is at the origin of the RTN coordinate system. The Cartesian system (x,y,z) is indicated along with the Geocentric Equatorial coordinate system (Maclean et al., 2014).

Since it is a spacecraft which make use of the coordinate system elaborated on above, the spacecraft itself is briefly discussed in the next section. The Voyager 1 spacecraft carrying a plasma instrument that is used to measure solar wind parameters is the final topic of discussion for this chapter.

2.9 The Voyager mission

The Voyager interstellar mission (first called the Mariner Jupiter/Saturn 1977) was launched in the year 1977. Voyager 2 was launched first in August; followed by Voyager 1 in September (Jet Propulsion Laboratory, ndc). Both Voyager spacecrafts have made signficant contributions to the current knowledge of our Solar system and interstellar space. Data from Voyager 1 is analysed later in this paper. A brief review of the spacecraft mission from Voyager 1 is given along with the current mission status.

Voyager 1 mission timeline (Jet Propulsion Laboratory, ndc) ;

- 1977: Launch, Spacecraft photos of Earth and the Moon
- 1979: Jupiter Encounter
- 1980: Saturn Encounter
- 1990: Takes the last images of the mission
- 1998: Passes the recorded distance of Pioneer 10
- 2004: Termination shock crossing
- 2012: Enters interstellar space after crossing the heliopause.
- 2013: Makes first measurement of interstellar medium density.

The Voyager 1 is currently (November 2019) 145 au from the Sun. The Voyager missions are expected to deliver data until the year 2020 (Jet Propulsion Laboratory, ndb). The Plasma Science instrument on board the instrument Voyager 1 was turned off in 1980 and so measurements of solar wind plasma parameters have not been available from this source since then. Only 4 of the 10 instruments onboard Voyager 1 are still operational (Jet Propulsion Laboratory, ndb). The Voyager 1 spacecraft has already surpassed expectations after performing the designated planetary flyby's of Jupiter and Saturn and then going on to reach interstellar space (Jet Propulsion Laboratory, ndc). Voyager data has been an instrumental source of information in many fields of study including the solar wind, the heliospheric magnetic field, cosmic rays and the composition of properties of interstellar space. Outer heliosphere studies (Jet Propulsion Laboratory, nda) and those concerning the structure of the heliosphere have also benefitted from the Voyager data sources.

2.10 Summary

This background chapter serves as a brief review of selected concepts in the theory of turbulence. Models such as the composite model, used to define the structure of turbulence, were discussed briefly. A review of the turbulent energy cascade describes how energy is transferred between the different eddy scales. On larger scales, the highly turbulent solar wind is discussed as a turbulent fluid. Also associated with the solar wind are the pickup ion particle populations. A brief background on the pickup ion and how they interact with the solar wind is presented. Two theoretical pickup ion spectra are discussed and will be used in Chapter 3 to test the numerical technique. Also discussed in the current chapter is

the Voyager mission and its current status. The choice of coordinates appropriate to the current study is elaborated on, including why it is appropriate for the current study and the data sets being used.

Chapter 3

Numerical technique and benchmarking

3.1 Introduction

Turbulence power spectra are used to study the cascade of energy from one scale to another. A turbulence power spectrum is generated by plotting the power spectral density (PSD) as a function of frequency (f). Various techniques are available to calculate this, but the most commonly used one is the Fourier transform. The calculations reported in this dissertation are performed in the Python language by source code supplied by the developers of the Python SciPy library (Jones et al., 2001). The code uses a periodogram to generate the power spectral density estimates. This is ideal for analysing spacecraft data with gaps and variable fluctuations in the signal. When analyzing Voyager 1 turbulence spectra data in Chapter 4, qualitative rather than quantitative results are used. The quantitative results in the current chapter are used to test the accuracy of the numerical technique from the SciPi library.

3.2 Fitting procedure for turbulence spectra

The frequency spectrum in the current project is divided in to two variable ranges, namely the energy and the inertial range. Each range is fitted by a power law and its spectral index is then found by optimizing the fit. However, at frequencies lower than the energy containing range, the index is assumed to be zero so that the energy density output is finite. The high frequencies are described in some texts by a dissipation range, but this range is neglected for the current study since the data resolution chosen for the current project will not be able to resolve it. The break point between the energy range and the inertial range is denoted by bp_2 and the break point between the energy range and low frequencies is denoted by bp_1.

The numerical modelling procedure uses the three-stage spectrum

$$PSD_{model}(f) = C \begin{cases} f^{-e}, & \text{if } f \geq f_{bp_2} \\ f_{bp_2}^{-e}(f/f_{bp_2})^{-d}, & \text{if } f_{bp_1} < f < f_{bp_2} \\ f_{bp_2}^{-e}(f_{bp_1}/f_{bp_2})^{-d}, & \text{if } f \leq f_{bp_1} \end{cases}; \tag{3.1}$$

where C is a constant determining the spectral level, f_{bp_2} is the frequency separating the energy range and the inertial range, e is the index of the spectrum in the inertial range, f_{bp_1} is frequency separating the low-frequency range and the energy range and d is the index of the spectrum in the energy range.

The fitting procedure is broken up into multiple components which are listed and briefly addressed below:

- A first estimate for the value of C is made, using the high-frequency part of the spectrum.
- This estimate of the value of C is then used with estimates for other parameters and then a two range fit is performed for the inertial and energy range.
- A full three range fit is then performed. All parameters are optimized using the outputs of the two stage process as input to this stage.

Given the large number of Fourier nodes that are generated when using around 1 minute resolution data spanning 13 days, a subset of (nearly) logarithmically spaced data points are used for graphs rather than the full set. Fits to the full set and the subset are virtually identical. An example using an arbitrary magnetic field dataset from the ACE spacecraft is shown in Figures 3.1 and 3.2.

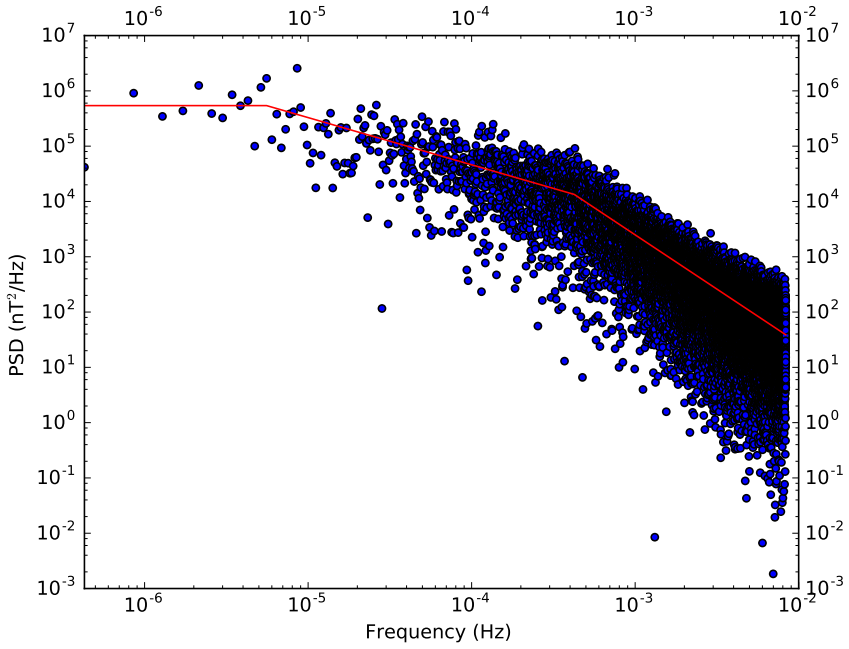

Figure 3.1: Example of a power spectrum as a function of frequency for a 13-day interval of the ACE spacecraft data set for the N component of the magnetic field.

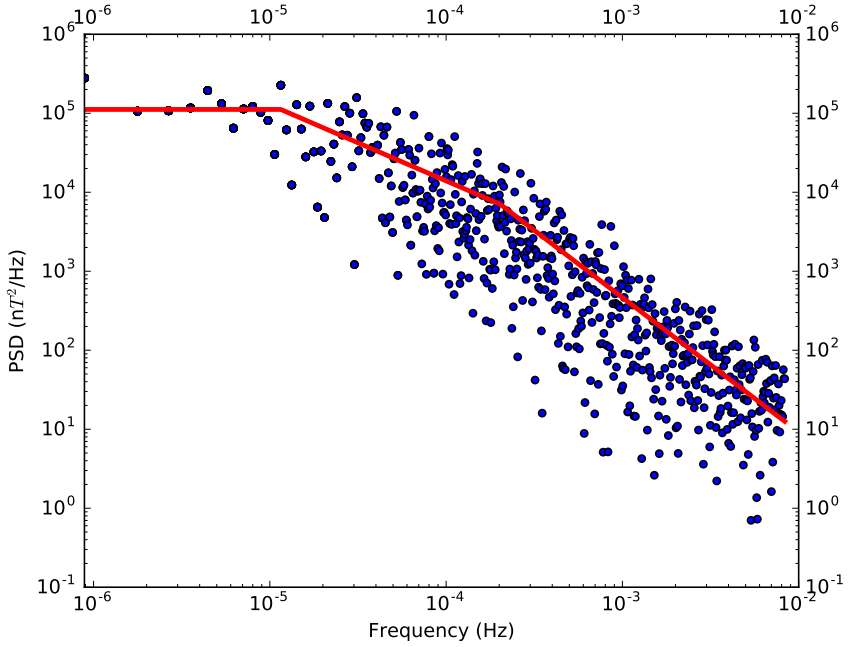

Figure 3.2: Power spectrum as a function of logarithmically spaced frequencies for the interval of ACE spacecraft data. The frequency range is made up of 1000 logarthmically spaced points.

3.3 Benchmarking numerical technique

The numerical technique was applied to a synthetically generated data set (see Appendix A) and the results of the analysis compared to the input values. The equivalent of fourteen 27-day intervals with one minute resolution was generated and the average values for the fourteen intervals calculated. Three data sets with different input parameters were generated. The results are discussed in the next three subsections.

3.3.1 Synthetic data set 1

The input values for the first set are in Table 3.1 below. The values are not meant to always be physically realistic but are rather meant to stress the technique. The spectral indices, the inertial range break point bp_2, and the variance value in Table 3.1 are in good agreement with the input values. The value of the input parameters C and bp_1 fall within the error margins of the average values in Table 3.1. A useful cross check for this numerical technique is to compare the variance of the original synthetic magnetic field data and the integral of the spectrum produced by the fitting technique. These are also in good agreement.

Parameter	Mean	Std deviation	Input values
Inertial range spectral index	-1.94	± 0.08	-2.00
Energy range spectral index	-0.79	± 0.08	-0.75
C (nT^2/Hz)	1.66E+04	± 0.31E+04	1.72E+04
bp_1 (hrs)	39	± 15	50
bp_2 (min)	44	± 5	45
Average Integral (nT^2)	25.1	± 1.2	N/A
Average Variance (nT^2)	24.8	± 0.9	25

Table 3.1: Averages of the parameters over the whole synthetic data set.

3.3.2 Synthetic data set 2

Parameter	Average	Std deviation	Input values
Inertial range spectral index	-1.67	0.01	-1.67
Energy range spectral index	-1.03	0.18	-1.0
C (nT^2/Hz)	6.94E+03	0.73E+03	6.48E+03
bp_1 (hrs)	50	1	50
bp_2 (min)	30	1	30
Average Integral (nT^2)	25.4	$\pm$ 2.6	N/A
Average Variance (nT^2)	25.4	$\pm$ 1.2	25

Table 3.2: Parameter averages for the second set of synthetic data tested.

After comparing the input and average values in Table 3.2 it is clear that the estimates of the inertial range spectral indices, the two break points as well as the variance and integral values are accurate. The estimates of the parameter C and the energy range spectral index are not as accurate as the other parameters. However, they do agree with the input values in Table 3.2 and are within the error margins quoted.

3.3.3 Synthetic data set 3

Parameter	Average	Std deviation	Input values
Inertial range spectral index	-1.62	0.17	-1.67
Energy range spectral index	-1.00	0.05	-1.00
C (nT^2/Hz)	1.16E+04	0.40E+04	1.25E+04
bp_1 (hrs)	115	18	120
bp_2 (min)	60	9	60
Average Integral (nT^2)	25	$\pm$ 3	N/A
Average Variance (nT^2)	24	$\pm$ 2	25

Table 3.3: Parameter averages for the third set of synthetic data tested.

After considering the average and the input values in Table 3.3, it is clear that the estimates of the energy range spectral indices, the two break points as well as the value of the constant C are accurate. The estimates of the inertial range spectral index, variance and integral, are not as accurate as the other parameters. However, they do agree with the input values in Table 3.3 and are within the error margins quoted.

3.4 Data gaps

The data gaps are introduced to the data sets by removing a section of the data and replacing it with missing data marker values. The data markers indicate the data gaps and are not introduced uniformly. If for instance there is to be a 35% data gap in the interval of data, then the data gaps are introduced at random throughout the data interval until the 35% total is met. The numerical technique is then applied to the data set and the data set is then fitted.

After comparing the fits produced, it is found that the technique performs satisfactory for up to 80% of data gaps. The spectral indices, spectral level C, and the break point bp_2 estimates are in good agreement with the input values listed in Table 3.4. The break point between the low-frequency constant part of the spectrum and the energy range was not considered since it is rarely resolved in actual spacecraft data. The technique would not deliver reliable fits for data gaps larger than 80%.

	Inertial range spectral index	Energy range spectral index	C parameter ($^{nT^2}/_{Hz}$)	bp_2 (min)
Input values	-2.0	-0.75	1.72E+04	45
0%	-2.0	-0.78	1.73E+04	45
10%	-2.0	-0.78	1.65E+04	44
20%	-2.0	-0.78	1.75E+04	45
25%	-2.0	-0.78	1.80E+04	46
30%	-2.0	-0.78	1.78E+04	45
40%	-2.0	-0.78	1.81E+04	46
50%	-2.0	-0.78	1.80E+04	46
60%	-2.0	-0.78	1.66E+04	44
68%	-2.0	-0.77	1.80E+04	46
70%	-2.0	-0.77	1.66E+04	44
80%	-2.0	-0.78	1.80E+04	46
Average	-2.00 ± 0.00	-0.776 ± 0.004	1.76E+04 ± 0.06E+04	45.1 ± 0.8

Table 3.4: Results of the analysis of synthetically generated data with a percentage data omission as indicated.

3.5 Pre-whitening and post-darkening

One method to handle data sets with significant gaps is presented in the work by Bieber et al. (1993) on the basis of time series reconstruction. For this discussion, consider a magnetic field $\mathbf{B}(t) = \mathbf{B}_0 + \delta\mathbf{B}(t)$. The correlation function for the data is then $R_{ii}(\tau) = \langle \delta B_i(t)\delta B_i(t+\tau)\rangle$ where τ is the lag. It is this correlation function which is now altered when implementing the method presented in (Bieber et al., 1993). Begin by redefining the input time series as a difference time series,

$$\Delta\mathbf{B}(t) = \mathbf{B}(t+\Delta\tau) - \mathbf{B}(t). \tag{3.2}$$

Reformulate the correlation function by means of Equation 3.2. Define the correlation function now in terms of differences as $R_{ii}^{(\Delta)}$,

$$R_{ii}^{(\Delta)}(\tau) = \langle \Delta B_i(t) \Delta B_i(t+\tau) \rangle. \tag{3.3}$$

Now rewrite the correlation function of differences (R_{ii}^{Δ}) in terms of the origional correlation function (R_{ii}). Begin by substituting 3.2 in to 3.3. After some algebra and simplification,

$$R_{ii}^{(\Delta)}(\tau) = \underbrace{\langle B_i(t+\tau+\Delta\tau) B_i(t+\Delta\tau) \rangle}_{a} - \overbrace{\langle B_i(t+\tau+\Delta\tau) B_i(t) \rangle}^{b} - \underbrace{\langle B_i(t+\tau) B_i(t+\Delta\tau) \rangle}_{c} + \overbrace{\langle B_i(t+\tau) B_i(t) \rangle}^{d}. \tag{3.4}$$

In order to relate the above expression to the correlation function R_{ii}, define $t' = t + \Delta\tau$.

Term a becomes $\langle B_i(t'+\tau) B_i(t') \rangle$ and this resembles the correlation function R_{ii}. R_{ii} is dependent on τ and not t so that $R_{ii(\tau)}$ is the same for t and t'. Thus term a can be replaced with $R_{ii}(\tau)$. Using the defintion of t' above, term c becomes $\langle B_i(t' - \Delta\tau + \tau) B_i(t') \rangle$ which amounts to $R_{ii}(\tau - \Delta\tau)$.

Consider a substitution of $\tau + \Delta\tau$ for τ in $R_{ii}(\tau)$. $R_{ii}(\tau + \Delta\tau) = \langle B_i(t + \tau + \Delta\tau) B_i(t) \rangle$ and this resembles term b and so term b may be replaced by $R_{ii}(\tau + \Delta\tau)$.

Term d is a straight forward expression for $R_{ii}(\tau)$.

$R_{ii}^{(\Delta)}$ can then be recast as

$$R_{ii}^{(\Delta)}(\tau) = 2R_{ii}(\tau) - R_{ii}(\tau + \Delta\tau) - R_{ii}(\tau - \Delta\tau). \tag{3.5}$$

This correlation function can then be integrated to form a power spectrum of differences. Taking the Fourier transform of Equation 3.5 term by term yields

$$F^{\Delta}(\omega) = 2F(\omega) - e^{-j\Delta\tau\omega} F(\omega) - e^{j\Delta\tau\omega} F(\omega); \tag{3.6}$$

where $F^{\Delta}(\omega) = \mathscr{F}\{R_{ii}^{\Delta}(\tau)\}$ and $F(\omega) = \mathscr{F}\{R_{ii}(\tau)\}$ are the Fourier transforms of the correlation functions. The exponential terms in Equation 3.6 are introduced when using the second Fourier shift theorem which states that $\mathscr{F}\{f(t-a)\} = e^{-ja\omega} F(\omega)$. The shift theorem was applied to equation 3.5 with $t = \tau$ and $a = \Delta\tau$. The Fourier transform of a correlation function is a power spectrum (Bieber, 1996). Equation 3.6 can then be reformulated as

$$P_{ii}^{\Delta}(f) = 2P_{ii}(f) - e^{-j\Delta\tau\omega} P_{ii}(f) - e^{j\Delta\tau\omega} P_{ii}(f) \tag{3.7}$$

and can be simplified as follows:

$$
\begin{aligned}
P_{ii}^{\Delta}(f) &= P_{ii}(f)\Big[2 - \Big(e^{-j\Delta\tau\omega} + e^{j\Delta\tau\omega}\Big)\Big] \\
&= 2P_{ii}(f)\Big[1 - \cos(\omega\Delta\tau)\Big] \\
&= 2P_{ii}(f)\Big[1 - \cos(2\pi f\Delta\tau)\Big] \\
&= 2P_{ii}(f)\Big[1 - \cos^2(\pi f\Delta\tau) + \sin^2(\pi f\Delta\tau)\Big] \\
&= 2P_{ii}(f)\Big[\sin^2(\pi f\Delta\tau) + \sin^2(\pi f\Delta\tau)\Big] \\
&= 4P_{ii}(f)\sin^2(\pi f\Delta\tau).
\end{aligned}
$$

Therefore, a power spectrum can be rewritten in terms of the power spectrum of differences as

$$P_{ii}(f) = \frac{P_{ii}^{\Delta}(f)}{4\sin^2(\pi f\Delta\tau)}. \tag{3.8}$$

The power spectrum thus goes through a two-step method. The use of the differences in the magnetic field pre-whitens the magnetic field data. Equation 3.8 is the filter which then performs a "post darkening" of the spectrum (Bieber, 1996).

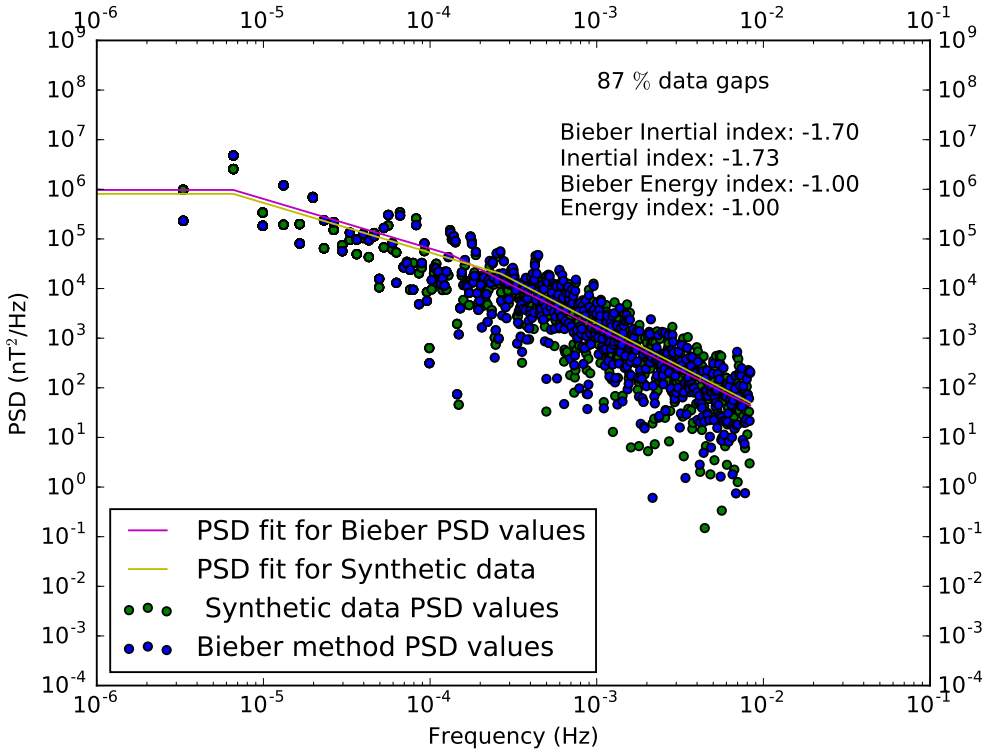

Figure 3.3: Bieber method applied to a synthetic data set with 87 % data gap as in the analysis of Bieber et al. (1993).

This Bieber (1996) technique is applied to two intervals of the first synthetic data set, each with a different percentage of data omission, shown in Figure 3.3. The aim is to test how this filtering technique responds to different amounts of missing data. For each interval, the power spectrum from the numerical technique (without filtering) is indicated by the green symbols. The Bieber-corrected PSD is indicated by the blue symbols. The fits made to both PSD spectra are indicated in yellow and purple, respectively. Comparing these two data sets clearly illustrates that even when there is a large percentage of data gaps, the Bieber filtering method does not make improvements of more than around two percent to the fits. Even in this extreme case of very large data gaps, the gain of Bieber technique is outweighed by the added complexity and processing time.

3.6 Implementation of theoretical pickup ion spectra

The theoretical equations 2.3 and 2.4 are used to generate synthetic data which is combined with a standard three-stage spectrum. The total energy density of the pickup ion contribution was arbitrarily chosen to be 40% of that of the three-stage spectrum. The results of such an implementation are shown in Figure 3.4 below.

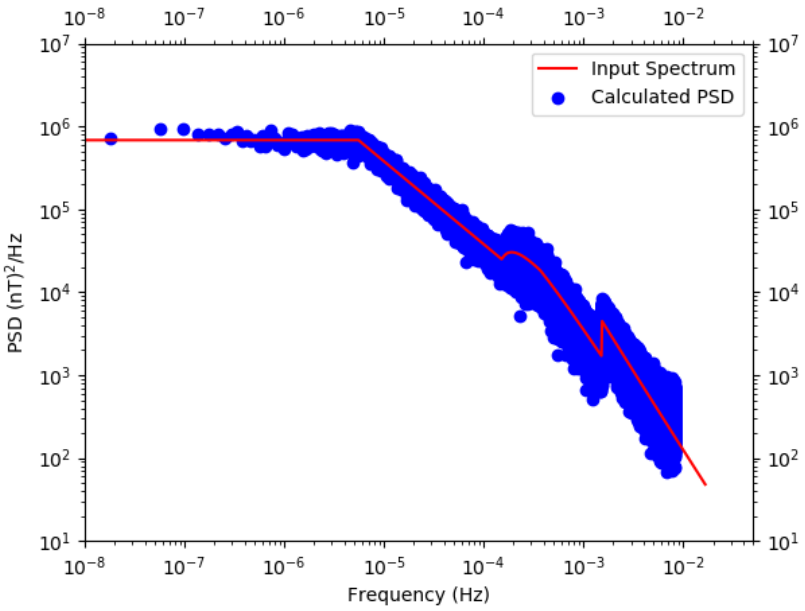

Figure 3.4: The input spectrum used to generate the data modified by pickup ions is indicated in red. The results of the numerical analysis, by the technique discussed in this paper, are indicated in blue.

The enhancement between 10^{-3} and 10^{-2} Hz corresponds with that expected in Figure 2.6. The enhancement between 10^{-4} and 10^{-3} Hz corresponds with that expected in Figure 2.5. The conclusion which can be drawn from the investigation in this section is that if the wave excitation of pickup ions presents a particular feature in the power spectrum, the numerical technique will be able to identify it.

3.7 Summary

This chapter introduces the concept of a turbulence power spectrum and provides a numerical technique that can be used to analyse the power spectrum. The numerical technique is benchmarked using synthetic data. More on the synthetic data and how it is generated can be found in Appendix A. Three different frequency ranges are defined and each spectral index is optimized using the numerical technique. These estimates are then compared to the input values and show good agreement with the input values over the frequency range considered. The effect of missing data on the results is tested and shows that the technique delivers satisfactory estimates until the data gaps amount to 80% of the data set. The pre-whitening and post-darkening power spectra filters discussed in Bieber et al. (1993) were applied to the data in the current project. The results show that these filters add little value to the current analysis which in turn confirms how well the numerical technique works without aid. Finally, the theory of pickup ion spectra discussed in the previous chapter is implemented for a final test of the numerical technique in this chapter. The analysis shows that if pickup ion signatures are present, the technique can with confidence resolve them.

Chapter 4

Voyager 1 analysis

4.1 Introduction

The magnetic field data collected by the Voyager 1 spacecraft from 1977 to 1990, presented in RTN coordinates, is used in this analysis. The numerical technique, as discussed in Chapter 3 is used to calculate the power spectral density (PSD) of the N component as a function of frequency for consecutive 13-day intervals spanning the whole period. The spectra are binned by putting 10 values in a frequency bin. The helium and proton gyrofrequencies were also calculated for each interval. The results of such analyses for each year are recorded in Tables (B1-B14) in Appendix B. Before any data processing could begin, it was noticed that the data files were not in a satisfactory condition for use in this analysis. After applying some pre-processing techniques as discussed in the next section, the data was used for the analyses in the following sections.

4.2 Data filtering

The raw Voyager 1 data which was used in this analysis was obtained from `https://spdf.gsfc.nasa.gov/pub/data/Voyager/vgrmag-data/summary/`. The analysis of the Voyager data presented two main problems. The first is that there are a large number of missing data records. Missing data is "filled in" by generating evenly spaced dummy time records with resolution as close as possible to the nominal 48 s. The corresponding entries for magnetic field and other data are filled with "No data" markers. There are in fact four distinct resolutions present in the data set: 46.656 s, 47.520 s, 48.384 s, and 49.248 s. After filling in the missing records, both the average and the median resolution are very close to 48 s.

The second feature deemed to be problematic was the presence of spurious data peaks of large amplitude that pose a challenge to the identification of pickup ion signatures. These peaks were eliminated by using the following filtering process (Burger 2018, private communication). Firstly, the data for each yearly interval is divided up in to 2.5 day intervals (this amounts to 150 data blocks). Each of the data blocks are then filtered independently. The Parker field decreases by about r^{-1} in the ecliptic, and the maximum value of the field at 1 au is around 12 nT. The first conservative filter was applied to eliminate all records where magnetic field values have a magnitude larger than $12r^{-1}$ nT.

Next, the magnitude of the field for a given record was compared with the RMS value for the whole block, and eliminated if it was more than three times larger. These two filtering methods removed any spurious data peaks before the data was used for analysis. Figure 4.1 (a) shows the power spectrum for a thirteen-day interval starting at 1981.891 using the raw data, while Figure 4.1 (b) shows the power spectrum after filtering.

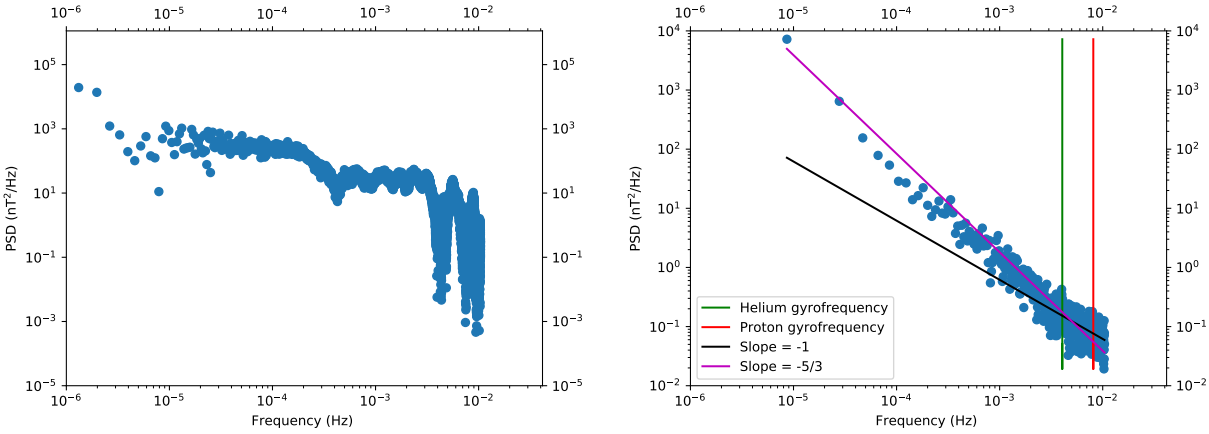

(a) (b)

Figure 4.1: Power spectral density as a function of frequency for decimal year 1981.819 at a heliocentric radial distance of 11.6 au and heliographic latitude 7.96° (a) before pre-processing and (b) after processing the data.

The spectrum, using the raw data in panel (a), bears almost no resemblance to the spectrum after filtering in panel (b). The latter spectrum has a spectral index of close to $-5/3$ at low frequencies that changes to about -1 at high frequencies. More importantly, there is a clear enhancement at the helium gyrofrequency (vertical green line) indicating the presence of pickup ions.

4.3 Spectral forms and features

After the pre-processing of the Voyager data was complete, four distinct spectral forms were apparent along with two distinct spectral features. The spectral forms discussed here describe the form of the background spectrum and the spectral features are enhancements above the background spectrum. The lowest frequency resolved in this analysis is around 6×10^{-6} Hz or just less than two days. However, it is apparent that the number of Fourier modes is only high enough to give a reasonable idea of the spectral shape at frequencies above about 10^{-4} Hz.

4.3.1 Spectral forms

Type 1 spectra

These spectra are representative of what is usually observed near Earth in this frequency range. An energy range with spectral index -1 at lower frequencies is followed by the

ubiquitous Kolmogorov inertial range with spectral index $-5/3$ at higher frequencies, (an example of which is shown in Figure 4.2).

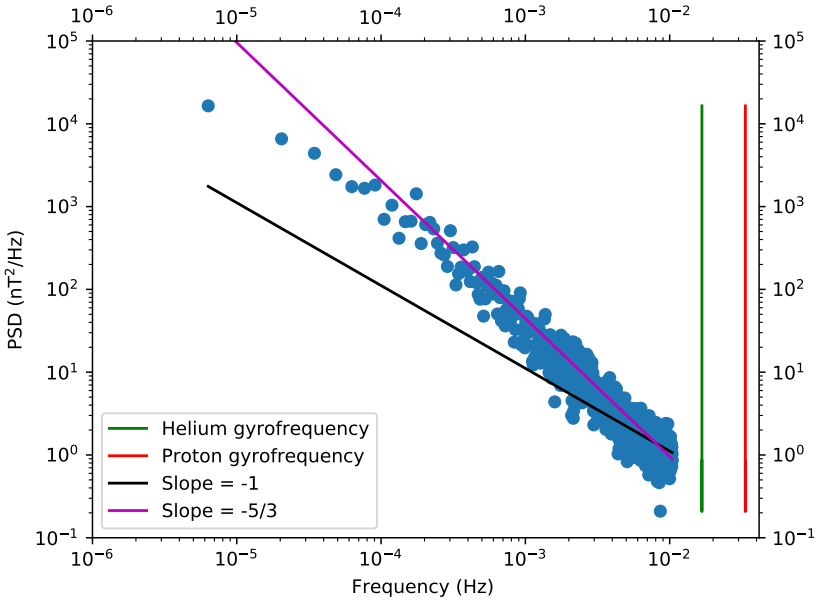

Figure 4.2: Example of a Type 1 spectrum seen in 1977.928 at a heliocentric radial distance of 1.65 au and heliographic latitude 2.33°. The helium and proton gyrofrequencies are indicated on the figure in green and red, respectively. The lines with slopes -1 and $-5/3$ are fits by eye. They will be shown on all graphs in this section 4.3 and are meant to guide the eye. This figure corresponds to entry 8 in Table B1 of Appendix B.

A typical timescale for the breakpoint between the different spectral indices at Earth is between one and four hours (Borovsky, 2012). This equates to between 2.78×10^{-4} and 6.95×10^{-5} Hz, respectively. The analysis by Nel (2015) of almost 40 years of data suggests an average value of about one hour. The last Type 1 spectrum is observed at a radial distance of 3.79 au (Table B2 entry 17) which agrees with the fact that no Type 1 spectra should be observed beyond at most 9 au.

Type 2 spectra

These spectra only have a Kolmogorov inertial range; an example of which is shown in Figure 4.3.

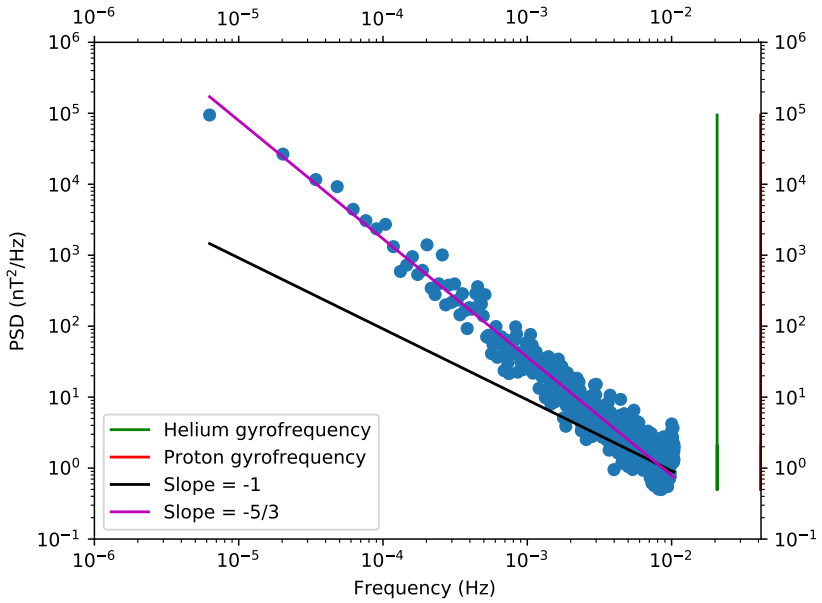

Figure 4.3: Example of a Type 2 spectrum seen in 1978.107 at a heliocentric radial distance of 2.31 au and $-0.546°$ heliographic latitude. This figure corresponds to entry 4 in Table B2 of Appendix B.

Type 3 spectra

If the power spectral density has a spectral index of approximately $-5/3$ at low frequencies and a spectral index of -1 at high frequencies, then the spectrum is classed as Type 3. An example of such a spectrum is shown in Figure 4.4 (Table B10 entry 3). This spectral form becomes dominant beyond 25 au.

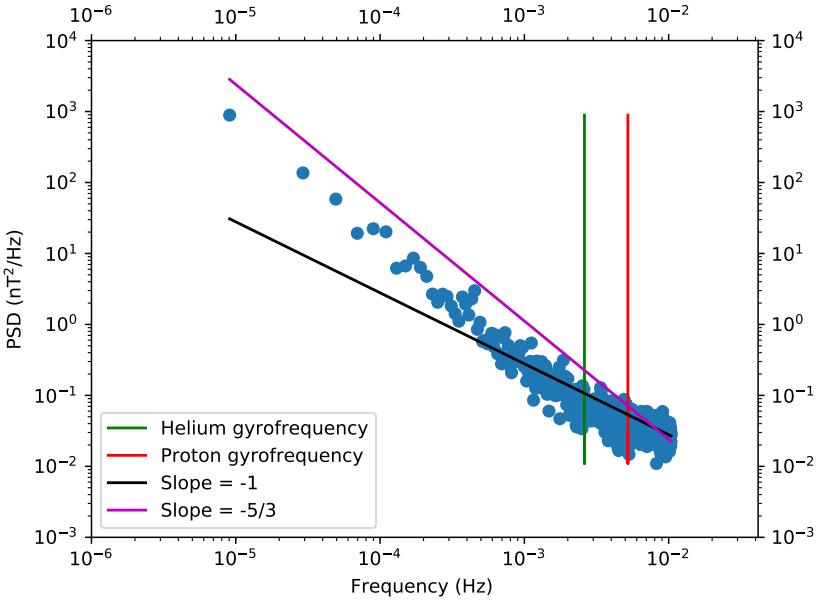

Figure 4.4: Example of a Type 3 spectrum seen in 1982.249 at a heliocentric distance of 12.7 au and 12.7° heliographic latitude. The helium and proton gyrofrequencies are indicated on the figure in green and red, respectively. This figure corresponds to entry 8 in Table B6 in Appendix B.

Frequencies larger than $\sim 5 \times 10^{-5}$ Hz suffer from considerable instrument noise (Burlaga et al., 2018). Additionally, the flattening of a power spectral density is expected when approaching the noise level of the instrument (0.005 nT for the Voyager magnetometer (Burlaga et al., 2018)). Burlaga et al. (2015) suggest that the noise at this flattened part of the spectrum (see Figure 4.5) could also be what is known as "Guassian white noise". Guassian white noise is of a ergodic nature and defined by a zero mean (Marmarelis, 2004). For this study, it is assumed that this f^{-1} behaviour is due to spacecraft noise.

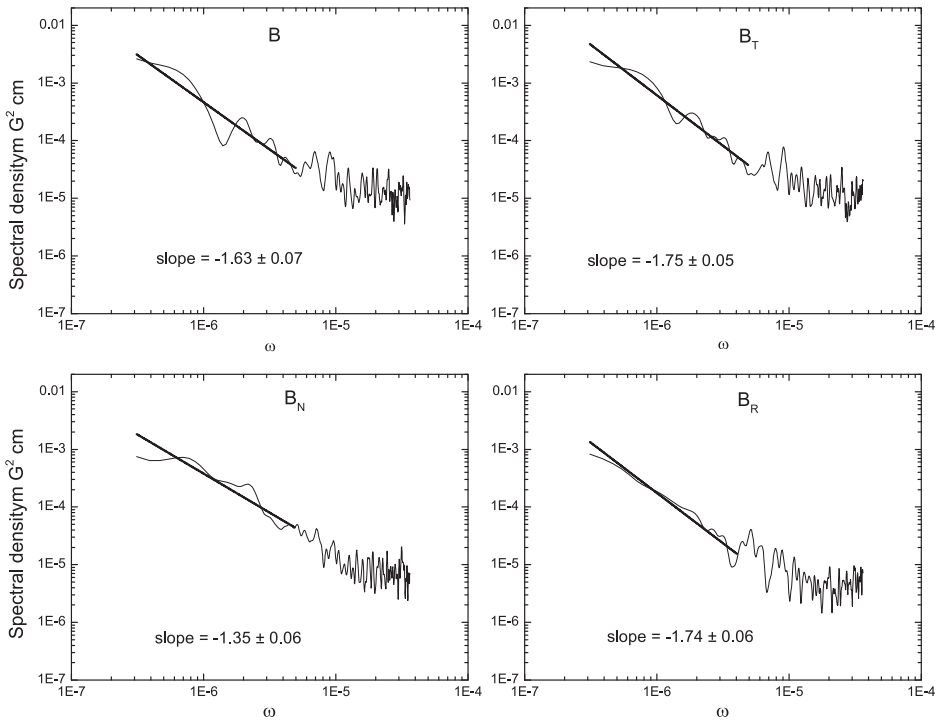

Figure 4.5: Straight lines indicate the part of the spectrum which is consistent with Kolmogorov theory. Burlaga et al. (2015) state that high frequencies are influenced by instrument noise and are thus not consistent with Kolomogorov theory. The part of the spectrum influenced most strongly by instrument noise flattens.

Type 4 spectra

Spectra with an index of -1 only, constitute this category. These spectra are dominated by f^{-1} spacecraft noise.

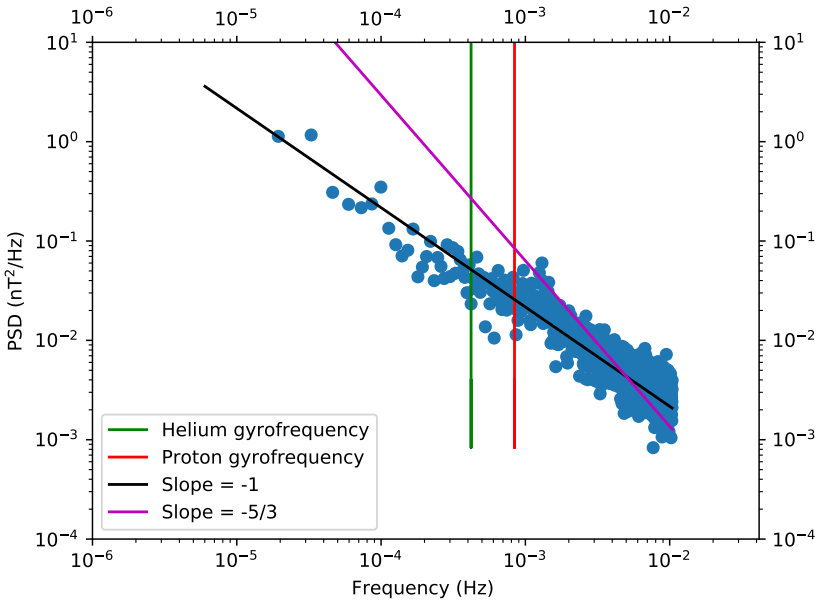

Figure 4.6: Example of a Type 4 spectrum seen in 1988.570 at a heliocentric radial distance of 34.7 au and 34.9° heliographic latitude. This figure corresponds to entry 17 in Table B12 in Appendix B.

4.3.2 Spectral features

The two specific spectral features discussed in this section are sharp data peaks and pickup ion signatures superimposed on background spectra above.

Sharp PSD spikes

An example of this feature is shown in Figure 4.7.

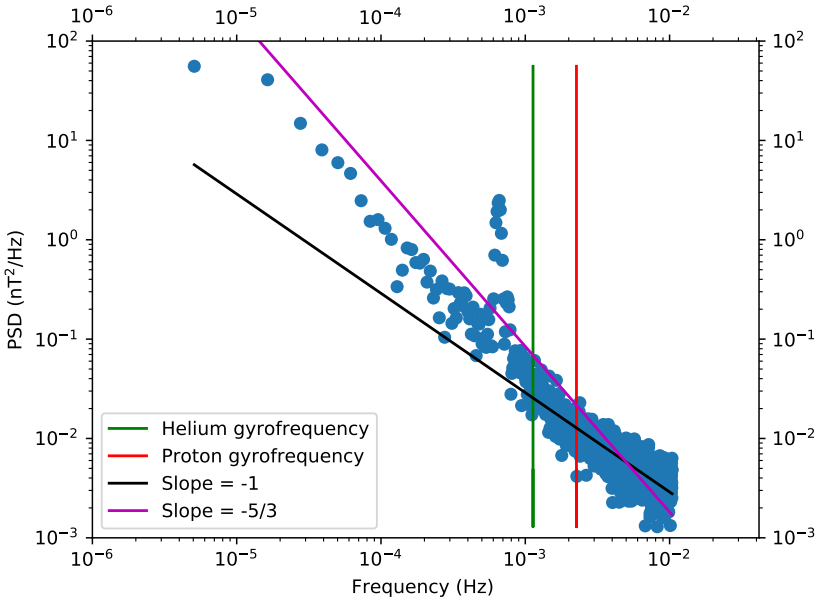

Figure 4.7: Example of a sharp PSD spike around 5×10^{-4} Hz seen in 1990.548 at a heliocentric radial distance of 41.9 au and 37.06° heliographic latitude. This figure corresponds to entry 16 in Table B14 in Appendix B.

If the peak is present, it is seen clearly at a frequency close to 5×10^{-4} Hz. Fraternale et al. (2016) suggest that if the peak was as a result of signal reconstruction it should appear in every interval of processed data. However, this is not the case for the present study. Fraternale et al. (2016) concluded that it could be a harmonic of the data sampling frequency. Fraternale et al. (2016) came to this conclusion after observing this spike at a harmonic frequency of their sampling frequency in Voyager 1 velocity data. The origin of this peak does not appear to be related to pickup ions. It will be noted in the present study but not analysed.

Helium and proton pickup ions

Helium and proton pickup ions may be identified by wave signatures close to the helium and proton gyrofrequencies (Hz) given by

$$f = \frac{qB}{2\pi m} \quad . \tag{4.1}$$

The helium gyrofrequency is obviously smaller than the proton gyrofrequency since the mass of a proton is smaller than that of the helium. The pickup ion signatures will be apparent only when the gyrofrequencies are lower than the Nyquist frequency for the particular data set. The magnetic field dataset has a resolution of 48 s, which means a Nyquist frequency of 0.042 Hz. Figures 4.8 and 4.9 show the gyrofrequency as a function of radial distance in au. The radial distance at which the gyrofrequency equals the Nyquist frequency is the radial distance at which pickup ion signatures are expected to begin being observable in the spectra. Figure 4.8 indicates that proton gyrofrequency signatures are expected to move into the spectrum between 7 and 11 au. Figure 4.9 indicates that helium gyrofrequency signatures are expected to move into the spectrum between 5 and 10 au. The magnetic field values used are those measured by Voyager 1, as a function of time, as the Voyager spacecraft moves throughout the heliosphere. Throughout the analysis of Voyager data, an averaging period of 13 days was used which amounts to a radial distance of 0.13 au. The helium and proton gyrofrequencies are thus binned by 0.13 au and are then plotted as a function of radial distance.

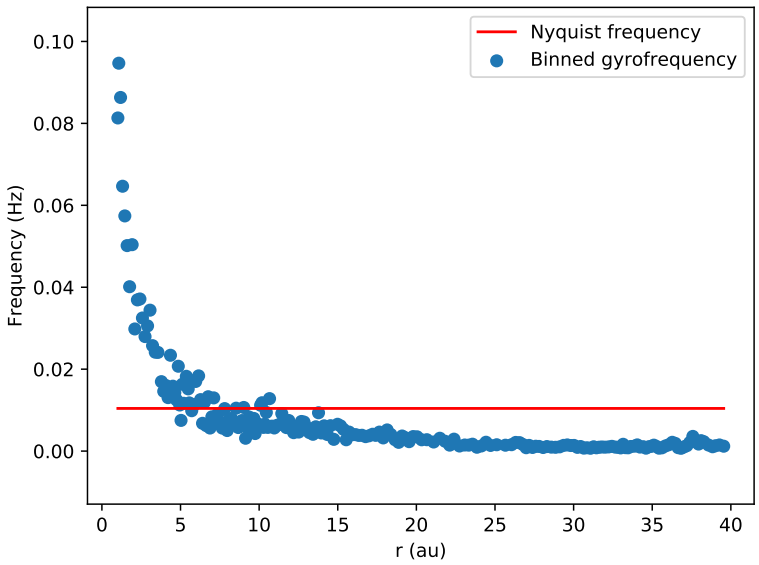

Figure 4.8: Proton gyrofrequency as a function of radial distance in au. The Nyquist frequency is plotted with a red line.

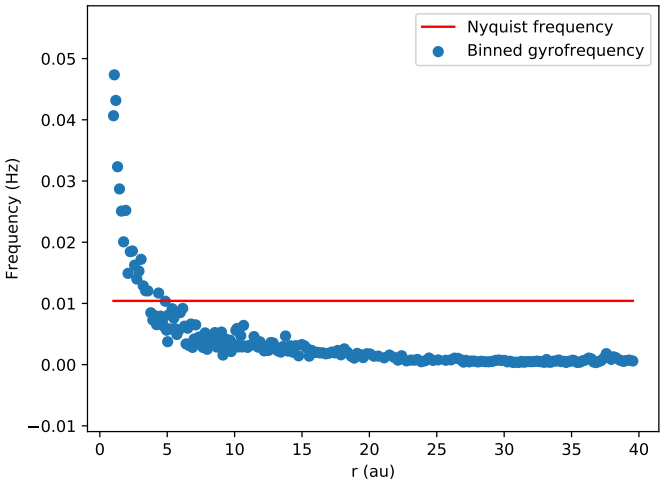

Figure 4.9: Helium gyrofrequency as a function of radial distance in au.

A plot of the radial distance of the Voyager spacecraft, as function of time, is instrumental in determining when pickup ion signatures should be observed. Figure 4.10 indicates that the Voyager spacecraft moves between 5 au and 11 au during the time interval $1978 - 1981$ at a speed of around 3.2 au/year. The first pickup ion signatures are thus expected to appear during or after 1978.

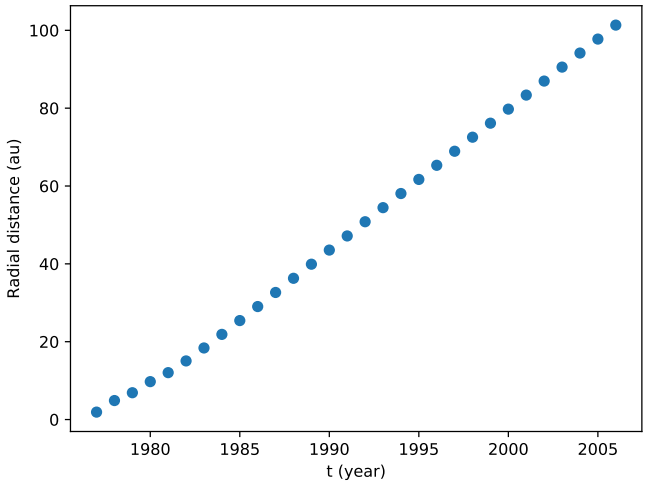

Figure 4.10: Radial distance of Voyager 1.

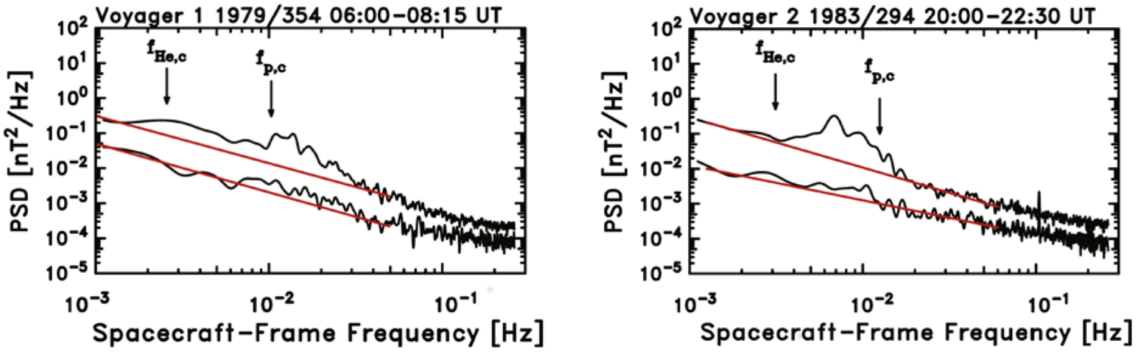

(a) (b)

Figure 4.11: Pickup ion observations from Hollick et al. (2018a). The red lines indicate the background spectra in each panel. Panel (a) is an example of pickup ion peak identification in 1979.970 at a heliocentric radial distance of 6.81 au and $-5.416°$ heliographic latitude. The peaks identified here coincide with entry 28 in Table B3. Panel (b) is an example of pickup ion peak identification in 1983.806 at 17.74 au and 22.66° heliographic latitude. The peaks identified here coincide with entry 23 in Table B7.

Pickup ion signatures, such as those identified here in Figure 4.11 from Hollick et al. (2018b) are very useful when identifying possible pickup ion signatures from data. Figure 4.11 panel (a) clearly shows the pickup ion peaks, associated with pickup helium and hydrogen, at the respective frequencies indicated by the arrows in the figure. Panel (b) shows a pickup ion peak associated with hydrogen which is indicated by the arrow at the proton gyrofrequency. Burlaga et al. (2018) also identify the small enhancement above the background spectra at the helium gyrofrequency in this figure as a pickup ion peak (entry 23 in Table B7 is an example of this).This highlights the need to distinguish between possible and probable peaks. A probable pickup ion peak is one which appears at the gyrofrequency and is a clear enhancement above the background spectrum. A possible pickup ion peak is one which appears at the gyrofrequency but is not a significant enhancement above the background spectrum. Only probable pickup ion peaks are recorded in the Tables and the figures included in this text (peaks identified only as possible require further analysis before being able to conclude whether or not these are peaks identified as pickup ion peaks).

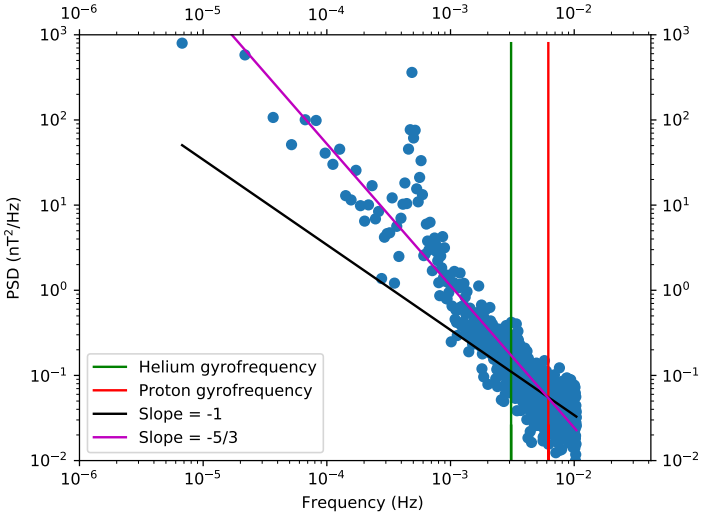

Figure 4.12: Example of pickup helium in 1979.785 at a heliocentric radial distance of 6.36 au and −5.51° heliographic latitude. This figure corresponds to entry 23 in Table B3 in Appendix B.

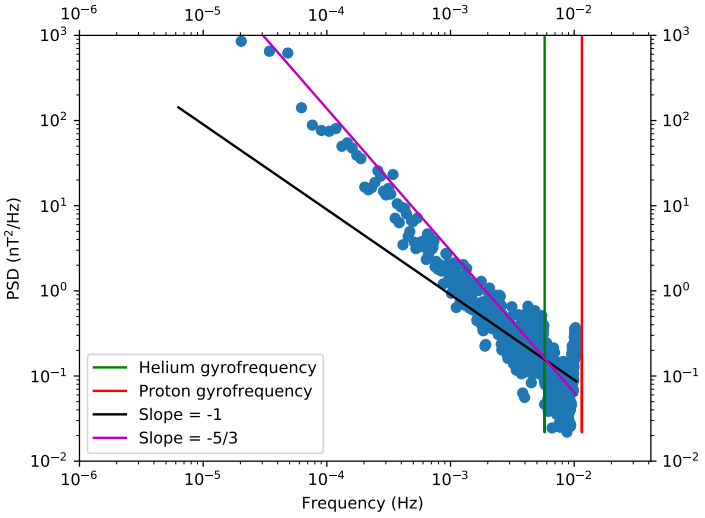

Figure 4.13: Power spectral density as a function of frequency for decimal year 1979.820 at heliocentric radial distance of 6.44 au and −5.50° heliographic latitude. This figure corresponds to entry 24 in Table B3 in Appendix B.

The first pickup ion peak, for helium, appears around mid-1978 at a radial distance of about 4 au (Figure 4.12; entry 18 in Table B3). Three peaks are seen mid- to late 1979 at a radial distance of about 6.5 au; two helium and the first proton peak (Figures 4.12 and 4.13; Table B3 entries 23 and 24). Hollick et al. (2018) observed both helium and proton peaks during the first interval; in the present study only a helium peak was identified. In the second interval, both helium and proton peaks are seen in the present study whereas Hollick et al. (2018) did not observe helium peaks. Both protons and helium were next

observed only in the beginning of 1982 (Figure 4.15; Table B6 entry 11). This particular interval was not analysed by Hollick et al. (2018). During 1983, no less than six pickup ion peaks were identified in the current study: protons only (Figure 4.16; Table B7 entry 1), helium only (Figure 4.18; Table B7 entry 12), and twice both peaks were seen in the same interval (Figures 4.17 and 4.17; Table B7 entries 6 and 23). Only the latter interval was analysed by Hollick et al. (2018) and they also report peaks for both helium and protons. The next observation was only in mid-1986 (Figure 4.21; Table B10 entry 17) for protons, in agreement with the observations of Hollick et al. (2018) who similarly did not see helium peaks. Four more proton peaks are seen in the present study but in intervals not analysed by Hollick et al. (2018). These are in late 1987 (Figure 4.22; Table B11 entry 24), mid-1988 (Figure 4.19; Table B12 entry 15), and in the beginning of 1989 (Figure 4.20 and 4.23; Table B13 entries 7 and 9).

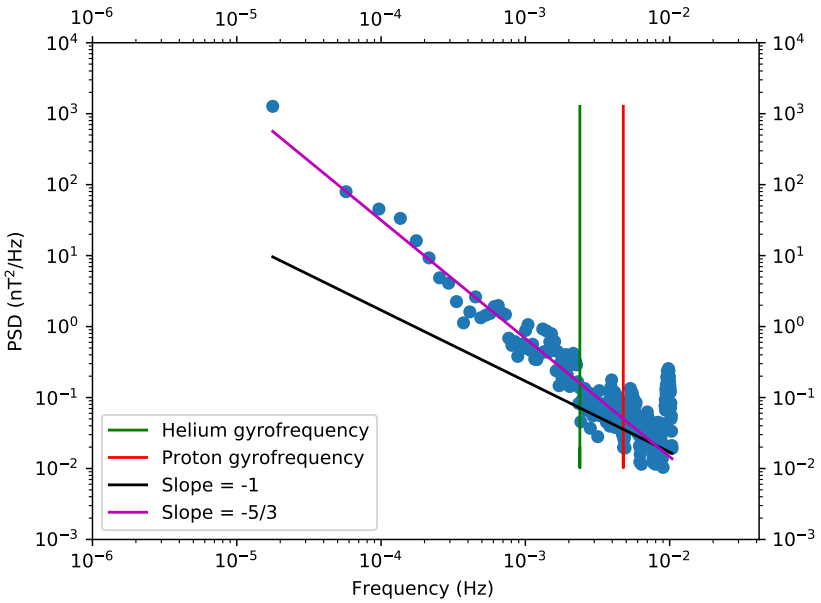

Figure 4.14: Power spectral density as a function of frequency for decimal year 1980.959 at a heliocentric radial distance of $9.67au$ and $-3.19°$ heliographic latitude. This figure corresponds to entry 28 in Table B4 in the Appendix B.

Another important feature to notice in Figure 4.14 is the upturn of the spectrum at high frequencies. This is seen in Bieber et al. (1993) and comes about as a result of aliasing at these high frequencies. This feature is also apparent in intervals (1985 #10) and (1979 #24) where the spectrum peaks at high frequencies (on order 10^{-2}). The observation in Figure 4.15 is also a new observation.

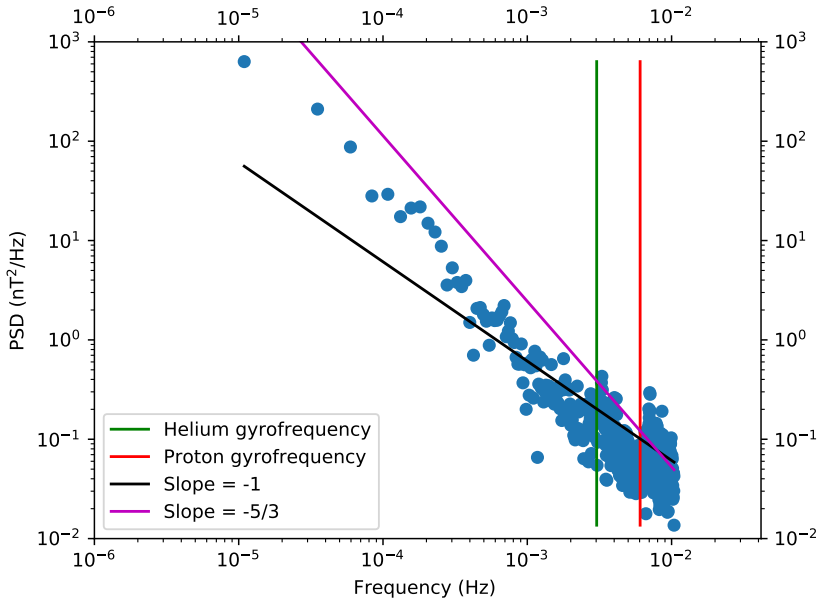

Figure 4.15: Power spectral density as a function of frequency for decimal year 1982.356 at a heliocentric radial distance of 13.1 au and 13.2° heliographic latitude. This figure corresponds to entry 11 in Table B6 in Appendix B.

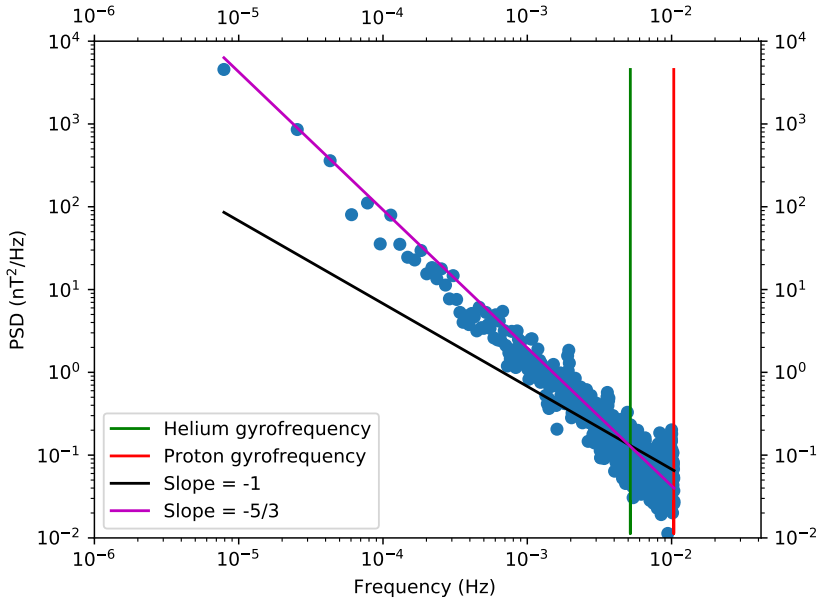

Figure 4.16: Power spectral density as a function of frequency for decimal year 1983.000 at a heliocentric radial distance of 15.1 au and 18.04° heliographic latitude. This figure corresponds to entry 1 in Table B7 in Appendix B.

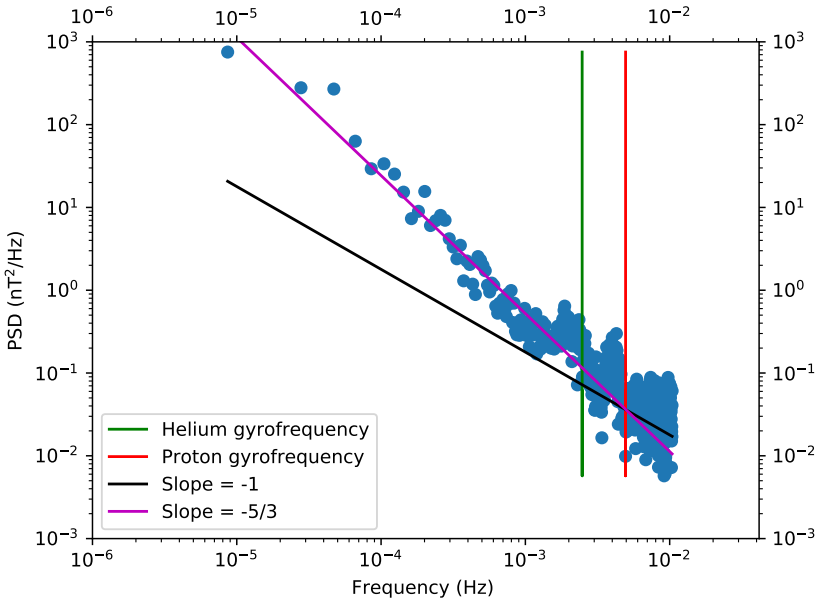

Figure 4.17: Power spectral density as a function of frequency for decimal year 1983.178 at a heliocentric radial distance of 15.6 au and 19.2° heliographic latitude. This figure corresponds to entry 6 in Table B7 in Appendix B.

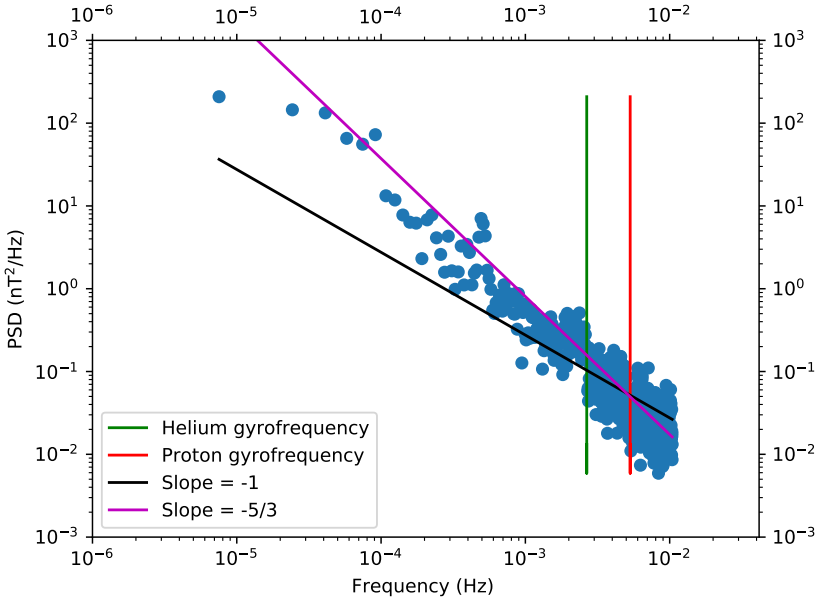

Figure 4.18: Power spectral density as a function of frequency for decimal year 1983.392 at a heliocentric radial distance of 16.3 au and 20.5° heliographic latitude. This figure corresponds to entry 12 in Table B7 in Appendix B.

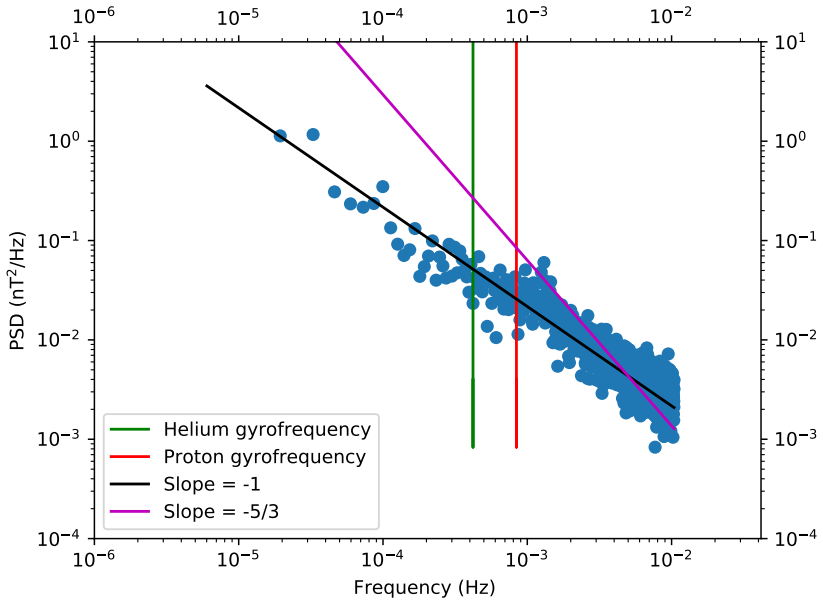

Figure 4.19: Power spectral density as a function of frequency for decimal year 1988.570 at a heliocentric radial distance of 34.7 au and 34.9° heliographic latitude. The proton and helium gyrofrequencies are indicated on the figure. This figure corresponds to entry 15 in Table B12 in Appendix B

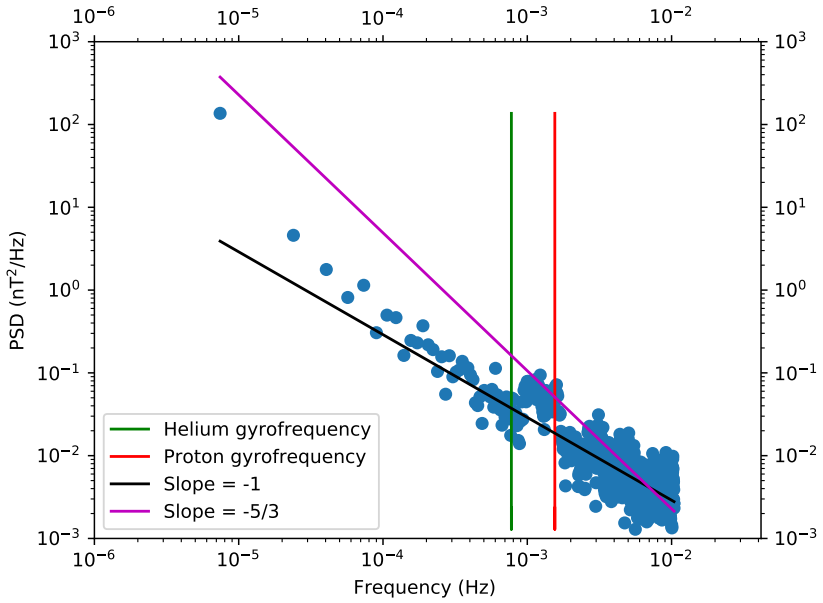

Figure 4.20: Power spectral density as a function of frequency for decimal year 1989.215 at a heliocentric radial distance of 37.7 au and 35.7° heliographic latitude. The proton and helium gyrofrequencies are indicated on the figure. This figure corresponds to entry 6 in Table B13 in Appendix B.

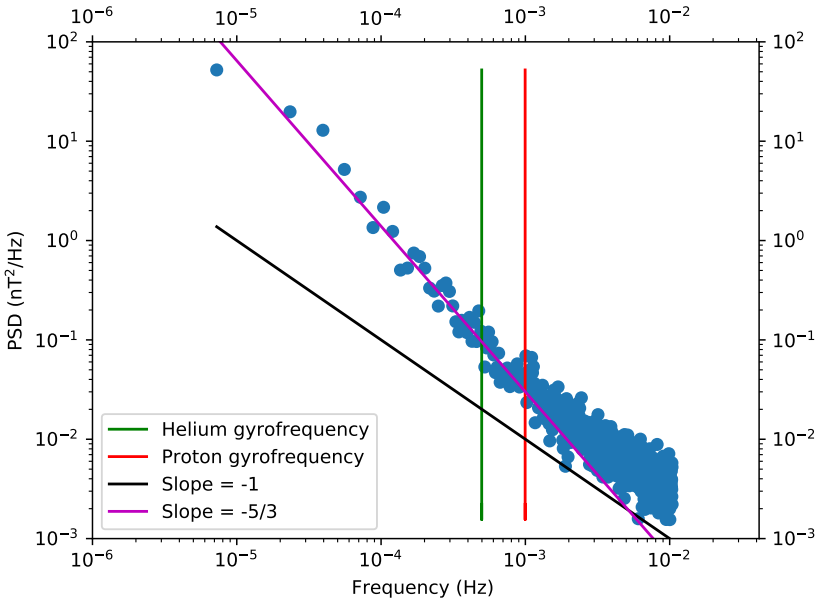

Figure 4.21: Power spectral density as a function of frequency for decimal year 1986.571 at a heliocentric radial distance of 27.5 au and 31.6° heliographic latitude. This figure corresponds to entry 17 in Table B10 in Appendix B.

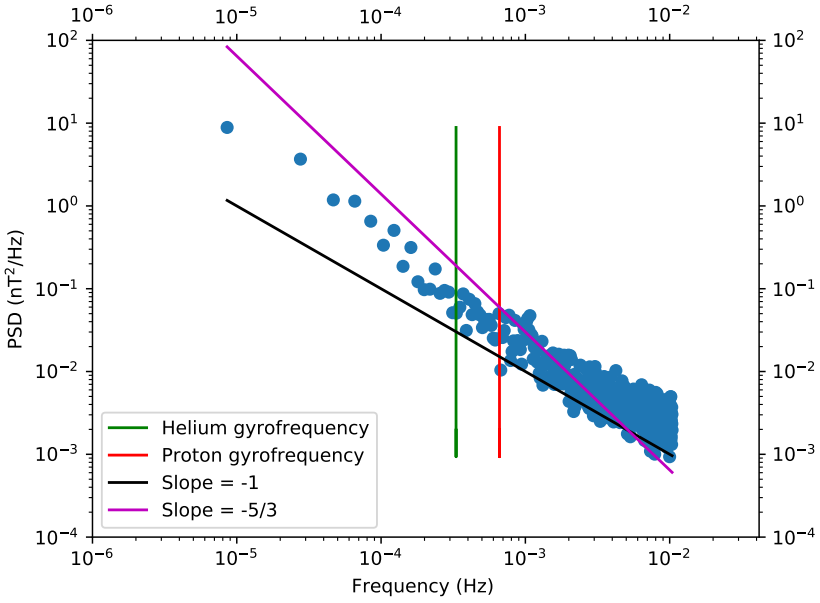

Figure 4.22: Power spectral density as a function of frequency for decimal year 1987.820 at a heliocentric radial distance of 32.0 au and 33.9° heliographic latitude. This figure corresponds to entry 24 in Table B11 in Appendix B.

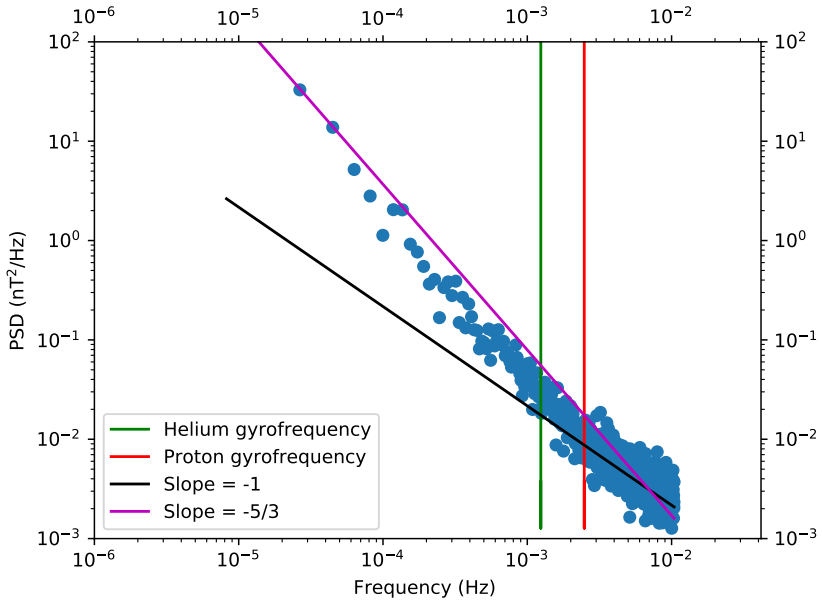

Figure 4.23: Power spectral density as a function of frequency for decimal year 1989.322 at a heliocentric radial distance of 37.5 au and 35.8° heliographic latitude. This figure corresponds to entry 9 in Table B13 in Appendix B

4.3.3 Remarks

The turbulence evolves from Type 1 to Type 3 as Voyager 1 moves away from the Sun. This implies that as the distance traveled in radial distance by the Voyager 1 spacecraft increases, the spectral index transitions between having a value of -1 at low frequencies to having a value of -1 at high frequencies. The largest number of data intervals per year with a Type 3 spectrum was recorded for the year 1988. The Type 3 spectrum is most frequent throughout the period 1985 to 1990. The Type 3 spectrum first appears in 1978 with one data interval of Type 3 (15 in Table B2). The f^{-1} contribution to the Type 3 spectra becomes significant from year 1979. Overall, the most commonly observed spectral form is a Type 2 spectrum. This is a spectral form which resembles the turbulent inertial range with a spectral index of $-5/3$. Type 4 spectra are most frequent in 1988. There is only one pickup ion signature observed on a background spectrum of Type 4. The pickup ion signatures may be hidden or overshadowed by the spacecraft noise when this noise is at the helium and proton gyrofrequencies.

The first pickup ion signature is observed in 1978 and is at the helium gyrofrequency. The first signature at the hydrogen gyrofrequency is seen in 1979. In total, there are 18 observations; 7 of which are at the helium gyrofrequency and 11 which are at the hydrogen gyrofrequency. There are five data intervals in this analysis which agree with the observations detailed in Hollick et al. (2018b,a,c) (6 agreed pickup ion observations). New pickup ion observations are found in eight data intervals in this analysis (10 new pickup ion observations). The fact that the f^{-1} noise becomes more prominent at larger radial distances is because the level of the underlying turbulence spectrum is decreasing. This causes the break between the inertial- and the noise range to move to lower frequencies.

Consider that over the period of analysis the break point frequency moves from 0.004 to 0.001 Hz whilst the level of the f^{-1} spectrum drops from $\sim 10^{-1}$ to $\sim 10^{-3}$ nT^2Hz^{-1} at 10^{-2} Hz as in Figure 4.24.

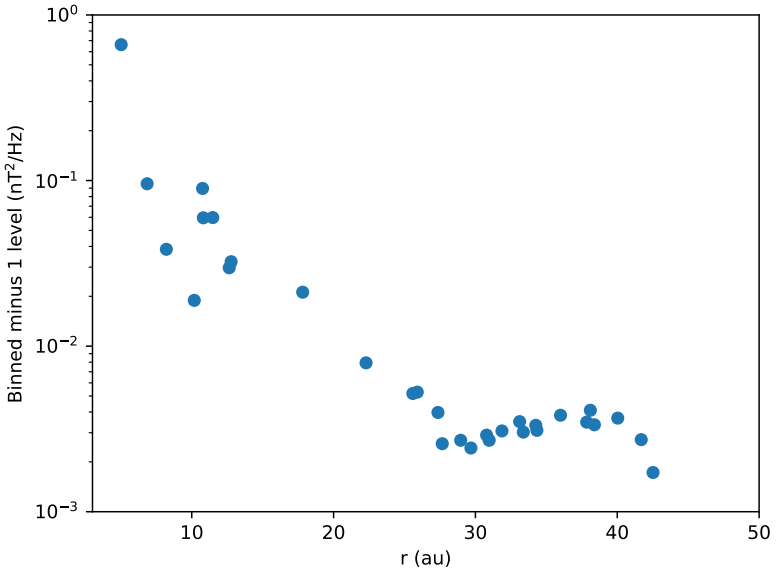

Figure 4.24: Level of f^{-1} noise spectrum at 10^{-2} Hz as a function of radial distance over the data period.

So, how would the noise part of the spectrum influence the total energy density. Would its presence lead to significant errors when the variance is calculated? How important is it that the turbulence spectrum used in scattering models for cosmic-ray modulation models includes this artifact? To answer such questions, a simple calculation is done over the frequency range used in the current analysis. The relative contribution to the total area of a Kolmogorov inertial range and the f^{-1} spectrum is calculated for different break frequencies between these two ranges. Since both are power laws, the absolute levels play no role. The results are shown in Table 4.1. The break is typically at frequencies at or above 10^{-4} Hz.

High-frequency break f^{-1} (Hz)	f^{-1} contribution (%)	$f^{-5/3}$ contribution (%)
5×10^{-5}	57	43
5×10^{-4}	12	88
5×10^{-3}	0.68	99.32

Table 4.1: Contribution to a total power spectrum by the parts of the power spectrum described by a -1 or $-5/3$ slope, respectively.

It, therefore, follows that the f^{-1} part of the spectrum does not make up a significant percentage of the background spectrum in this analysis. This also means that there is no need to account for f^{-1} behaviour in cosmic-ray modulation up to the radial distances

covered in the current project.

One last remark revolves around the spike at 5×10^{-4} Hz. There were 26 spikes in total across the data period with the first spike appearing in 1978. The number of spikes, occuring within a year of data, increases with radial distance. The presence of these spikes do not effect the form of the background spectra.

4.4 Radial dependence of the magnetic field variance

Consider the variance of the magnetic field data as being a function with both a radial and time dependence denoted by $S^2B(r,t)$. In order to observe only the time dependence of the variance, the radial dependence should be removed and vice versa. In this section, the aim is to try and highlight the radial dependence by removing the time dependence.

Take the solar wind to have a speed of $V_w = 440$ km.s^{-1} and assume that it is constant over the period of study (1977 to 1990). Denote the time at which the solar wind left the sun as t_0 and the position as r_0. Denote the variance at the position r_1 of the voyager spacecraft at a time t_1 as $S^2B(r_1,t_1)$. The aim here is to determine at what time (t_0) the plasma left the sun by tracing back in time from the point (t_1,r_1) to the point (t_0,r_0). The variances measured by Voyager 1 at (t_1,r_1) are then normalised by using the values of the variance measured at the reference point (t_0,r_0). The properties of the solar wind are frozen in at 1 au and the reference point will be placed at 1 au. The reference variance values (at 1 au) will be retrieved from data recorded by the IMP spacecraft over the period of study.

Let the plasma take a period of time ($\Delta\tau$) to travel from the Sun at time t_0 to the location of the Voyager spacecraft at a time t_1. These times are related by $t_1 = t_0 + \Delta\tau$. The travel time $\Delta\tau$ may then be written in terms of the average solar wind speed V_w and the position r_1 by using $V_w\Delta\tau = r_1$. The above expressions when combined can then be used to work backwards and calculate the time the plasma left the Sun. Equation 4.2 relates the time the plasma left the sun to the time and position the same plasma arrived at the spacecraft:

$$t_0 = t_1 - \frac{r_1}{V_w} \tag{4.2}$$

The Voyager 1 spacecraft moves at a speed of 3.50 au/year which is then 0.3 au/month. The normalised Voyager variance data will be binned with bins of 0.3 au width. The resulting graphs after this process of tracking the plasma to its release time and then normalising the Voyager data accordingly are in Figure 4.25.

Figure 4.25 indicates a dependency of the form $\sim r^{-2.7}$ since the slope of the straight line through the data values is -2.7. There is a noticeable upturn in the variance at large radial distances and it was thought that this may be due to the introduction of spacecraft noise into the spectra by means of the f^{-1} part of some spectra. However, this was ruled out as an absolute reason for the upturn. Further study on the variance values, at large radial distances, will prove necessary.

It is useful to compare the variances of the N component of the magnetic field calculated with the different datasets from the the two Voyager spacecraft. Figure 4.26 (a) shows the normalized results for Voyager 2 (Smith et al., 2006) and (b) for Voyager 1 from the current study. The variations in the Voyager 2 data is around two orders of magnitude, while it is around one order of magnitude in the Voyager 1 data. However, at 30 au the two datasets

both give values around 10^{-4} nT^2. Engelbrecht (2008) modeled the radial dependence of the x-component of the slab turbulence and found that the radial dependence agrees with the $r^{-2.7}$ dependence found by the present study for the magnetic field variance of the data. Balogh et al. (2001) suggest a value of -3.4 for the radial dependence of hourly data magnetic field variance components. Helios 1 and 2 data observations of high-speed streams (Schwenn and Marsch, 1991) suggest that the strongest radial dependence of the total variance of magnetic field components scales as $\sim r^{-4}$. The study of the variances at radial distances larger than those considered in the current project could be used to further constrain the power law index of the radial dependence of the variances.

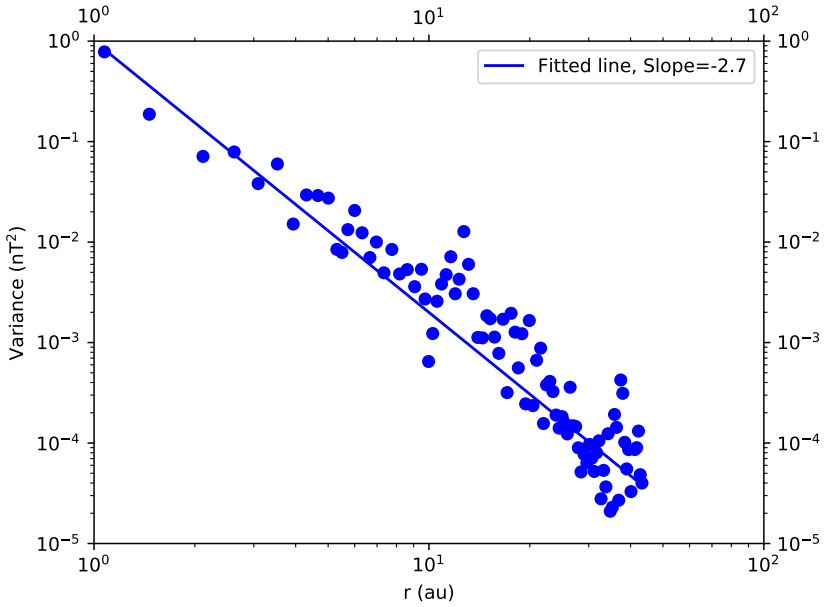

Figure 4.25: Magnetic field variance data for the N component as a function of radial distance in au. Also indicated on the figure is the slope of the line fitted through the data normalised to the values at Earth.

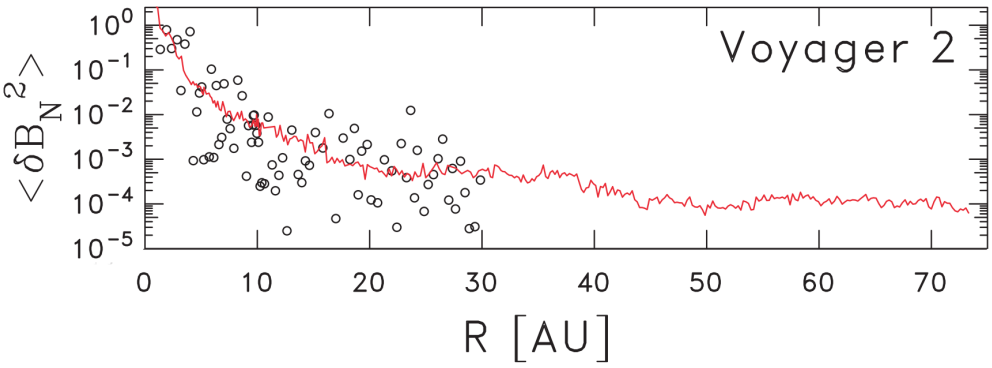

(a)

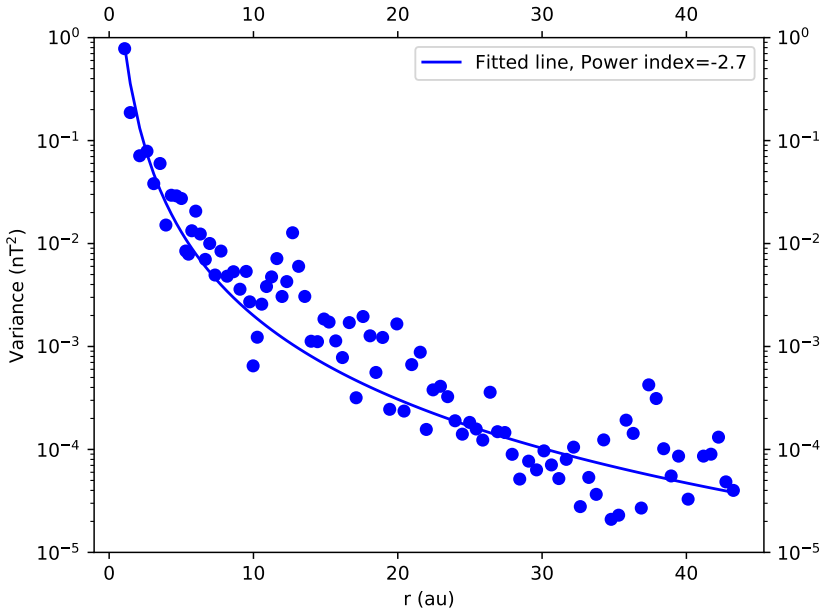

(b)

Figure 4.26: (a) Variance of magnetic field data recorded by Voyager 2 as a function of radial distance up to 70 au. The black circles indicate the variance values calculated from data and the red lines indicate model predicted values from Smith et al. (2006). (b) Variance of magnetic field data recorded by Voyager 1 as a function of radial distance up to 40 au. The data is the same as in Figure 4.25, but here plotted on a log-linear scale for easier comparison with the comparable Voyager 2 data in panel (a). The blue circles indicate the variance values calculated in the present analysis and the solid line indicates a power law curve fit to the data which is normalised to the values at Earth.

4.5 Summary

This chapter describes the filtering and analysis of the Voyager 1 magnetic field data. The aim of the filtering process is to remove spurious data peaks and to ensure an average data resolution of 48 s. The filtered data is then used to construct turbulence power spectra. The analysis of these turbulence power spectra reveals four different forms of the background spectrum. A Kolmogorov type spectral index is prominent at smaller radial distances whilst a f^{-1} type spectrum is more prominent at the larger radial distances considered. Also observed in the turbulence power spectra of this data set are spectral enhancements above the background spectrum. Enhancements above the background spectrum include sharp frequency spikes at 5×10^{-4} Hz and pickup ion peaks. The pickup ion peaks occur at the helium and proton gyrofrequencies. Proton pickup ion peaks are more prevalent than helium pickup ion peaks. The helium pickup ion peaks are observed more than the proton peaks at the smaller radial distances, whereas the proton pickup ion peaks are more prevalent at larger radial distances. The final topic discussed in this chapter is the radial dependence of the magnetic field variance. The dependence of the variance as a function of radial distance scales as $r^{-2.7}$. The radial dependence of the variances in the current analysis compares well with that in previous observations over the radial distances considered in this project.

Chapter 5

The structure of turbulence

5.1 Introduction

The focus of this dissertation is on the frequency spectrum as observed by a single spacecraft. The spectral form and the level of turbulence (or noise) were looked at. However, it is of great importance in scattering theory to also consider the structure of the turbulence. In a seminal paper, Matthaeus et al. (1990) suggested the presence of quasi-two dimensional fluctuations in the solar wind. In this case, the wave vectors are in a plane perpendicular to the background magnetic field, hence the designation of two dimensional. In the well-known slab or Alfvénic model, the structure is such that the wave vectors are parallel to the background magnetic field. As noted by Bieber et al. (1994), a two-dimensional component of the turbulence would not contribute to the resonant scattering of particles. However, it would add to the levels measured by a magnetometer. Bieber (1996) devised methods to distinguish between slab- and two-dimensional turbulence and showed that the two-dimensional component of turbulence, in fact, dominates the inner heliosphere. In this Chapter, their analysis is revisited and an incomplete result for integrals generalised.

5.2 Slab turbulence, 2D turbulence and composite model

Consider a mean magnetic field component $\mathbf{B}_0$ which has a constant value (Bieber, 1996). The first step in describing the structure of homogenous, isotropic turbulence is to note down the correlation matrix for the scenario at hand. The two-point correlation matrix is defined as $R_{ij}(\mathbf{r}) =< b_i(\mathbf{x})b_j(\mathbf{x}+\mathbf{r}) >$ where b_i denotes the components of the fluctuating part of the field ($\mathbf{b}$) (Bieber, 1996). Since the magnetic field is assumed to be spatially homogenous, the correlation matrix R_{ij} is assumed to depend only on the lag $\mathbf{r}$ and not on the spatial variable $\mathbf{x}$ (Bieber, 1996). The power spectrum is defined as

$$P_{ij}(\mathbf{k}) = \frac{1}{(2\pi)^3}\int d^3r R_{ij}(\mathbf{r})e^{-i\mathbf{k}\cdot\mathbf{r}}. \tag{5.1}$$

(Bieber, 1996; Matthaeus et al., 2007).

This is a Fourier transform of the correlation function (in real space $\Re^3$) to $\mathbf{k}$ wavenumber space. The spatial ($\mathbf{r}$) vectors and wave vectors ($\mathbf{k}$) in Equation 5.1 have magnitudes $\boldsymbol{r} = (r_x^2 + r_y^2 + r_z^2)^{1/2}$ and $\boldsymbol{k} = (k_x^2 + k_y^2 + k_z^2)^{1/2}$, respectively. These definitions may be

simplified further by assuming axisymmetry. More specifically, assume that the turbulence is symmetric about the mean magnetic field direction along the z-axis such that $\hat{\mathbf{z}} \equiv \frac{\mathbf{B}_0}{|\mathbf{B}_0|}$ (Bieber, 1996). The assumptions made above imply that the x and y axes or the k_x and k_y axes (in k-space) are interchangable. It is then for convenience and by convention to define a perpendicular wavenumber and a parallel wavenumber using field aligned co-ordinates (Bieber, 1996). The perpendicular and parallel wavenumbers are defined as

$$k_\perp \equiv |\hat{\mathbf{z}} \times \mathbf{k}| = (k_x^2 + k_y^2)^{1/2} \tag{5.2}$$

$$k_\parallel = k_z. \tag{5.3}$$

The turbulent field can now be described by slab and 2D components, which each assume different behaviours of $k_\perp$ and $k_\parallel$.

5.2.1 Slab turbulence

Following the assumptions made in Bieber (1996), consider a slab turbulence model and assume $k_\perp \approx 0$ so that the slab turbulence is a function of $k_\parallel$ only. Consider only the diagonal entries of the power spectrum matrix which are calculated from Equation 5.1. Note that the double index in P_{ii} will not imply summation in the present study.

$$P_{ii}^{(slab)}(\mathbf{k}) = \frac{1}{(2\pi)^3} \int_{-\infty}^{\infty} dx \int_{-\infty}^{\infty} dy \int_{-\infty}^{\infty} dz R_{ii}(\mathbf{r}) e^{(-ik_x x - ik_y y - ik_z z)}. \tag{5.4}$$

In the case of slab turbulence, the correlation matrix depends only on the spatial variable z (Bieber, 1996), so that Equation 5.4 becomes

$$P_{ii}^{(slab)}(\mathbf{k}) = \frac{1}{(2\pi)^3} \int_{-\infty}^{\infty} dx e^{-ik_x x} \int_{-\infty}^{\infty} dy e^{-ik_y y} \int_{-\infty}^{\infty} dz R_{ii}(\mathbf{z}) e^{-ik_z z}. \tag{5.5}$$

Notice that the integrals in the spatial variables x and y are the Fourier inverse transform integrals of the respective delta functions in k space so that Equation 5.5 becomes

$$P_{ii}^{(slab)}(\mathbf{k}) = \frac{1}{2\pi} \delta(k_x)\delta(k_y) \int_{-\infty}^{\infty} dz R_{ii}(z) e^{-ik_z z}. \tag{5.6}$$

Equation 5.6 leads to the diagonal entries of the matrix

$$P_{xx}^{slab}(\mathbf{k}) = P_{yy}^{slab}(\mathbf{k}) = G_S(k_z)\delta(k_x)\delta(k_y), \tag{5.7}$$

where $G_S = \frac{1}{2\pi} \int_{-\infty}^{\infty} dz R_{ii}(z) e^{-ik_z z}$. The equality of $P_{xx}^{slab}(\mathbf{k})$ and $P_{yy}^{slab}(\mathbf{k})$ follows as a consequence of axisymmetry. The entry for the power spectrum matrix z-component is $P_{zz}(\mathbf{k}) = 0$ under the solenoidal constraint (Bieber, 1996). A short discussion of the solenoidal constraint and the form of the spectrum tensor now follows.

Consider a vector field $\mathbf{F}$ which is **Divergence Free**; this is the essense of the constraint. The solenoidal constraint is stated as $\nabla \cdot \mathbf{F} = 0$ (Matthaeus and Goldstein, 1982) for the vector field $\mathbf{F}$. For turbulent magnetic fields $\mathbf{B}$, it follows that $\nabla \cdot \mathbf{B} = 0$ which implies that $\frac{dR_{ij}(\mathbf{r})}{dx_i} = 0$ where $R_{ij}(\mathbf{r})$ refers to the correlation function (Matthaeus and

Goldstein, 1982). This constraint implies further that $k_i P_{ij}(\mathbf{k}) = 0$ where k_i is a wavenumber and $P_{ij}(\mathbf{k})$ is the power spectrum tensor. If $i = j = z$, then according to the solenoidal constraint $k_z P_{zz}(\mathbf{k}) = 0$. The slab models used in this work assume k_z to be non-zero. This implies for slab models that given $k_z P_{zz}(\mathbf{k}) = 0$, $P_{zz}(\mathbf{k}) = 0$ is true.

Consider now a brief motivation for the form of the spectral tensor used in discussing $2D$ turbulence geometry. It is shown in Matthaeus et al. (2007) that the solenoidal constraint $k_i P_{ij}(\mathbf{k}) = 0$ can be used to derive $P_{ij}(\mathbf{k}) = \Big(\delta_{ij} - \frac{k_i k_j}{k^2}\Big) S(\mathbf{k})$ which is given in scalar form as $P_{ij}(k) = \Big(\delta_{ij} - \frac{k_i k_j}{k^2}\Big) S(k)$ with $S(k) = \frac{E(k)}{4\pi k^2}$ for $E(k)$ as the turbulence energy spectrum.

Considering the vector form $P_{ij}(\mathbf{k}) = \Big(\delta_{ij} - \frac{k_i k_j}{k^2}\Big) S(\mathbf{k})$ in the case of $2D$ geometry, this can be written in the form $P_{ij}^{(2D)}(\mathbf{k}) = \Big(\delta_{ij} - \frac{k_i k_j}{k^2}\Big) S(k_x, k_y)\delta(k_z)$ for $S(\mathbf{k}) = S(k_x, k_y)\delta(k_z)$. Consulting the work for example by Matthaeus and Smith (1981) and Shalchi (2008), further simplifies the above form of the spectral tensor to

$$P_{ij}^{(2D)}(\mathbf{k}) = \Big(\delta_{ij} - \frac{k_i k_j}{k^2}\Big) \frac{G^{2D}(k_\perp)}{k_\perp} \delta(k_z), \tag{5.8}$$

for $S(k_x, k_y) = \frac{G^{2D}(k_\perp)}{k_\perp}$, where $G^{2D}(k_\perp)$ is the wave spectrum (Shalchi, 2008).

5.2.2 2D turbulence

In the case of the 2D turbulent field geometry, the power spectrum matrix is constructed much like in the slab geometry case but starts with different assumptions. Assume as in Bieber (1996) that the model depends only on $k_\perp$ when $k_\parallel \approx 0$. The power spectrum matrix for 2D turbulence will now be calculated. Begin as in the slab case with Equation 5.1, which then in turn becomes

$$P_{ij}^{(2D)}(\mathbf{k}) = \frac{1}{(2\pi)^3} \int_{-\infty}^{\infty} dx \int_{-\infty}^{\infty} dy \int_{-\infty}^{\infty} dz R_{ij}(x, y) e^{(-ik_x x - ik_y y - ik_z z)}. \tag{5.9}$$

The correlation matrix is independent of z for 2D turbulence. Equation 5.9 then further simplifies to

$$P_{ij}^{(2D)}(\mathbf{k}) = \frac{1}{(2\pi)^2} \delta(k_z) \int_{-\infty}^{\infty} dx \int_{-\infty}^{\infty} dy R_{ij}(x, y) e^{-ik_x x} e^{-ik_y y}. \tag{5.10}$$

The next step is to examine Equation 5.10 for the diagonal entries of the matrices since this discussion will not concern off-diagonal terms. Recall from section 5.2 that $Pij^{(2D)}(\mathbf{k})$ can be calculated by making use of equation 5.8 . The component of the power spectrum matrix along the x-direction is

$$\begin{aligned} P_{xx}^{(2D)}(\mathbf{k}) &= \delta(k_z)\Big(\delta_{xx} - \frac{k_x^2}{k_\perp^2}\Big) \frac{G_{2D}(k_\perp)}{k_\perp} \\ &= \delta(k_z)\Big(1 - \frac{k_x^2}{k_x^2 + k_y^2}\Big) \frac{G_{2D}(k_\perp)}{k_\perp} \\ &= \delta(k_z) k_y^2 \frac{G_{2D}(k_\perp)}{k_\perp^3}. \end{aligned} \tag{5.11}$$

The component of the power spectrum matrix in the y-direction is calculated in the same manner:

$$\begin{aligned} P_{yy}^{(2D)}(\mathbf{k}) &= \delta(k_z)\Big(\delta_{yy} - \frac{k_y^2}{k_\perp^2}\Big)\frac{G_{2D}(k_\perp)}{k_\perp} \\ &= \delta(k_z)\Big(1 - \frac{k_y^2}{k_x^2 + k_y^2}\Big)\frac{G_{2D}(k_\perp)}{k_\perp} \\ &= \delta(k_z)k_x^2\frac{G_{2D}(k_\perp)}{k_\perp^3}. \end{aligned} \tag{5.12}$$

There is one final assumption required for this model as made in Bieber (1996) and that is to assume that $P_{zz}^{(2D)}(\mathbf{k}) = 0$.

5.2.3 Composite models

The aim in this section is to formulate a composite geometric model comprised of both slab and 2D turbulent components. This discussion does not concern all frequencies but only those in the ***inertial range***.

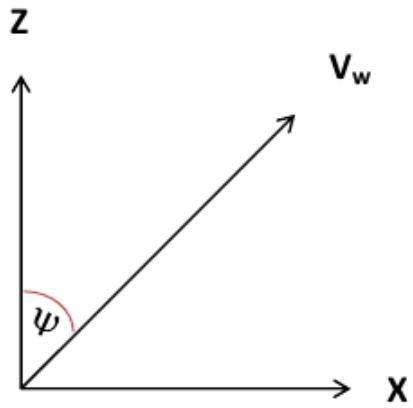

Figure 5.1: Align the z-axis with the mean magnetic field as before. The x-axis is in the plane defined by the radial solar wind velocity vector and the mean field vectors. All vectors point away from the Sun. The y-axis is the orthogonal axis to the x-z plane. ψ is the field or spiral angle.

The field angle in Figure 5.1 is defined as the acute angle between the mean magnetic field and the solar wind velocity vector direction. This angle is defined in such a way so that its sine or cosine will produce a positive value. The power spectrum, as a function of frequency, is to be calculated with respect to this coordinate system. The first step in this process involves defining the appropriate correlation matrix. Fourier transform theory is instrumental in retrieving a frequency spectrum from temporal input data. This property will be used to calculate the power spectrum, as a function of frequency, from a temporal correlation matrix. Denote the temporal correlation matrix by $R_{ij}^{(t)}(\delta t)$ and as

in previous discussions, a spatial correlation matrix is also necessary when discussing the structure of turbuluence. The spatial correlation matrix is denoted by $R_{ij}^{(\mathbf{x})}(\delta\mathbf{x})$. Before proceeding with the correlation function, a relation between the two correlation functions is required. One particular assumption to be made during this process is that when discussing the solar wind, the magnetic field is "frozen in". This assumption implies that the solar wind is fixed to the mean field in the z-direction (Roberts, 2007). It also implies that motions in the y-direction are not permitted since they are perpendicular to the fluid flow as concluded by making reference to Alfvén's theorem (Roberts, 2007). Consult Figure 5.1 when calculating the components of $R_{ij}^{(\mathbf{x})}(\delta\mathbf{x}) = R_{ij}^{(\mathbf{x})}(x, y, z)$. The diagonal entries of this matrix are $x = V_w\delta t \sin\psi$, $y = 0$, $z = V_w\delta t\cos\psi$. The two correlation functions are then finally related through $R_{ij}^{(t)}(\delta t) = R_{ij}^{(\mathbf{x})}(-V_w\delta t\sin\psi, \quad 0, \quad -V_w\delta t\cos\psi)$. Performing a Fourier inverse transform of the correlation matrix in the temporal domain of $R_{ij}^{(t)}(\delta t)$ produces the power spectrum as a function of frequency,

$$P_{ij}(f) = \int_{-\infty}^{\infty} d(\delta t)e^{i2\pi f\delta t}R_{ij}^{(t)}(\delta t). \tag{5.13}$$

This equation needs to be written in terms of wavenumber so that the results of the previous sections can be applied when constructing composite models. It follows then that

$$\begin{aligned} P_{ij}(f) &= \int_{-\infty}^{\infty} d(\delta t)e^{i2\pi f\delta t}R_{ij}^{(\mathbf{x})}(\delta\mathbf{x}) \\ &= \int_{-\infty}^{\infty} d(\delta t)e^{i2\pi f\delta t}\iiint_{-\infty}^{\infty} d^3kP_{ij}(\mathbf{k})e^{ik_xx}e^{ik_yy}e^{ik_zz} \\ &= \int_{-\infty}^{\infty} d(\delta t)e^{i2\pi f\delta t}\iiint_{-\infty}^{\infty} d^3kP_{ij}(\mathbf{k})e^{-ik_xV_w\delta t\sin\psi}e^{-ik_zV_w\delta t\cos\psi}. \end{aligned} \tag{5.14}$$

The integrals above are now solved separately for slab and 2D turbulence for both the parallel and perpendicular components. It is convention to denote P_{yy} by $P_\perp$. P_{yy} is thus the perpendicular spectrum. P_{xx} is denoted by $P_\parallel$ and is known as the "quasi-parallel spectrum" since only a component of the P_{xx} spectrum is parallel to the radial direction. These definitions are used in accordance with the field aligned coordinates assumed previously in this section. After introducing these components, slab and 2D turbulence can be decomposed into parallel and perpendicular contributions which are then used to formulate the composite models in field aligned coordinates. Substituting $P_{xx}^{slab}(\mathbf{k}) = P_{yy}^{slab}(\mathbf{k}) = G_S(k_z)\delta(k_x)\delta(k_y)$ into Equation 5.14 yields the parallel and perpendicular components of the slab geometry,

$$\begin{aligned} P_\parallel^{(slab)}(f) &= P_{xx}^{(slab)}(f) \\ &= \int_{-\infty}^{\infty} d(\delta t)e^{i2\pi f\delta t}\int_{-\infty}^{\infty}\int_{-\infty}^{\infty}\int_{-\infty}^{\infty} dk_xdk_ydk_z \\ &\quad \times G_S(k_z)\delta(k_x)\delta(k_y)e^{-ik_xV_w\delta t\sin\psi}e^{-ik_zV_w\delta t\cos\psi} \\ &= \int_{-\infty}^{\infty} d(\delta t)e^{i2\pi f\delta t}\int_{-\infty}^{\infty} dk_zG_S(k_z)e^{-ik_zV_w\delta t\cos\psi}; \end{aligned}$$

which from section 5.2.1 can be rewritten as

$$P_{\parallel}^{(slab)}(f) = \int_{-\infty}^{\infty} d(\delta t) e^{i2\pi f \delta t} R_{ij}(z).$$

The δt factor should be eliminated by substitution for $z = V_w \delta t \cos\psi$ such that the integral takes the form

$$P_{\parallel}^{(slab)}(f) = \int_{-\infty}^{\infty} \frac{dz}{V_w \cos\psi} e^{i2\pi f \frac{z}{V_w \sin\psi}} R_{ij}(z),$$

which further simplifies to

$$P_{\parallel}^{(slab)}(f) = \int_{-\infty}^{\infty} \frac{dz}{V_w \cos\psi} e^{ik_z z} R_{ij}(z), \tag{5.15}$$

where $k_z = \frac{2\pi f}{V_w \cos\psi}$. Equation 5.15 is just the Fourier inverse transform of $R_{ij}(z)$. The complete parallel slab component of the measured frequency spectrum follows as

$$P_{\parallel}^{(slab)}(f) = \frac{2\pi}{V_w \cos\psi} G_S(k_z). \tag{5.16}$$

Similarly, the perpendicular slab component P_{yy} is calculated from $P_{yy} = P_{xx}$ and thus is the same as the parallel component in Equation 5.16. Finally, for the slab geometry,

$$P_{\perp}^{(slab)}(f) = P_{\parallel}^{(slab)}(f) = \frac{2\pi}{V_w \cos\psi} G_S(k_z). \tag{5.17}$$

The same calculations are then performed for the 2D geometry. In this case, the parallel and perpendicular components are different and need to be calculated separately by making use of both Equations 5.11 and 5.12, respectively. One property of Fourier transforms is that $\int_{-\infty}^{\infty} d(\delta t) e^{i2\pi f \delta t} = \delta(f)$ since this is just the expression for the inverse Fourier transform of the delta function $\delta(f)$ as a function of frequency f. Using this the parallel power spectrum component is calculated as

$$\begin{aligned} P_{\parallel}^{(2D)}(f) &= \int_{-\infty}^{\infty} d(\delta t) e^{i2\pi f \delta t} \int_{-\infty}^{\infty} \int_{-\infty}^{\infty} \int_{-\infty}^{\infty} dk_x dk_y dk_z G_{2D}(k_\perp) \frac{k_y^2}{k_\perp^3} \delta(k_z) \\ &\qquad \times e^{-ik_x V_w \delta t \sin\psi} e^{-ik_z V_w \delta t \cos\psi} \\ &= \int_{-\infty}^{\infty} d(\delta t) e^{i2\pi f \delta t} \int_{-\infty}^{\infty} \int_{-\infty}^{\infty} dk_x dk_y G_{2D}(k_\perp) \frac{k_y^2}{k_\perp^3} e^{-ik_x V_w \delta t \sin\psi} \\ &= \delta(f) \int_{-\infty}^{\infty} dk_y k_y^2 \int_{-\infty}^{\infty} dk_x \frac{G_{2D}(k_\perp)}{k_\perp^3} e^{-ik_x V_w \delta t \sin\psi}. \end{aligned}$$

The integrand in the variable k_y is even and so the integral in k_y may be rewritten as $2\int_0^{\infty} dk_y k_y^2$. Take the derivative of the expression $k_\perp^2 = k_x^2 + k_y^2$ with respect to the variable k_y and find that $dk_\perp k_\perp = k_y dk_y$. Substituting these changes yields

$$P_{\parallel}^{(2D)}(f) = 2\delta(f)\int_0^\infty dk_\perp k_\perp k_y \int_{-\infty}^\infty dk_x \frac{G_{2D}(k_\perp)}{k_\perp^3} e^{-ik_x V_w \delta t \sin\psi}$$
$$= 2\delta(f)k_y \int_0^\infty dk_\perp \frac{G_{2D}(k_\perp)}{k_\perp^2} \int_{-\infty}^\infty dk_x e^{-ik_x V_w \delta t \sin\psi}.$$

These integrals need to be rewritten in terms of the frequency with

$$k_x = \frac{2\pi f}{V_w \sin\psi} \tag{5.18}$$

and after doing so the integrals are written as

$$P_{\parallel}^{(2D)}(f) = \frac{4\pi}{V_w \sin\psi} k_y \int_0^\infty dk_\perp \frac{G_{2D}(k_\perp)}{k_\perp^2} \int_{-\infty}^\infty df \delta(f) e^{-i2\pi f}.$$

Changing variables one last time from k_y to $k_\perp$ then yields the final expression with different limits on the integral. The lower limit of the integral in Equation 5.19 changes from 0 to $|k_x|$ since $k_\perp = |k_x|$ when $k_y = 0$. Equation 5.19 is the expression for the $2D$ parallel component of the power spectrum as a function of frequency f.

$$P_{\parallel}^{(2D)}(f) = \frac{4\pi}{V_w \sin\psi} \int_{|k_x|}^\infty dk_\perp \frac{G_{2D}(k_\perp)}{k_\perp^2} (k_\perp^2 - k_x^2)^{1/2}. \tag{5.19}$$

The calculation for the perpendicular $P_\perp^{(2D)}(f)$ component follows along a similar pattern. We have that

$$P_\perp^{(2D)}(f) = \int_{-\infty}^\infty d(\delta t) e^{i2\pi f \delta t} \int_{-\infty}^\infty \int_{-\infty}^\infty \int_{-\infty}^\infty dk_x dk_y dk_z G_{2D}(k_\perp) \frac{k_x^2}{k_\perp^3} \delta(k_z)$$
$$\times e^{-ik_x V_w \delta t \sin\psi} e^{-ik_z V_w \delta t \cos\psi}$$
$$= \int_{-\infty}^\infty d(\delta t) e^{i2\pi f \delta t} \int_{-\infty}^\infty \int_{-\infty}^\infty dk_x dk_y G_{2D}(k_\perp) \frac{k_x^2}{k_\perp^3} e^{-ik_x V_w \delta t \sin\psi}$$
$$= \delta(f) \int_{-\infty}^\infty dk_y (k_\perp^2 - k_y^2) \int_{-\infty}^\infty dk_x \frac{G_{2D}(k_\perp)}{k_\perp^3} e^{-ik_x V_w \delta t \sin\psi}.$$

Once again the integrand in the variable k_y is even and so the integral in k_y may be rewritten as $2\int_0^\infty dk_y (k_\perp^2 - k_y^2)$. Take the derivative of the expression $k_\perp^2 = k_x^2 + k_y^2$ with respect to the variable k_y and find that $dk_\perp k_\perp = k_y dk_y$. Substituting these changes yields

$$P_\perp^{(2D)}(f) = 2\delta(f) \int_0^\infty dk_\perp \frac{k_\perp}{k_y} (k_\perp^2 - k_y^2) \int_{-\infty}^\infty dk_x \frac{G_{2D}(k_\perp)}{k_\perp^3} e^{-ik_x V_w \delta t \sin\psi}.$$

These integrals need to be rewritten in terms of the variable f and after doing so the integrals are written as

$$P_{\perp}^{(2D)}(f) = \frac{4\pi}{V_w \sin\psi}\int_0^{\infty} dk_{\perp}\frac{k_{\perp}}{k_y}(k_{\perp}^2 - k_y^2)\frac{G_{2D}(k_{\perp})}{k_{\perp}^3}\int_{-\infty}^{\infty} df\delta(f)e^{-i2\pi f}$$
$$= \frac{4\pi}{V_w \sin\psi}\int_0^{\infty} dk_{\perp}\frac{k_x^2}{k_y}\frac{G_{2D}(k_{\perp})}{k_{\perp}^2}.$$

Changing variables one last time from k_y to $k_{\perp}$ then yields Equation 5.20 for the perpendicular component of the 2D geometry as a function of frequency f.

$$P_{\perp}^{(2D)}(f) = \frac{4\pi}{V_w \sin\psi}k_x^2\int_{|k_x|}^{\infty} dk_{\perp}\frac{G_{2D}(k_{\perp})}{k_{\perp}^2}(k_{\perp}^2 - k_x^2)^{-1/2}. \tag{5.20}$$

The lower limit of the integral in equation 5.20 comes about as explained in the derivation of equation 5.19.

However, the determination of the composite model begins by assuming an inertial range frequency spectra only. Assume that for slab geometry $G_S(k_z)$ is of the form $G_S(k_z) = C_S k_z^{-q}$ with the index $-q$ and where C_S is the amplitude of the slab component in the composite model as in Bieber (1996). Assume for $2D$ geometry that $G_{2D}(k_{\perp})$ is of the form $G_{2D}(k_{\perp}) = C_{2D}k_{\perp}^{-q}$ with the index $-q$ and where C_{2D} is the amplitude of the $2D$ component in the composite model as in Bieber (1996). Equation 5.17 is then rewritten as

$$P_{\perp}^{(slab)}(f) = P_{\parallel}^{(slab)}(f) = \frac{2\pi}{V_w \cos\psi}G_S(k_z)$$
$$= \frac{2\pi}{V_w \cos\psi}C_S k_z^{-q}.$$

Multiplying this result by frequency f and then substituting for k_z (Equation 5.2.3) yields the slab components (both parallel and perpendicular) of the composite model (Equation 5.21),

$$fP_{\perp}^{(slab)}(f) = fP_{\parallel}^{(slab)}(f) = C_S\Big(\frac{2\pi f}{V_w \cos\psi}\Big)^{1-q}. \tag{5.21}$$

The parallel 2D component represented by Equation 5.19 is reformulated as

$$P_{\parallel}^{(2D)}(f) = \frac{4\pi}{V_w \sin\psi}\int_{|k_x|}^{\infty} dk_{\perp}\frac{C_{2D}k_{\perp}^{-q}}{k_{\perp}^2}(k_{\perp}^2 - k_x^2)^{1/2}$$
$$= \frac{4\pi}{V_w \sin\psi}\int_{|k_x|}^{\infty} dk_{\perp}C_{2D}k_{\perp}^{-q-2}(k_{\perp}^2 - k_x^2)^{1/2}$$
$$= C_{2D}\Big(\frac{4\pi}{V_w \sin\psi}\Big)\frac{k_x^{-q}\quad\sqrt{\pi}\quad\Gamma(\frac{q}{2})}{4\Gamma(\frac{3+q}{2})}$$
$$= C_{2D}\Big(\frac{4\pi}{V_w \sin\psi}\Big)\frac{k_x^{-q}\quad\sqrt{\pi}\quad\Gamma(\frac{q}{2})}{2(1+q)\Gamma(\frac{1+q}{2})}.$$

Multiplying the last line in this calculation by f yields the (quasi-) parallel component of the 2D component as a function of frequency,

$$fP_{\parallel}^{(2D)}(f) = C_{2D}\Big(\frac{2\pi f}{V_w \sin\psi}\Big)^{(1-q)}\frac{\sqrt{\pi}\quad\Gamma(\frac{q}{2})}{(1+q)\Gamma(\frac{1+q}{2})}. \tag{5.22}$$

Reformulation of Equation 5.20 yields

$$\begin{aligned} P_{\perp}^{(2D)}(f) &= \frac{4\pi}{V_w \sin\psi} k_x^2 \int_{|k_x|}^{\infty} dk_{\perp} \frac{C_{2D} k_{\perp}^{-q}}{k_{\perp}^2} (k_{\perp}^2 - k_x^2)^{-1/2} \\ &= \frac{4\pi}{V_w \sin\psi} k_x^2 \int_{|k_x|}^{\infty} dk_{\perp} C_{2D} k_{\perp}^{-q-2} (k_{\perp}^2 - k_x^2)^{-1/2} \\ &= C_{2D}\Big(\frac{4\pi}{V_w \sin\psi}\Big) \frac{k_x^{-q} \quad \sqrt{\pi} \quad \Gamma(1+\frac{q}{2})}{2\Gamma(\frac{3+q}{2})} \\ &= C_{2D}\Big(\frac{4\pi}{V_w \sin\psi}\Big) \frac{q}{(1+q)} \frac{k_x^{-q} \quad \sqrt{\pi} \quad \Gamma(\frac{q}{2})}{2\Gamma(\frac{1+q}{2})}. \end{aligned}$$

Multiplying the last line in this calculation by f yields the perpendicular component of the 2D geometry as a function of frequency,

$$fP_{\perp}^{(2D)}(f) = C_{2D}\Big(\frac{2\pi f}{V_w \sin\psi}\Big)^{(1-q)} \frac{q}{(1+q)} \frac{\sqrt{\pi} \quad \Gamma(\frac{q}{2})}{\Gamma(\frac{1+q}{2})}. \tag{5.23}$$

The composite model is then constructed by adding the parallel components of the slab (5.21) and 2D (5.22) geometries and doing the same for the perpendicular components (5.21, 5.23).

$$fP_{\parallel}(f) = C_S\Big(\frac{2\pi f}{V_w \cos\psi}\Big)^{(1-q)} + C_{2D}\Big(\frac{2\pi f}{V_w \sin\psi}\Big)^{(1-q)} \frac{\sqrt{\pi} \quad \Gamma(\frac{q}{2})}{(1+q)\Gamma(\frac{1+q}{2})}, \tag{5.24}$$

$$fP_{\perp}(f) = C_S\Big(\frac{2\pi f}{V_w \cos\psi}\Big)^{(1-q)} + C_{2D}\Big(\frac{2\pi f}{V_w \sin\psi}\Big)^{(1-q)} \frac{q}{(1+q)} \frac{\sqrt{\pi} \quad \Gamma(\frac{q}{2})}{\Gamma(\frac{1+q}{2})}. \tag{5.25}$$

The aim is to determine the total energy $P_{SUM}(f)$ in the fluctuations as a function of a frequency f. Calculate the total energy $P_{SUM}(f) = P_{\parallel}(f) + P_{\perp}(f)$ by adding equations 5.24 and 5.25. In total, the energy spectrum as a function of frequency for the composite model (considering the inertial range frequencies only) is given by

$$fP_{SUM}(f) = 2C_S\Big(\frac{2\pi f}{V_w \cos\psi}\Big)^{(1-q)} + C_{2D}\Big(\frac{2\pi f}{V_w \sin\psi}\Big)^{(1-q)} \frac{\sqrt{\pi} \quad \Gamma(\frac{q}{2})}{\Gamma(\frac{1+q}{2})}. \tag{5.26}$$

5.3 Comparison with Bieber et al. (1996)

Bieber (1996) present Equation 5.27 for the total energy $P_{SUM}(f)$ in the turbulent magnetic field fluctuations as a function of frequency as

$$fP_{SUM}(f) = 2C_S\Big(\frac{2\pi f}{V_w \cos\psi}\Big)^{(1-q)} + 2C_{2D}\Big(\frac{2\pi f}{V_w \sin\psi}\Big)^{(1-q)}. \tag{5.27}$$

However, this differs from the current result in Equation 5.26,

$$fP_{SUM}(f) = 2C_S\Big(\frac{2\pi f}{V_w \cos\psi}\Big)^{(1-q)} + \frac{\sqrt{\pi} \quad \Gamma(\frac{q}{2})}{\Gamma(\frac{1+q}{2})} C_{2D}\Big(\frac{2\pi f}{V_w \sin\psi}\Big)^{(1-q)}.$$

The $2D$ contribution to the total power spectrum in Equation 5.27 has a multiplicative constant of 2 which is different from the factor $\frac{\sqrt{\pi}d\Gamma(\frac{q}{2})}{\Gamma(\frac{1+q}{2})}$ in Equation (5.26). This means then that Equation (5.27) is an approximation of the more general result in Equation (5.26) since for $q = 2$, Equations (5.27) and (5.26) produce the same result. Consider Figure 5.2 which shows a plot of these multiplicative constants.

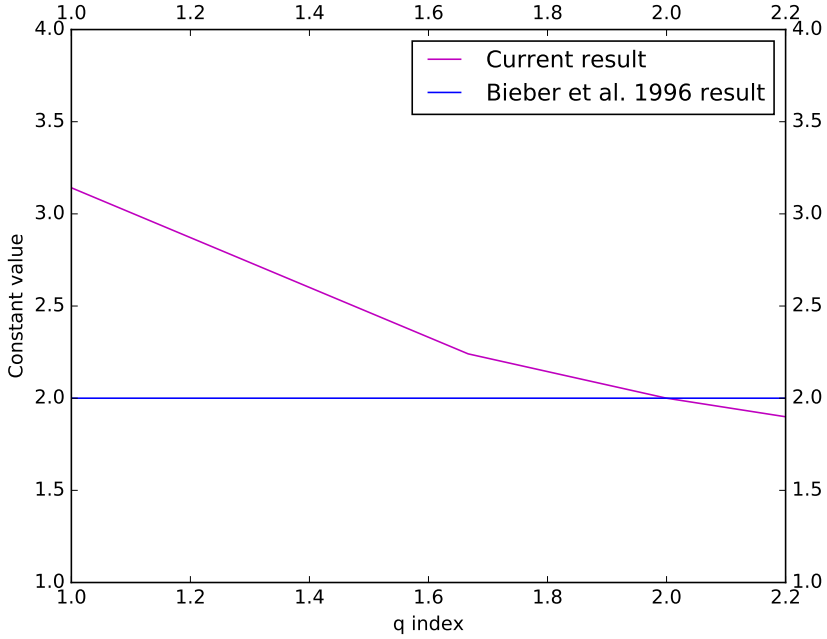

Figure 5.2: Plot of the multiplicative constant of the 2D contribution as a function of the index q. The value of the constant in Bieber (1996) is plotted in blue. The value of the constant, in the revised Equation 5.26 above, is plotted in magenta.

5.4 Summary

This chapter presented a theoretical review of the structure of turbulence. The concepts of slab and 2D turbulence are discussed. The slab and 2D turbulent components are defined in terms of parallel and perpendicular magnetic field fluctuations. A total power spectrum is then constructed from a composite model of these perpendicular and parallel components. The total power spectrum in the current project is compared to that in Bieber et al. (1993). The current calculations are valid for any value of the inertial range spectral index, while those of Bieber et al. (1993) are only valid for a value of 2.

Chapter 6

Discussion and conclusions

The current analysis utilizes a public-domain numerical technique specifically designed to analyse power spectra constructed from magnetic field data. The technique delivers satisfactory power spectral curves, even for data sets riddled with significant fractions of missing data. The aim of the filtering methods was to remove spurious data peaks and fill in the missing records to maintain a 48 s data resolution. Voyager 1 magnetic field data was then analysed over the period 1977 to 1990 during which time the spacecraft moved to about 44 au from the Sun.

The background spectra in the current analysis were found to exhibit four different distinct forms over the data period. The most common form of the background spectrum resembles the Kolmogorov inertial range. The high-frequency part of the spectrum includes a significant contribution of the f^{-1} form at radial distances larger than 30 au. However, this flattening behaviour is found to be inconsequential as far as the total energy density at the heliocentric radial distances considered in the current project. It is thus not necessary to account for this flattening of the spectrum at high frequencies in cosmic-ray modulation models, at least up to around 44 au. There is an indication that the level of the noise starts to level off. The same observation is made with the large spike in frequency near 5×10^{-4} Hz.

Pickup ion peaks were detected close to both the proton and helium gyrofrequencies. Proton pickup ions were more frequently seen in the spectra than the helium ions but the helium pickup ion peaks are seen closer to the Sun. This suggests, tentatively, that helium pickup ions penetrate deeper into the heliosphere than proton pickup ions. However, the composition of the pickup ion species detected in power spectra is a topic for future work. The presence of pickup ion peaks in the power spectra is found to neither alter the shape of the background spectrum nor affect the total energy density. The pickup ion peaks observed in the current work were compared with the observations by Hollick et al. (2018a). Six of the observations from the current analysis agreed with those in Hollick et al. (2018a) and eleven observations of pickup ion peaks are new observations not documented by these authors. As for the magnetic field variance as a function of radial distance, the current study found a radial dependence of $r^{-2.7}$. The result compares well to previous observations for the radial distances concerned in the current project.

The current project also revisited the theoretical calculations of Bieber (1996). Their expressions relating the observed frequency spectra for fluctuations perpendicular and (quasi-) parallel to background magnetic field, to wavenumber spectra for the slab- and for the

2D component of turbulence, were generalized to be valid for any (reasonable) value of the inertial range spectral index.

Acknowledgements

The author wishes to acknowledge and express gratitude for the following institutions and persons.

Institutions:

- The National Astrophysics and Space Science Programme (NASSP) for continued academic and financial support.
- The South African National Space Agency (SANSA) for continued financial support and opportunities.
- The North-West University (NWU) Potchefstroom Campus.
- The Centre for Space Research for the continued support of its staff and fellow students.

Persons:

- Prof. Ferreira, director of the Centre for Space Research.
- Prof. Burger, my supervisor.
- Mr. Fransman, the NWU Potchefstroom NASSP administrator.
- Dana Hyde, language and grammar editor.

A final special thanks goes to my God, Creator and Saviour.

Bibliography

Aggarwal, P., Taylor, D. K., Smith, C. W., Joyce, C. J., Fisher, M. K., Isenberg, P. A., Vasquez, B. J., Schwadron, N. A., Cannon, B. E., and Richardson, J. D. (2016). Voyager Observations of Magnetic Waves due to Newborn Interstellar Pickup Ions: 2-6 AU. *The Astrophysical Journal*, 822(2):94.

Axford, W. I., Dessler, A. J., and Gottlieb, B. (1963). Termination of solar wind and solar magnetic field. *The Astrophysical Journal*, 137:1268.

Balogh, A., Marsden, R. G., and Smith, E. J. (2001). *The heliosphere near solar minimum: The Ulysses perspective*. Springer Science & Business Media.

Bieber, J. W. (1996). Cosmic rays in the heliosphere. *Nuovo Cimento C Geophysics Space Physics C*, 19C:777–790.

Bieber, J. W., Chen, J., Matthaeus, W. H., Smith, C. W., and Pomerantz, M. A. (1993). Long-term variations of interplanetary magnetic field spectra with implications for cosmic ray modulation. *Journal of Geophysical Research: Space Physics*, 98(A3):3585–3603.

Bieber, J. W., Matthaeus, W. H., Smith, C. W., Wanner, W., Kallenrode, M.-B., and Wibberenz, G. (1994). Proton and Electron Mean Free Paths: The Palmer Consensus Revisited. *The Astrophysical Journal*, 420:294.

Borovsky, J. (2012). The velocity and magnetic field fluctuations of the solar wind at 1 au: Statistical analysis of fourier spectra and correlations with plasma properties. *Journal of Geophysical Research: Space Physics*, 117(A5).

Burlaga, L., Florinski, V., and Ness, N. (2015). In situ observations of magnetic turbulence in the local interstellar medium. *The Astrophysical Journal Letters*, 804(2):L31.

Burlaga, L., Florinski, V., and Ness, N. (2018). Turbulence in the outer heliosheath. *The Astrophysical Journal*, 854(1):20.

Cannon, B. E., Smith, C. W., Isenberg, P. A., Vasquez, B. J., Joyce, C. J., Murphy, N., and Nuno, R. G. (2014). Ulysses Observations of Magnetic Waves Due to Newborn Interstellar Pickup Ions. II. Application of Turbulence Concepts to Limiting Wave Energy and Observability. *The Astrophysical Journal*, 787(2):133.

Cannon, B. E., Smith, C. W., Isenberg, P. A., Vasquez, B. J., Joyce, C. J., Murphy, N., and Nuno, R. G. (2017). Listing of 502 Times When the Ulysses Magnetic Fields Instrument Observed Waves Due to Newborn Interstellar Pickup Protons. *The Astrophysical Journal*, 840(1):13.

Davis, A. (2010). Coordinate systems descriptions. `http://www.srl.caltech.edu/STEREO/docs/coordinate_systems.html`. Date Accessed : 12/07/2019.

Decker, R. B. (1993). The role of magnetic loops in particle acceleration at nearly perpendicular shocks. *The Journal of Geophysical Research*, 98(A1):33–46.

Decker, R. B. and Vlahos, L. (1986). Numerical studies of particle acceleration at turbulent, oblique shocks with an application to prompt ion acceleration during solar flares. *The Astrophysical Journal*, 306:710–729.

Dobrowolny, M., M., A., and Veltri, P. (1980). Properties of magnetohydrodynamic turbulence in the solar wind. In *Solar and Interplanetary Dynamics*, pages 143–146. Springer.

Dosch, A. and Zank, G. (2015). *Transport Processes in Space Physics and Astrophysics: Problems and Solutions*, volume 918. Springer.

Engelbrecht, N. E. (2008). *On the heliospheric diffusion tensor and its effect on 26-day recurrent cosmic-ray variations*. PhD thesis, North-West University.

Engelbrecht, N. E. (2017). On the Effects of Pickup Ion-driven Waves on the Diffusion Tensor of Low-energy Electrons in the Heliosphere. *The Astrophysical Journal Letters*, 849(1):L15.

Engelbrecht, N. E. and Burger, R. A. (2013a). An Ab Initio Model for Cosmic-ray Modulation. *The Astrophysical Journal*, 772(1):46.

Engelbrecht, N. E. and Burger, R. A. (2013b). An Ab Initio Model for the Modulation of Galactic Cosmic-ray Electrons. *The Astrophysical Journal*, 779(2):158.

Engelbrecht, N. E., Strauss, R. D., le Roux, J. A., and Burger, R. A. (2017). Toward a Greater Understanding of the Reduction of Drift Coefficients in the Presence of Turbulence. *The Astrophysical Journal*, 841(2):107.

Falgarone, E. and Passot, T. (2008). *Turbulence and magnetic fields in astrophysics*, volume 614. Springer.

Fraternale, F., Gallana, L., Iovieno, M., Opher, M., Richardson, J., and Tordella, D. (2016). Turbulence in the solar wind: spectra from voyager 2 data at 5 au. *Physica Scripta*, 91(2):023011.

Frisch, U. and Kolmogorov, A. (1995). *Turbulence: the legacy of AN Kolmogorov*. Cambridge university press.

Goldreich, P. and Sridhar, S. (1995). Toward a Theory of Interstellar Turbulence. II. Strong Alfvenic Turbulence. *The Astrophysical Journal*, 438:763.

Goldreich, P. and Sridhar, S. (1997). Magnetohydrodynamic turbulence revisited. *The Astrophysical Journal*, 485(2):680.

Hollick, S. J., Smith, C. W., Pine, Z. B., Argall, M. R., Joyce, C. J., Isenberg, P. A., Vasquez, B. J., Schwadron, N. A., Sokół, J. M., Bzowski, M., et al. (2018a). Magnetic waves excited by newborn interstellar pickup ions measured by the voyager spacecraft from 1 to 45 au. i. wave properties. *The Astrophysical Journal*, 863(1):75.

Hollick, S. J., Smith, C. W., Pine, Z. B., Argall, M. R., Joyce, C. J., Isenberg, P. A., Vasquez, B. J., Schwadron, N. A., Sokół, J. M., Bzowski, M., et al. (2018b). Magnetic waves excited by newborn interstellar pickup ions measured by the voyager spacecraft from 1 to 45 au. ii. instability and turbulence analyses. *The Astrophysical Journal*, 863(1):76.

Hollick, S. J., Smith, C. W., Pine, Z. B., Argall, M. R., Joyce, C. J., Isenberg, P. A., Vasquez, B. J., Schwadron, N. A., Sokół, J. M., Bzowski, M., et al. (2018c). Magnetic Waves Excited by Newborn Interstellar Pickup Ions Measured by the Voyager Spacecraft from 1 to 45 au. III. Observation Times. *The Astrophysical Journal*, 237:34.

Howard, T. (2011). *Coronal mass ejections: An introduction*, volume 376. Springer Science & Business Media.

Hussein, M., Tautz, R., and Shalchi, A. (2015). The influence of different turbulence models on the diffusion coefficients of energetic particles. *Journal of Geophysical Research: Space Physics*, 120(6):4095–4111.

Isenberg, P. A. (2005). Turbulence-driven Solar Wind Heating and Energization of Pickup Protons in the Outer Heliosphere. *The Astrophysical Journal*, 623(1):502–510.

Jet Propulsion Laboratory, C. I. o. T. (n.d.a). Voyager interstellar science. Web site. `https://voyager.jpl.nasa.gov/mission/science/`.

Jet Propulsion Laboratory, C. I. o. T. (n.d.b). Voyager mission status. Web site. `https://voyager.jpl.nasa.gov/mission/status/`.

Jet Propulsion Laboratory, C. I. o. T. (n.d.c). Voyager mission timeline. Web site. `https://voyager.jpl.nasa.gov/mission/timeline/#event-a-once-in-a-lifetime-alignment`.

Jones, E., Oliphant, T., and Peterson, P. (2001). SciPy: Open source scientific tools for Python. Online; accessed on 27 March 2019.

Kolmogorov, A. (1941a). The Local Structure of Turbulence in Incompressible Viscous Fluid for Very Large Reynolds' Numbers. *Akademiia Nauk SSSR Doklady*, 30:301–305.

Kolmogorov, A. (1941b). The Local Structure of Turbulence in Incompressible Viscous Fluid for Very Large Reynolds' Numbers. *Akademiia Nauk SSSR Doklady*, 30:301–305.

Kota, J. and Jokipii, J. R. (1983). Effects of drift on the transport of cosmic rays. VI - A three-dimensional model including diffusion. *The Astrophysical Journal*, 265:573–581.

Kowal, G. and Lazarian, A. (2010). Velocity field of compressible magnetohydrodynamic turbulence: wavelet decomposition and mode scalings. *The Astrophysical Journal*, 720(1):742.

Kraichnan, R. H. (1965). Inertial-range spectrum of hydromagnetic turbulence. *The Physics of Fluids*, 8(7):1385–1387.

Lazarian, A. and Vishniac, E. (1999). Reconnection in a weakly stochastic field. *The Astrophysical Journal*, 517(2):700.

Losa, D., Lovera, M., Drai, R., Dargent, T., and Amalric, J. (2005). Electric station keeping of geostationary satellites: a differential inclusion approach. In *Proceedings of the 44th IEEE Conference on Decision and Control*, pages 7484–7489. IEEE.

Maclean, C., Pagnozzi, D., and Biggs, J. (2014). Planning natural repointing manoeuvres for nano-spacecraft. *IEEE Transactions on aerospace and electronic systems*, 50(3):2129–2145.

Marmarelis, V. (2004). *Nonlinear dynamic modeling of physiological systems*, volume 10. John Wiley & Sons.

Marsch, E. (1991). Mhd turbulence in the solar wind. In *Physics of the inner heliosphere II*, pages 159–241. Springer.

Matthaeus, W., Bieber, J., Ruffolo, D., Chuychai, P., and Minnie, J. (2007). Spectral properties and length scales of two-dimensional magnetic field models. *The Astrophysical Journal*, 667(2):956.

Matthaeus, W., Qin, G., Bieber, J., and Zank, G. (2003). Nonlinear collisionless perpendicular diffusion of charged particles. *The Astrophysical Journal Letters*, 590(1):L53.

Matthaeus, W. and Smith, C. (1981). Structure of correlation tensors in homogeneous anisotropic turbulence. *Physical Review A*, 24(4):2135.

Matthaeus, W. H. and Goldstein, M. L. (1982). Measurement of the rugged invariants of magnetohydrodynamic turbulence in the solar wind. *Journal of Geophysical Research: Space Physics*, 87(A8):6011–6028.

Matthaeus, W. H., Goldstein, M. L., and Roberts, D. A. (1990). Evidence for the presence of quasi-two-dimensional nearly incompressible fluctuations in the solar wind. *The Journal of Geophysical Research*, 95:20673–20683.

Möbius, E., Hovestadt, D., Klecker, B., Scholer, M., Gloeckler, G., and Ipavich, F. (1985). Direct observation of he+ pick-up ions of interstellar origin in the solar wind. *Nature*, 318(6045):426.

Moloto, K., Engelbrecht, N., and Burger, R. (2018). A simplified ab initio cosmic-ray modulation model with simulated time dependence and predictive capability. *The Astrophysical Journal*, 859(2):107.

Moloto, K. D. (2015). The effect of the heliospheric current sheet on cosmic-ray modulation. MSc dissertation, North-West University (South Africa), Potchefstroom Campus.

Nel, A. E. (2015). The solar-cycle dependence of the heliospheric diffusion tensor. MSc dissertation, North West University.

Ng, C. and Bhattacharjee, A. (2007). Anisotropic mhd turbulence. In *AIP Conference Proceedings*, volume 932, pages 137–143. AIP.

Owens, M. and Forsyth, R. (2013). The heliospheric magnetic field. *Living Reviews in Solar Physics*, 10(1):5.

Parker, E. (1965). Dynamical theory of the solar wind. *Space Science Reviews*, 4(5-6):666–708.

Roberts, P. H. (2007). Alfvén's theorem and the frozen flux approximation. In *Encyclopedia of Geomagnetism and Paleomagnetism*, pages 7–11. Springer.

Russell, C., Luhmann, J., and Strangeway, R. (2016). *Space Physics: An Introduction*. Cambridge University Press.

Saur, J. and Bieber, J. W. (1999). Geometry of low-frequency solar wind magnetic turbulence: Evidence for radially aligned Alfénic fluctuations. *The Journal of Geophysical Research*, 104(A5):9975–9988.

Schwenn, R. and Marsch, E. (1991). *Physics of the Inner Heliosphere II: Particles, Waves and Turbulence*, volume 21. Springer Science & Business Media.

Shalchi, A. (2008). Analytical forms of correlation functions and length scales of astrophysical turbulence. *Astrophysics and Space Science*, 315(1-4):31–43.

Smith, C. W., Isenberg, P. A., Matthaeus, W. H., and Richardson, J. D. (2006). Turbulent heating of the solar wind by newborn interstellar pickup protons. *The Astrophysical Journal*, 638(1):508–517.

Williams, L. and Zank, G. (1994). Effect of magnetic field geometry on the wave signature of the pickup of interstellar neutrals. *Journal of Geophysical Research: Space Physics*, 99(A10):19229–19244.

Williams, L. L. and Zank, G. P. (1994). Effect of magnetic field geometry on the wave signature of the pickup of interstellar neutrals. *Journal Geophysical Research*, 99(A10):19229–19244.

Wu, Y., Florinski, V., and Guo, X. (2016). Interstellar pickup ion production in the global heliosphere and heliosheath. *The Astrophysical Journal*, 832(1):61.

Zank, G. (2014). *Transport processes in space physics and astrophysics*. Springer.

Zank, G. P. (1999). Interaction of the solar wind with the local interstellar medium: a theoretical perspective. *Space Science Reviews*, 89:413–688.

Appendix A

A.1 Synthetic Data Generation

In order to benchmark the current Fourier technique, a data set with known turbulence characteristics (like spectral indices and spectral level, etc.) is needed. Such a technique is described in Decker and Vlahos (1986) and Decker (1993). The technique was used and discussed by Nel (2015). The current version (Burger 2019, Private Communication) makes small changes to the one described by Nel (2015).

The synthetic data mimic a magnetic field with a fluctuating random component and a zero mean denoted by $\langle \delta \mathbf{B}(z) \rangle = 0$. Consider a data set consisting of N points. The length of the data interval is L. Assume that the spacing between the points is denoted by h_b and that the data points are evenly spaced along the z-direction.

The number of points is specified by $N = 2^p$ with p only having non-negative values. The magnetic field at a point n is denoted by δB_n. The position of each data point is described by the relation $z_n \equiv n \cdot h_b$, in the z-direction. The value of n is limited by $0 \leqslant n \leqslant N-1$. In order to generate a synthetic power spectrum using the new synthetic data, the Fourier transform over the interval should be taken. The data interval $[0, L]$ is finite and so a discrete Fourier transform must be used. Start by considering the Fourier coefficients which can be used to express the data series as a Fourier series. Denote the Fourier coefficients by f_m and calculate them from

$$f_m = \sum_{n=0}^{N-1} \delta B_n e^{-ik_m z_n}, m = 0, 1, 2, ..., N-1. \tag{6.1}$$

The term k_m in Equation 6.1 is defined by $k_m = \frac{2\pi}{\lambda_m} = \frac{2\pi m}{N h_b}$ where λ_m is the wavelength corresponding with the m^{th} Fourier component f_m. The Fourier transform in Equation 6.1 has an inverse transform which is defined as

$$\delta B_n = \frac{1}{N} \sum_{m=0}^{N-1} f_m e^{ik_m z_n}, m = 0, 1, 2, ..., N-1. \tag{6.2}$$

Note that B_0 represents the mean field. Since this was assumed to be zero previously, it implies that $f_0 = 0$. Also, assume that δB_n is real-valued. This implies that the δB_n is equal to its complex conjugate.

The power spectrum is obtained by taking the square of the discrete inverse Fourier

transform of δB_n. The power spectrum can thus be written as follows:

$$P_n = \left| \frac{1}{N} \sum_{n=0}^{N-1} \delta B_n e^{ik_n z_m} \right|^2.$$

Consider only positive wavenumbers and recall that L can be recast as Nh_b when N is large. The expression above can then be recast as

$$\begin{aligned} P_m &\approx 2\frac{h_b}{L} \sum_{n=0}^{N-1} \delta B_n \frac{h_b}{L} \sum_{n=0}^{N-1} \delta B_n \\ &\approx 2\Big(\frac{h_b}{L}\Big)^2 |f_m|^2. \end{aligned}$$

The power per interval Δk is given by

$$\begin{aligned} P_m &\approx 2\Big(\frac{h_b}{L}\Big)^2 |f_m|^2 \\ &\approx \frac{2}{\Delta k}\Big(\frac{h_b}{L}\Big)^2 |f_m|^2 \\ &\approx \frac{h_b^2 \quad |f_m|^2}{L\pi}. \end{aligned} \tag{6.3}$$

Note that in Equation 6.3 $\Delta k = \frac{2\pi}{L}$. The smallest wavenumber corresponds to the mode $m = 1$. This means that $k_1 = \frac{2\pi}{Nh_b}$. In the case that N is very large, $N \approx N - 1$ is a good approximation. The approximation $\Delta k \approx k_1$ can be used as a consequence and thus Δk is substituted with $\frac{2\pi}{L}$ above.

Each wave mode m should have a different phase in order to ensure the random and fluctuating nature of the magnetic field. In order to introduce different phases for each mode m, a random phase angle should be introduced into the Fourier series expansions. This is achieved by introducing the random phase angle into the Fourier components f_m. The components are recast as $f_m = |f_m|e^{i\phi_m}$ where ϕ_m is the phase angle of mode m. The Fourier components can be expressed in terms of the power per unit wavenumber P_m calculated above. Recast 6.3 to solve for f_m and then substitute this into the Equation for f_m above. This yields

$$f_m = |f_m|e^{i\phi_m} = \Big(\frac{L\pi P_m}{h_b^2}\Big)^{\frac{1}{2}} e^{i\phi_m} = N\Big(\frac{\pi P_m}{L}\Big)^{\frac{1}{2}} e^{i\phi_m}. \tag{6.4}$$

From the assumption that $\delta B_n \equiv \delta B_n^*$, it follows that $\delta B_n = \frac{1}{N}\sum_{m=0}^{N-1} f_m^* e^{-ik_m z_n}$ where $f_m^* = N\Big(\frac{\pi P_m}{L}\Big)^{\frac{1}{2}} e^{-i\phi_m}$. Additionally, $\delta B_n = \sum_{m=0}^{N-1} \Big(\frac{\pi P_m}{L}\Big)^{\frac{1}{2}} e^{-i\phi_m} e^{-ik_m z_n}$. This expression simplifies to $\delta B_n = \sum_{m=0}^{N-1} A_m e^{-ik_m z_n}$ where $A_m = \Big(\frac{\pi P_m}{L}\Big)^{\frac{1}{2}} e^{-i\phi_m}$. δB_n is the Fourier transform of A_m and since δB_n is real valued, A_m is hermitian. This means that A_m obeys conjugate symmetry, implying that the real part of A_m is even about the midpoint of the interval. It implies, additionally, that the imaginary part of A_m is odd about the

midpoint of the interval. Only half of the A_m values are then independent. The modes to be considered thus change from $m = 0, 1, 2, ..., N-1$ to $m = 1, 2, 3, ..., \frac{N}{2} - 1$ and as a consequence the final expression for δB_n becomes

$$\delta B_n = 2 \sum_{m=0}^{\frac{N}{2}-1} A_m e^{-ik_m z_n}. \tag{6.5}$$

This is the Fourier transform expression for δB_n. However, in practise, such a computation is computationally expensive and as a result a Fast Fourier transform algorithm is used to perform the calculations. A_m is written in terms of P_m and so a normalised power spectrum P_m needs to be specified. Assume a power spectrum of the form

$$P_m = C\sigma^2 G\Big(k_m \frac{z_{c,j}}{2\pi}\Big); \tag{6.6}$$

where $z_{c,j}$ represents characteristic spatial scales, k_m is the wavenumber of the m^{th} wave mode as mentioned previously, and σ^2 is the variance of the data. The term $G(k_m \frac{z_{c,j}}{2\pi})$ in Equation 6.6 is an arbitrary function. The constant C in Equation 6.6 is the normalisation constant obtained by integrating Equation 6.7 below:

$$\int_{k_1}^{k_{N-1}} P_m dk \equiv \sigma^2. \tag{6.7}$$

The integration needs to be over a discrete interval because the data is discrete. Equation 6.7 is recast as

$$\begin{aligned} \sum_{m}^{N-1} P_m \Delta k &= \sigma^2 \\ \Rightarrow \frac{2\pi}{L} \sum_{m}^{N-1} P_m &= \sigma^2, \end{aligned} \tag{6.8}$$

where $\Delta k = \frac{2\pi}{L}$. Equations 6.6 and 6.8 are then used to solve for the normalisation constant C. Substituting Equation 6.6 into Equation 6.8 yields

$$\begin{aligned} &\frac{2\pi}{L} \sum_{m}^{N-1} C\sigma^2 G(k_m \frac{z_{c,j}}{2\pi}) = \sigma^2 \\ &\Rightarrow C = \frac{L}{2\pi C_{sum}}, \end{aligned}$$

where $C_{sum} = \sum_{m}^{N-1} G(k_m \frac{z_{c,j}}{2\pi})$. The power spectrum in Equation 6.6 is then rewritten in terms of the normalisation constant C as

$$P_m = \frac{L}{2\pi C_{sum}} \sigma^2 G(k_m \frac{z_{c,j}}{2\pi}). \tag{6.9}$$

The value of A_m in Equation 6.5 was related to the form of the power spectrum through $A_m = \Big(\frac{\pi P_m}{L}\Big)^{\frac{1}{2}} e^{-i\phi_m}$. The substituting for P_m from Equation 6.9 yields Equation

$$A_m = \sigma \left(\frac{G(k_m \frac{z_{c,j}}{2\pi})}{2C_{sum}} \right)^{\frac{1}{2}} e^{-i\phi_m}. \tag{6.10}$$

Single spacecraft measurements by their nature are time series. To convert spatial scales to time scales requires some assumptions. The magnetic field is assumed to be frozen into the solar wind flow. Therefore, $V = \frac{h_b}{t_b}$ where h_b represents a spatial structure in the solar wind which is convected past a stationary observer. t_b denotes the time resolution of the data. Combining $kV = 2\pi f$ with the definition of the flow speed in terms of h_b and t_b yields Equation

$$f = \frac{kh_b}{2\pi t_b}. \tag{6.11}$$

The correlation length z_c can also be written in terms of the flow speed by virtue of the correlation time t_c as in $z_c = Vt_c$. The argument of the function G should be rewritten in terms of frequency instead of wavenumber. The argument which is given by $k_m \frac{z_{c,j}}{2\pi}$ becomes

$$\begin{aligned} k_m \frac{z_{c,j}}{2\pi} &= 2\pi f_m \frac{t_b}{h_b} \frac{z_{c,j}}{2\pi} \\ &= 2\pi f_m \frac{t_b}{h_b} \frac{Vt_{c,j}}{2\pi} \\ &= 2\pi f_m \frac{t_b}{h_b} \frac{h_b}{t_b} \frac{t_{c,j}}{2\pi} \\ &= f_m t_{c,j}; \end{aligned} \tag{6.12}$$

where Equation 6.11 along with $z_{c,j} = Vt_{c,j}$ and $V = \frac{h_b}{t_b}$ have been used. In order to have the power spectrum in terms of frequency units (Hz) and not wavenumber units, the power spectrum expression in Equation 6.9 needs to be multiplied by $\frac{2\pi t_b}{h_b}$. The final expression for the power spectrum, as a function of frequency generated by the time series data, is given by

$$P(f_m) = \frac{Lt_b}{h_b C_{sum}} \sigma^2 G(f_m t_{c,j}). \tag{6.13}$$

Appendix B

- A " - " in the last two columns of each table indicates that there is no recorded observation from the work of Hollick et al. (2018c).
- A " - " in the last two columns of the "Current analysis" section of each table indicates no high-frequency break in the spectra.
- The latitude column in each table indicates the Heliographic latitude of the spacecraft in RTN coordinates.
- A " - " in the Spectral Type column indicates that the form of the spectrum does not fall into any of the classifications given in section 4.3.1.

Data					Current analysis						Hollick at. al	
#	Decimal year	Radial distance (au)	Latitude (degrees)	Data gaps (%)	Spectral Type	Spike at 5×10^{-4} Hz (Y/N)	He^+ (Y/N)	H^+ (Y/N)	High-frequency break f^{-1} (Hz)	High-frequency f^{-1} level (nT^2/Hz)	He^+ (Y/N)	H^+ (Y/N)
1	1977.679	1.01	7.30	18	1	N	N	N	-	-	N	Y
2	1977.714	1.03	7.38	54	1	N	N	N	-	-	N	N
3	1977.750	1.09	6.89	56	1	N	N	N	-	-	-	
4	1977.786	1.17	6.03	70	1	N	N	N	-	-	-	
5	1977.821	1.28	5.01	54	1	N	N	N	-	-	-	
6	1977.857	1.40	4.06	20	1	N	N	N	-	-	-	
7	1977.893	1.51	3.20	29	1	N	N	N	-	-	-	
8	1977.928	1.65	2.33	37	1	N	N	N	-	-	-	
9	1977.964	1.78	1.60	30	1	N	N	N	-	-	-	

Table B1: 1977

Data					Current analysis						Hollick at. al	
#	Decimal year	Radial distance (au)	Latitude (degrees)	Data gaps (%)	Spectral Type	Spike at 5×10^{-4} Hz (Y/N)	He^+ (Y/N)	H^+ (Y/N)	High-frequency break f^{-1} (Hz)	High-frequency f^{-1} level (nT^2/Hz)	He^+ (Y/N)	H^+ (Y/N)
1	1978.000	1.92	0.95	32	2	N	N	N	-	-	-	
2	1978.036	2.05	0.39	45	2	N	N	N	-	-	Y	Y
3	1978.071	2.18	-0.11	31	2	N	N	N	-	-	N	Y
4	1978.107	2.31	-0.55	36	2	N	N	N	-	-	-	
5	1978.143	2.44	-0.94	28	1	N	N	N	-	-	-	
6	1978.178	2.56	-1.29	35	2	N	N	N	-	-	-	
7	1978.214	2.69	-1.60	36	1	N	N	N	-	-	Y	Y
8	1978.249	2.80	-1.89	31	2	N	N	N	-	-	Y	N
9	1978.285	2.93	-2.17	45	1	N	N	N	-	-	-	
10	1978.321	3.04	-2.39	32	2	N	N	N	-	-	-	
11	1978.356	3.15	-2.61	52	2	N	N	N	-	-	-	
12	1978.392	3.26	-2.81	52	2	N	N	N	-	-	-	
13	1978.427	3.37	-2.99	61	2	N	N	N	-	-	-	
14	1978.463	3.48	-3.17	49	2	N	N	N	-	-	-	
15	1978.499	3.58	-3.33	79	3	N	N	N	2E-03	1.44E+00	-	
16	1978.534	3.69	-3.48	71	2	N	N	N	-	-	-	
17	1978.570	3.79	-3.62	62	1	N	N	N	-	-	-	
18	1978.605	3.89	-3.75	59	2	N	Y	N	-	-	-	
19	1978.641	3.98	-3.87	58	2	N	N	N	-	-	-	
20	1978.677	4.08	-3.99	53	2	N	N	N	-	-	-	
21	1978.712	4.17	-4.10	65	2	N	N	N	-	-	-	
22	1978.748	4.27	-4.20	58	2	N	N	N	-	-	-	
23	1978.784	4.36	-4.30	69	2	Y	N	N	-	-	-	
24	1978.819	4.46	-4.40	66	2	N	N	N	-	-	-	
25	1978.855	4.54	-4.48	64	2	N	N	N	-	-	-	

26	1978.890	4.62	-4.57	50	2	N	N	N	-	-	-
27	1978.926	4.71	-4.65	72	2	N	N	N	-	-	-
28	1978.962	4.82	-4.74	90	2	N	N	N	-	-	-

Table B2: 1978

Data					Current analysis						Hollick at. al	
#	Decimal year	Radial distance (au)	Latitude (degrees)	Data gaps (%)	Spectral Type	Spike at 5×10^{-4} Hz (Y/N)	He^+ (Y/N)	H^+ (Y/N)	High-frequency break f^{-1} (Hz)	High-frequency f^{-1} level (nT^2/Hz)	He^+ (Y/N)	H^+ (Y/N)
1	1979.001	4.89	-4.81	18	2	N	N	N	-	-	-	
2	1979.037	4.97	-4.88	12	2	N	N	N	-	-	Y	Y
3	1979.073	5.05	-4.95	10	2	N	N	N	-	-	-	
4	1979.108	5.13	-5.01	13	3	N	N	N	1E-03	1E-01	Y	Y
5	1979.144	5.21	-5.07	47	3	N	N	N	5E-03	9E-02	-	
6	1979.179	5.30	-5.13	11	3	N	N	N	2E-03	1.01E+00	-	
7	1979.215	5.34	-5.20	15	2	N	N	N	-	-	-	
8	1979.251	5.38	-5.25	12	2	N	N	N	-	-	Y	Y
9	1979.286	5.43	-5.31	34	2	N	N	N	-	-	Y	Y
10	1979.322	5.47	-5.35	65	2	N	N	N	-	-	Y	Y
11	1979.358	5.52	-5.39	31	2	N	N	N	-	-	-	
12	1979.393	5.58	-5.43	43	2	N	N	N	-	-	N	Y
13	1979.429	5.63	-5.46	36	2	N	N	N	-	-	N	Y
14	1979.464	5.69	-5.48	34	2	N	N	N	-	-	-	
15	1979.500	5.76	-5.50	21	2	N	N	N	-	-	N	Y
16	1979.536	5.82	-5.51	27	2	N	N	N	-	-	Y	Y
17	1979.571	5.89	-5.52	33	3	N	N	N	2E-03	5E-02	Y	Y
18	1979.607	6.04	-5.53	89	3	N	N	N	3E-03	1.20E-01	-	
19	1979.642	6.12	-5.53	74	2	N	N	N	-	-	Y	Y
20	1979.678	6.11	-5.53	57	2	N	N	N	-	-	N	Y
21	1979.714	6.19	-5.53	40	2	N	N	N	-	-	Y	Y
22	1979.749	6.27	-5.52	43	2	N	N	N	-	-	Y	Y
23	1979.785	6.36	-5.51	41	2	Y	Y	N	-	-	Y	Y
24	1979.820	6.44	-5.50	36	2	N	Y	Y	-	-	N	Y
25	1979.856	6.53	-5.48	34	3	N	N	N	4E-03	9E-02	Y	Y

26	1979.892	6.62	-5.46	31	3	N	N	N	5E-03	5E-02	Y	Y
27	1979.927	6.71	-5.44	49	2	N	N	N	-	-	Y	Y
28	1979.963	6.80	-5.42	16	2	N	N	N	-	-	Y	Y
29	1979.998	6.89	-5.40	39	-	N	N	N	-	-	-	

Table B3: 1979

Data					Current analysis						Hollick at.al	
#	Decimal year	Radial distance (au)	Latitude (degrees)	Data gaps (%)	Spectral Type	Spike at 5×10^{-4} Hz (Y/N)	He^+ (Y/N)	H^+ (Y/N)	High-frequency break f^{-1} (Hz)	High-frequency f^{-1} level (nT^2/Hz)	He^+ (Y/N)	H^+ (Y/N)
1	1980.000	6.90	-5.40	34	2	N	N	N	-	-	Y	Y
2	1980.036	6.99	-5.37	33	2	N	N	N	-	-	Y	N
3	1980.071	7.09	-5.35	25	2	N	N	N	-	-	Y	Y
4	1980.107	7.19	-5.32	37	2	Y	N	N	-	-	Y	Y
5	1980.142	7.29	-5.29	37	3	N	N	N	4E-03	1.20E-01	Y	Y
6	1980.178	7.39	-5.27	34	2	N	N	N	-	-	-	
7	1980.213	7.49	-5.24	57	2	N	N	Y	-	-	Y	Y
8	1980.249	7.59	-5.21	31	2	N	N	N	-	-	-	
9	1980.284	7.70	-5.18	9	2	N	N	N	-	-	-	
10	1980.320	7.80	-5.15	41	3	N	N	N	3E-03	8E-02	N	Y
11	1980.355	7.91	-5.12	64	3	N	N	N	4E-03	1E-02	-	
12	1980.391	8.02	-5.08	40	2	N	N	N	-	-	-	
13	1980.426	8.12	-5.05	23	3	Y	N	N	5E-03	1E-02	-	
14	1980.462	8.23	-5.02	35	3	N	N	N	5E-03	1.30E-01	-	
15	1980.497	8.34	-4.99	37	3	N	N	N	6E-03	1E-02	-	
16	1980.533	8.46	-4.96	53	3	N	N	N	3E-03	6E-02	-	
17	1980.568	8.56	-4.93	30	2	N	N	N	-	-	Y	N
18	1980.604	8.67	-4.90	20	2	N	N	N	-	-	-	
19	1980.639	8.78	-4.86	52	2	N	N	N	-	-	Y	Y
20	1980.675	8.97	-4.83	40	2	N	N	N	-	-	-	
21	1980.710	9.01	-4.80	6	2	N	N	N	-	-	N	Y
22	1980.746	9.12	-4.77	12	2	N	N	N	-	-	-	
23	1980.782	9.24	-4.74	55	2	N	N	N	-	-	-	
24	1980.817	9.35	-4.71	9	2	N	N	N	-	-	N	Y
25	1980.853	9.47	-4.68	69	2	N	N	N	-	-	-	

26	1980.888	9.55	-4.30	24	2	N	N	N	-	-	N	N
27	1980.924	9.61	-3.74	44	2	N	N	N	-	-	N	Y
28	1980.959	9.67	-3.19	77	2	N	N	N	-	-	-	
29	1980.995	9.74	-2.65	47	3	N	N	N	3E-03	1E-02	-	

Table B4: 1980

Data					Current analysis						Hollick at. al	
#	Decimal year	Radial distance (au)	Latitude (degrees)	Data gaps (%)	Spectral Type	Spike at 5×10^{-4} Hz (Y/N)	He^+ (Y/N)	H^+ (Y/N)	High-frequency break f^{-1} (Hz)	High-frequency f^{-1} level (nT^2/Hz)	He^+ (Y/N)	H^+ (Y/N)
1	1981.000	9.74	-2.56	53	2	N	N	N	-	-	-	
2	1981.036	9.81	-2.03	50	2	N	N	N	-	-	N	Y
3	1981.071	9.87	-1.50	46	2	N	N	N	-	-	N	Y
4	1981.107	9.94	-0.99	26	2	Y	N	N	-	-	N	Y
5	1981.142	10.0	-0.48	45	3	N	N	N	3E-03	1E-02	Y	Y
6	1981.178	10.1	0.03	43	2	N	N	N	-	-	-	
7	1981.214	10.2	0.53	36	2	N	N	N	-	-	Y	Y
8	1981.249	10.2	1.02	25	2	N	N	N	-	-	Y	Y
9	1981.285	10.3	1.50	23	3	N	N	N	4E-03	3E-02	-	
10	1981.321	10.4	1.98	39	3	N	N	N	4E-03	3E-02	-	
11	1981.356	10.5	2.45	41	3	Y	N	N	3E-03	9E-02	Y	N
12	1981.392	10.5	2.91	44	-	N	N	N	-	-	-	
13	1981.427	10.6	3.36	58	3	N	N	N	2E-03	2.40E-01	-	
14	1981.463	10.7	3.81	69	3	N	N	N	2E-03	2E-02	-	
15	1981.499	10.8	4.26	69	3	N	N	N	4E-03	4E-02	-	
16	1981.534	10.9	4.70	60	3	N	N	N	4E-03	6E-02	-	
17	1981.570	11.0	5.13	66	3	N	N	N	4E-03	3E-02	-	
18	1981.605	11.0	5.56	68	3	N	N	N	4E-03	7E-02	-	
19	1981.641	11.1	5.98	63	3	N	N	N	2E-03	5E-02	-	
20	1981.677	11.2	6.69	58	3	N	N	N	1E-03	2E-02	-	
21	1981.712	11.3	6.79	66	3	N	N	N	2E-03	9E-02	N	N
22	1981.748	11.4	7.18	72	3	N	N	N	2E-03	3E-02	-	
23	1981.783	11.5	7.57	56	3	N	N	N	2E-03	1E-01	-	
24	1981.819	11.6	7.96	54	3	N	N	N	3E-03	9E-02	N	N
25	1981.855	11.7	8.34	50	3	Y	N	N	3E-03	2E-02	-	

26	1981.890	11.8	8.72	55	3	N	N	N	2E-03	2E-02	N	Y
27	1981.926	11.9	9.09	65	3	Y	N	N	5E-03	7E-02	N	N
28	1981.961	12.0	9.45	55	3	N	N	N	5E-03	6E-02	-	
29	1981.997	12.1	9.81	54	-	N	N	N	-	-	-	

Table B5: 1981

Data					Current analysis						Hollick at. al	
#	Decimal year	Radial distance (au)	Latitude (degrees)	Data gaps (%)	Spectral Type	Spike at 5×10^{-4} Hz (Y/N)	He^+ (Y/N)	H^+ (Y/N)	High-frequency break f^{-1} (Hz)	High-frequency f^{-1} level (nT^2/Hz)	He^+ (Y/N)	H^+ (Y/N)
1	1982.000	12.1	9.84	62	2	N	N	N	-	-	-	
2	1982.036	12.3	10.6	68	2	N	N	N	-	-	N	Y
3	1982.071	12.3	10.6	56	3	N	N	N	1E-03	2E-02	-	
4	1982.107	12.4	10.9	61	2	N	N	N	-	-	-	
5	1982.143	12.5	11.2	55	3	N	N	N	3E-03	1E-02	-	
6	1982.178	12.6	11.6	65	2	N	N	N	-	-	-	
7	1982.214	12.7	12.0	70	2	Y	N	N	-	-	-	
8	1982.249	12.7	12.2	56	3	N	N	N	3E-03	3.30E-02	N	N
9	1982.285	12.9	12.5	59	3	N	N	N	2E-03	7E-02	-	
10	1982.321	13.0	12.9	56	3	N	N	N	1E-03	3E-02	-	
11	1982.356	13.1	13.2	63	2	N	Y	Y	-	-	-	
12	1982.392	13.2	13.5	49	2	N	N	N	-	-	N	Y
13	1982.427	13.3	13.8	60	2	N	N	N	-	-	N	Y
14	1982.463	13.7	14.1	54	2	N	N	N	-	-	-	
15	1982.499	13.5	14.4	49	2	N	N	N	-	-	-	
16	1982.534	13.6	14.6	46	2	N	N	N	-	-	N	N
17	1982.570	13.7	14.9	43	2	N	N	N	-	-	-	
18	1982.605	13.8	15.2	71	2	N	N	N	-	-	-	
19	1982.641	14.0	15.5	54	2	N	N	N	-	-	-	
20	1982.677	14.1	15.7	54	3	N	N	N	2E-03	2E-02	N	Y
21	1982.712	14.2	16.0	55	2	N	N	N	-	-	Y	N
22	1982.748	14.3	16.3	58	2	N	N	N	-	-	-	
23	1982.783	14.4	16.5	63	2	N	N	N	-	-	Y	N
24	1982.819	14.5	16.8	64	2	Y	N	N	-	-	-	
25	1982.855	14.6	17.0	59	2	N	N	N	-	-	Y	Y

26	1982.890	14.7	17.3	66	3	N	N	N	2E-03	1E-02	Y	Y
27	1982.926	14.8	17.5	64	2	N	N	N	-	-	-	
28	1982.962	14.9	17.8	46	2	N	N	N	-	-	-	
29	1982.997	15.1	18.0	45	2	N	N	N	-	-	-	

Table B6: 1982

Data					Current analysis						Hollick at. al	
#	Decimal year	Radial distance (au)	Latitude (degrees)	Data gaps (%)	Spectral Type	Spike at 5×10^{-4} Hz (Y/N)	He^+ (Y/N)	H^+ (Y/N)	High-frequency break f^{-1} (Hz)	High-frequency f^{-1} level (nT^2/Hz)	He^+ (Y/N)	H^+ (Y/N)
1	1983.000	15.1	18.0	49	2	N	N	Y	-	-	-	
2	1983.036	15.2	18.3	54	2	N	N	N	-	-	-	
3	1983.071	15.3	18.5	45	2	N	N	N	-	-	N	N
4	1983.107	15.4	18.7	50	-	N	N	N	-	-	Y	Y
5	1983.143	15.5	19.0	74	-	N	N	N	-	-	-	
6	1983.178	15.6	19.2	54	2	N	Y	Y	-	-	-	
7	1983.214	15.8	19.4	53	2	N	N	N	-	-	Y	Y
8	1983.249	15.9	19.6	51	2	N	N	N	-	-	Y	Y
9	1983.285	16.0	19.8	60	3	Y	N	N	4E-03	1E-02	Y	N
10	1983.321	16.1	20.1	53	2	N	N	N	-	-	-	
11	1983.356	16.2	20.3	49	2	N	N	N	-	-	Y	N
12	1983.392	16.3	20.5	47	2	N	Y	N	-	-	-	
13	1983.427	16.5	20.7	65	4	N	N	N	-	-	-	
14	1983.463	16.6	20.9	56	2	N	N	N	-	-	-	
15	1983.499	16.7	21.1	79	-	N	N	N	-	-	-	
16	1983.534	16.8	21.3	72	2	N	N	N	-	-	N	Y
17	1983.570	16.9	21.5	57	3	N	N	N	-	-	N	Y
18	1983.605	17.1	21.6	62	2	N	N	N	-	-	-	
19	1983.641	17.2	21.8	51	-	N	N	N	-	-	Y	Y
20	1983.677	17.3	22.0	46	2	N	N	N	-	-	-	
21	1983.712	17.4	22.2	53	3	N	N	N	3E-03	1E-02	N	Y
22	1983.748	17.5	22.4	76	2	N	N	N	-	-	-	
23	1983.783	17.7	22.6	70	2	N	Y	Y	-	-	Y	Y
24	1983.819	17.8	22.7	66	1	N	N	N	-	-	-	
25	1983.855	17.9	22.9	68	2	N	N	N	-	-	-	

26	1983.890	18.0	23.1	60	2	N	N	N	-	-	-
27	1983.926	18.1	23.2	55	3	N	N	N	1E-03	3E-02	Y	Y
28	1983.961	18.3	23.4	83	4	N	N	N	-	-	Y	Y
29	1983.997	18.4	23.6	60	-	N	N	N	-	-	-	

Table B7: 1983

Data					Current analysis						Hollick at. al	
#	Decimal year	Radial distance (au)	Latitude (degrees)	Data gaps (%)	Spectral Type	Spike at 5×10^{-4} Hz (Y/N)	He^+ (Y/N)	H^+ (Y/N)	High-frequency break f^{-1} (Hz)	High-frequency f^{-1} level (nT^2/Hz)	He^+ (Y/N)	H^+ (Y/N)
1	1984.002	18.4	23.6	66	3	Y	N	N	5E-03	3E-02	-	
2	1984.037	18.5	23.8	66	4	N	N	N	-	-	-	
3	1984.073	18.6	23.9	56	2	N	N	N	-	-	-	
4	1984.108	18.8	24.1	54	-	N	N	N	-	-	-	
5	1984.144	18.9	24.2	54	2	N	N	N	-	-	Y	Y
6	1984.180	19.0	24.4	62	2	N	N	N	-	-	Y	Y
7	1984.215	19.1	24.5	65	2	N	N	N	-	-	Y	N
8	1984.251	19.3	24.7	44	-	N	N	N	-	-	-	
9	1984.286	19.4	24.8	57	-	Y	N	N	-	-	N	Y
10	1984.322	19.5	25.0	79	4	N	N	N	-	-	-	
11	1984.357	19.6	25.1	61	4	N	N	N	-	-	-	
12	1984.393	19.8	25.3	58	2	N	N	N	-	-	-	
13	1984.429	19.9	25.4	49	2	N	N	N	-	-	-	
14	1984.464	20.0	25.6	75	2	N	N	N	-	-	-	
15	1984.500	20.1	25.7	61	3	N	N	N	1E-03	1E-02	N	Y
16	1984.535	20.3	25.8	70	2	N	N	N	-	-	-	
17	1984.571	20.4	26.0	76	-	N	N	N	-	-	-	
18	1984.606	20.5	26.1	74	3	N	N	N	1E-03	1E-02	-	
19	1984.642	20.6	26.2	77	-	N	N	N	-	-	-	
20	1984.677	20.8	26.4	78	2	N	N	N	-	-	-	
21	1984.713	20.9	26.5	81	2	N	N	N	-	-	-	
22	1984.749	21.0	26.6	86	2	N	N	N	-	-	-	
23	1984.820	21.3	26.9	83	-	N	N	N	-	-	-	
24	1984.855	21.4	27.0	72	3	N	N	N	1E-03	1E-02	-	
25	1984.891	21.5	27.1	68	2	N	N	N	-	-	-	

26	1984.926	21.6	27.2	78	-	N	N	N	-	-	-
27	1984.962	21.8	27.4	73	2	N	N	N	-	-	-
28	1984.998	21.9	27.5	50	2	N	N	N	-	-	-

Table B8: 1984

Data					Current analysis						Hollick at. al	
#	Decimal year	Radial distance (au)	Latitude (degrees)	Data gaps (%)	Spectral Type	Spike at 5×10^{-4} Hz (Y/N)	He^+ (Y/N)	H^+ (Y/N)	High-frequency break f^{-1} (Hz)	High-frequency f^{-1} level (nT^2/Hz)	He^+ (Y/N)	H^+ (Y/N)
1	1985.001	21.9	27.5	66	2	N	N	N	-	-	-	
2	1985.037	22.0	27.6	68	-	N	N	N	-	-	-	
3	1985.072	22.1	27.7	67	4	N	N	N	-	-	-	
4	1985.108	22.3	27.8	67	2	N	N	N	-	-	-	
5	1985.144	22.4	28.0	79	3	N	N	N	3E-03	1E-02	-	
6	1985.179	22.5	28.1	83	2	N	N	N	-	-	-	
7	1985.215	22.7	28.2	94	4	N	N	N	-	-	-	
8	1985.250	22.8	28.3	88	2	N	N	N	-	-	-	
9	1985.286	22.9	28.4	88	-	N	N	N	-	-	Y	Y
10	1985.322	23.0	28.5	87	-	N	N	N	-	-	-	
11	1985.357	23.2	28.6	89	2	N	N	N	-	-	-	
12	1985.393	23.3	28.7	80	2	N	N	N	-	-	-	
13	1985.428	23.4	28.8	87	2	N	N	N	-	-	-	
14	1985.464	23.6	29.0	88	4	N	N	N	-	-	-	
15	1985.500	23.7	29.0	95	2	N	N	N	-	-	-	
16	1985.535	23.8	29.1	94	4	N	N	N	-	-	-	
17	1985.571	23.9	29.2	81	2	N	N	N	-	-	-	
18	1985.606	24.0	29.3	68	3	N	N	N	1E-03	1E-02	-	
19	1985.642	24.2	29.4	66	2	N	N	N	-	-	-	
20	1985.678	24.3	29.5	63	4	N	N	N	-	-	-	
21	1985.713	24.4	29.6	63	-	N	N	N	-	-	-	
22	1985.749	24.5	29.7	66	3	Y	N	N	3E-03	1E-02	-	
23	1985.784	24.7	29.8	68	2	N	N	N	-	-	-	
24	1985.820	24.8	29.9	81	3	N	N	N	2E-03	4E-03	-	
25	1985.856	24.9	30.0	78	3	N	N	N	4E-03	1E-02	-	

26	1985.891	25.1	30.1	87	4	N	N	N	-	-	-
27	1985.927	25.2	30.2	76	3	N	N	N	3E-03	4E-03	Y	Y
28	1985.962	25.3	30.3	52	3	N	N	N	3E-03	1E-02	-
29	1985.998	25.4	30.3	86	-	N	N	N	-	-	-

Table B9: 1985

Data					Current analysis						Hollick at. al	
#	Decimal year	Radial distance (au)	Latitude (degrees)	Data gaps (%)	Spectral Type	Spike at 5×10^{-4} Hz (Y/N)	He^+ (Y/N)	H^+ (Y/N)	High-frequency break f^{-1} (Hz)	High-frequency f^{-1} level (nT^2/Hz)	He^+ (Y/N)	H^+ (Y/N)
1	1986.002	25.4	30.3	90	2	N	N	N	-	-	-	
2	1986.037	25.6	30.4	93	-	N	N	N	-	-	-	
3	1986.073	25.7	30.5	71	3	N	N	N	1E-03	4E-03	-	
4	1986.109	25.8	30.6	72	3	N	N	N	1E-03	1E-02	-	
5	1986.144	26.0	30.7	63	3	N	N	N	2E-03	5E-03	-	
6	1986.180	26.1	30.8	60	2	N	N	N	-	-	N	N
7	1986.215	26.2	30.8	67	3	N	N	N	2E-03	1E-02	-	
8	1986.251	26.3	30.9	62	3	Y	N	N	2E-03	1E-02	-	
9	1986.287	26.5	31.0	55	3	N	N	N	1E-03	5E-03	N	Y
10	1986.322	26.6	31.1	45	-	N	N	N	-	-	-	
11	1986.358	26.7	31.2	55	2	N	N	N	-	-	-	
12	1986.393	26.9	31.2	37	2	N	N	N	-	-	-	
13	1986.429	27.0	31.3	50	4	N	N	N	-	-	-	
14	1986.465	27.1	31.4	32	2	N	N	N	-	-	N	Y
15	1986.500	27.2	31.5	63	3	N	N	N	1E-03	4E-03	-	
16	1986.536	27.4	31.6	64	4	N	N	N	-	-	-	
17	1986.571	27.5	31.6	45	3	N	N	Y	1E-03	1E-02	N	Y
18	1986.607	27.6	31.7	47	3	N	N	N	7E-04	4E-03	-	
19	1986.643	27.8	31.8	51	3	Y	N	N	8E-04	4E-03	-	
20	1986.678	27.9	31.8	61	3	N	N	N	8E-04	3E-03	-	
21	1986.714	28.0	31.9	61	3	N	N	N	8E-04	3E-03	-	
22	1986.750	28.1	32.0	45	4	N	N	N	-	-	-	
23	1986.785	28.3	32.1	65	3	N	N	N	8E-04	3E-03	-	
24	1986.821	28.4	32.1	60	3	Y	N	N	1E-03	3E-03	-	
25	1986.856	28.5	32.0	62	3	N	N	N	1E-03	2E-03	-	

26	1986.892	28.6	32.3	62	4	N	N	N	-	-	-
27	1986.928	28.8	32.3	50	3	N	N	N	5E-04	2E-03	-

Table B10: 1986

Data					Current analysis						Hollick at. al	
#	Decimal year	Radial distance (au)	Latitude (degrees)	Data gaps (%)	Spectral Type	Spike at 5×10^{-4} Hz (Y/N)	He^+ (Y/N)	H^+ (Y/N)	High-frequency break f^{-1} (Hz)	High-frequency f^{-1} level (nT^2/Hz)	He^+ (Y/N)	H^+ (Y/N)
1	1987.002	29.0	32.5	63	2	N	N	N	-	-	-	
2	1987.037	29.2	32.5	52	3	N	N	N	5E-03	2E-03	-	
3	1987.073	29.3	32.6	59	3	N	N	N	2E-03	3E-03	-	
4	1987.109	29.4	32.7	50	3	N	N	N	2E-03	3E-03	-	
5	1987.144	29.6	32.7	59	3	N	N	N	1E-03	3E-03	-	
6	1987.180	29.7	32.8	50	3	N	N	N	3E-03	3E-03	-	
7	1987.215	29.8	32.9	44	3	N	N	N	6E-03	3E-03	-	
8	1987.251	29.9	32.9	43	3	N	N	N	1E-03	3E-03	N	Y
9	1987.287	30.1	33.0	55	3	N	N	N	1E-03	3E-03	-	
10	1987.322	30.2	33.1	45	3	N	N	N	2E-03	2E-03	-	
11	1987.358	30.3	33.1	39	3	N	N	N	1E-03	3E-03	-	
12	1987.393	30.5	33.2	44	3	Y	N	N	2E-03	3E-03	-	
13	1987.429	30.6	33.2	47	4	N	N	N	-	-	-	
14	1987.465	30.7	33.3	61	3	N	N	N	3E-03	2E-03	-	
15	1987.500	30.8	33.4	46	3	N	N	N	2E-03	2E-03	-	
16	1987.536	31.0	33.4	53	3	N	N	N	1.50E-03	2E-03	-	
17	1987.572	31.1	33.5	48	4	N	N	N	-	-	-	
18	1987.607	31.2	33.5	34	3	N	N	N	1.50E-03	3E-03	N	Y
19	1987.643	31.4	33.6	35	3	N	N	N	2E-03	3E-03	-	
20	1987.678	31.5	33.7	36	3	N	N	N	5E-03	3E-03	-	
21	1987.714	31.6	33.7	35	3	N	N	N	9E-04	3E-03	-	
22	1987.750	31.7	33.8	39	3	N	N	N	8E-04	3E-03	-	
23	1987.785	31.9	33.8	45	3	N	N	N	8E-04	3E-03	-	
24	1987.821	32.0	33.9	53	3	N	N	Y	1E-03	3E-03	-	
25	1987.856	32.1	33.9	52	3	N	N	N	1E-03	3E-03	N	Y

26	1987.892	32.3	34.0	61	3	N	N	N	1E-03	4E-03	-
27	1987.928	32.4	34.0	54	3	Y	N	N	3E-03	3E-03	N Y
28	1987.963	32.5	34.1	49	3	N	N	N	5E-04	4E-03	-
29	1987.999	32.6	34.1	25	-	N	N	N	-	-	-

Table B11: 1987

Data					Current analysis						Hollick at. al	
#	Decimal year	Radial distance (au)	Latitude (degrees)	Data gaps (%)	Spectral Type	Spike at 5×10^{-4} Hz (Y/N)	He^+ (Y/N)	H^+ (Y/N)	High-frequency break f^{-1} (Hz)	High-frequency f^{-1} level (nT^2/Hz)	He^+ (Y/N)	H^+ (Y/N)
1	1988.037	32.8	34.2	36	3	N	N	N	5E-04	3E-03	-	
2	1988.108	33.0	34.3	23	4	N	N	N	-	-	-	
3	1988.144	33.2	34.4	27	3	N	N	N	1E-03	3E-03	-	
4	1988.179	33.3	34.4	26	3	N	N	N	1E-03	3E-03	N	Y
5	1988.215	33.4	34.5	36	4	N	N	N	-	-	-	
6	1988.250	33.6	34.5	30	3	N	N	N	8E-04	3E-03	N	Y
7	1988.286	33.7	34.6	45	3	N	N	N	3E-04	2E-03	-	
8	1988.322	33.8	34.6	37	3	Y	N	N	4E-04	3E-03	-	
9	1988.357	34.0	34.7	34	3	N	N	N	8E-04	3E-03	-	
10	1988.393	34.1	34.7	35	3	N	N	N	1E-03	4E-03	-	
11	1988.428	34.2	34.8	41	3	N	N	N	1E-03	4E-03	-	
12	1988.464	34.3	34.8	54	4	N	N	N	-	-	N	Y
13	1988.499	34.5	34.8	25	3	N	N	N	9E-04	3E-03	-	
14	1988.535	34.6	34.9	33	4	N	N	N	-	-	-	
15	1988.570	34.7	34.9	32	4	N	N	Y	-	-	-	
16	1988.606	34.9	35.0	25	3	N	N	N	9E-04	3E-03	Y	Y
17	1988.641	35.0	35.0	28	3	Y	N	N	9E-04	3E-03	-	
18	1988.677	35.1	35.1	20	3	N	N	N	9E-04	3E-03	Y	Y
19	1988.713	35.2	35.1	32	3	N	N	N	2E-03	3E-03	-	
20	1988.748	35.4	35.2	34	4	N	N	N	-	-	-	
21	1988.784	35.5	35.2	43	4	N	N	N	-	-	-	
22	1988.819	35.6	35.3	55	3	N	N	N	8E-04	2E-03	-	
23	1988.855	35.6	35.3	50	4	N	N	N	-	-	-	
24	1988.890	35.9	35.3	44	3	N	N	N	3E-04	2E-03	-	
25	1988.926	36.0	35.4	50	3	N	N	N	2E-03	5E-03	N	Y

26	1988.961	36.2	35.4	61	3	N	N	N	6E-03	3E-03	-
27	1988.997	36.3	35.5	100	-	N	N	N	1E-03	3E-03	-

Table B12: 1988

Data					Current analysis						Hollick at. al	
#	Decimal year	Radial distance (au)	Latitude (degrees)	Data gaps (%)	Spectral Type	Spike at 5×10^{-4} Hz (Y/N)	He^+ (Y/N)	H^+ (Y/N)	High-frequency break f^{-1} (Hz)	High-frequency f^{-1} level (nT^2/Hz)	He^+ (Y/N)	H^+ (Y/N)
1	1989.002	36.3	35.5	43	3	N	N	N	2E-03	9E-03	Y	Y
2	1989.037	36.4	35.5	65	3	N	N	N	5E-03	3E-03	-	
3	1989.108	36.7	35.6	37	4	N	N	N	-	-	-	
4	1989.144	36.8	35.6	41	4	N	N	N	-	-	-	
5	1989.180	36.9	35.7	43	4	N	N	N	-	-	-	
6	1989.215	37.1	35.7	46	-	N	N	N	-	-	-	
7	1989.251	37.2	35.8	47	3	Y	N	Y	1E-03	3E-03	-	
8	1989.287	37.3	35.8	51	3	N	N	N	5E-04	4E-03	-	
9	1989.322	37.5	35.8	39	3	N	N	Y	2E-03	4E-03	-	
10	1989.358	37.6	35.9	45	3	N	N	N	3E-03	5E-03	-	
11	1989.393	37.7	35.9	54	3	N	N	N	4E-03	3E-03	-	
12	1989.429	37.8	36.0	43	3	N	N	N	4E-03	3E-03	-	
13	1989.465	38.0	36.0	31	3	N	N	N	3E-03	4E-03	-	
14	1989.500	38.1	36.0	44	3	N	N	N	1E-03	4E-03	Y	Y
15	1989.536	38.2	36.1	46	3	N	N	N	2E-03	5E-03	-	
16	1989.571	38.4	36.1	73	3	N	N	N	9E-04	4E-03	Y	Y
17	1989.607	38.5	36.2	84	3	N	N	N	3E-03	3E-03	-	
18	1989.643	38.6	36.2	72	3	N	N	N	2E-03	5E-03	-	
19	1989.678	38.8	36.2	34	3	N	N	N	2E-03	3E-03	-	
20	1989.714	38.9	36.3	42	3	N	N	N	9E-04	3E-03	-	
21	1989.749	39.0	36.3	57	3	N	N	N	5E-04	4E-03	-	
22	1989.785	39.1	36.3	64	3	Y	N	N	2E-03	3E-03	-	
23	1989.821	39.3	36.4	56	3	N	N	N	3E-03	4E-03	Y	Y
24	1989.856	39.4	36.4	73	3	N	N	N	4E-03	4E-03	-	
25	1989.892	39.5	36.4	55	3	N	N	N	2E-03	4E-03	-	

26	1989.927	39.7	36.5	72	4	N	N	N	-	-	-
27	1989.963	39.8	36.5	65	4	N	N	N	-	-	-
28	1989.999	39.9	36.6	38	-	N	N	N	-	-	-

Table B13: 1989

Data					Current analysis						Hollick at. al	
#	Decimal year	Radial distance (au)	Latitude (degrees)	Data gaps (%)	Spectral Type	Spike at 5×10^{-4} Hz (Y/N)	He^+ (Y/N)	H^+ (Y/N)	High-frequency break f^{-1} (Hz)	High-frequency f^{-1} level (nT^2/Hz)	He^+ (Y/N)	H^+ (Y/N)
1	1990.014	No data		100	-	N	N	N	-	-	-	
2	1990.085	No data		100	-	N	N	N	-	-	-	
3	1990.085	No data		100	-	N	N	N	-	-	-	
4	1990.121	No data		100	-	N	N	N	-	-	-	
5	1990.156	No data		100	-	N	N	N	-	-	-	
6	1990.192	No data		100	-	N	N	N	-	-	-	
7	1990.227	No data		92	-	N	N	N	-	-	-	
8	1990.263	40.9	36.8	51	3	N	N	N	6E-04	3E-03	N	Y
9	1990.299	41.0	36.8	56	3	N	N	N	9E-04	3E-03	-	
10	1990.334	41.1	36.8	45	3	Y	N	N	2E-03	4E-03	-	
11	1990.370	41.2	36.9	50	3	N	N	N	6E-03	4E-03	-	
12	1990.406	41.4	36.9	42	4	N	N	N	-	-	-	
13	1990.441	41.5	37.0	34	4	N	N	N	-	-	-	
14	1990.477	41.6	37.0	32	3	N	N	N	2E-03	3E-03	-	
15	1990.512	41.8	37.0	21	3	N	N	N	1E-03	4E-03	-	
16	1990.548	41.9	37.0	26	3	Y	N	N	7E-04	4E-03	-	
17	1990.584	42.0	37.1	89	3	N	N	N	2E-03	2E-03	-	
18	1990.619	42.2	37.1	35	4	N	N	N	-	-	-	
19	1990.655	42.3	37.2	52	3	N	N	N	-	-	-	
20	1990.690	42.4	37.2	52	3	Y	N	N	1E-03	2E-03	-	
21	1990.726	42.5	37.2	60	3	N	N	N	3E-03	2E-03	-	
22	1990.762	42.7	37.2	52	3	N	N	N	3E-03	2E-03	N	Y
23	1990.797	42.8	37.2	61	4	N	N	N	-	-	-	
24	1990.833	42.9	37.3	65	3	N	N	N	7E-03	2E-03	-	
25	1990.868	43.1	37.3	83	3	N	N	N	2E-03	2E-03	-	

26	1990.904	43.2	37.3	82	4	N	N	N	-	-	-
27	1990.940	43.3	37.4	69	3	N	N	N	2E-03	2E-03	-
28	1990.975	43.5	37.4	58	3	N	N	N	1E-03	2E-03	-

Table B14: 1990